Alma Mater Studiorum · Università di Bologna

SCUOLA DI INGEGNERIA E ARCHITETTURA
Dipartimento di Ingegneria Industriale
Corso di Laurea in Ingegneria Energetica

Tesi di Laurea in:
METODI NUMERICI PER L'ENERGETICA M

Benchmarking Activities on the ALFRED Core with the Deterministic Neutronic Code ERANOS

Relatore:
Prof. Ing. Matteo Gherardi

Candidato:
Saverio Quaranta

Correlatori:
Ing. Giacomo Grasso
Prof. Ing. Marco Sumini
Ing. Matteo Stanzani

Sessione II
Anno Accademico 2023/2024

"Saruman believes it is only great power that can hold evil in check, but that is not what I have found. It is the small everyday deeds of ordinary folk that keep the darkness at bay. Small acts of kindness and love. Why Bilbo Baggins? Perhaps because I am afraid, and he gives me courage."

[J.R.R.Tolkien – The Hobbit]

Sommario

La ricerca internazionale nell'ambito della produzione di energia mediante fissione nucleare si sta sempre più interessando ai reattori veloci refrigerati al piombo, a partire da quando il Generation IV International Forum (GIF) li propose come una soluzione promettente per la prossima generazione di sistemi energetici nucleari. Uno degli aspetti di interesse è legato alla capacità di questi reattori, grazie al loro spettro neutronico veloce, di consentire la chiusura del ciclo del combustibile, minimizzando la quantità di scorie nucleari generate e di risorse naturali richieste. L'Agenzia per l'Energia Nucleare (NEA) dell'OCSE, in collaborazione con l'Agenzia Nazionale Italiana per le Nuove Tecnologie, l'Energia e lo Sviluppo Economico Sostenibile (ENEA), sta supervisionando un benchmark internazionale sul progetto del reattore dimostrativo avanzato europeo refrigerato al piombo (ALFRED) come riferimento. L'obiettivo principale del benchmark è studiare la neutronica e la fisica dei reattori refrigerati al piombo, verificando la capacità degli strumenti computazionali attuali di simulare tali sistemi innovativi. In questo progetto di tesi, nato dalla collaborazione con ENEA, è stata utilizzata la suite deterministica di riferimento ERANOS e il suo codice integrato per celle e reticoli ECCO per affrontare le prime due fasi del benchmark neutronico di ALFRED. La prima fase si è concentrata sullo studio bidimensionale della fisica della cella elementare, che comprende la barra di combustibile e il refrigerante associato. La seconda fase, invece, ha riguardato lo studio di un intero assemblaggio, analizzato attraverso tre sotto-casi: un modello bidimensionale di un assemblaggio di combustibile, un modello bidimensionale di un assemblaggio di controllo circondato da assemblaggi di combustibile, e un modello bidimensionale di un assemblaggio di schermaggio circondato da assemblaggi di combustibile. Lo studio ha indagato sugli effetti delle sezioni d'urto di taluni isotopi rilevanti e sui valori dei principali parametri integrali di interesse quali: il fattore di moltiplicazione, il fattore di riproduzione e il fattore di utilizzo. Infine, sono state condotte analisi di sensibilità e incertezza per valutare la propagazione delle perturbazioni di input a quelle di output.

Abstract

International research in energy production by nuclear fission is increasingly focusing on lead-cooled fast reactors, since the Generation IV International Forum (GIF) first proposed them as a promising solution for the next generation of nuclear energy systems. One of the features of interest is the ability of these reactors, thanks to their fast neutron spectrum, to allow for the closure of the fuel cycle, minimizing the amount of nuclear waste generated and of natural resources requested. The OECD's Nuclear Energy Agency (NEA), in collaboration with the Italian National Agency for New Technologies, Energy, and Sustainable Economic Development (ENEA), is overseeing an international benchmark with the Advanced Lead-cooled Fast Reactor European Demonstrator (ALFRED) as reference. The main goal of the benchmark is to study the neutronics and physics of lead-cooled reactors, verifying the ability of current computational tools to simulate such innovative systems. In this thesis project, which emerged from the collaboration with ENEA, the reference deterministic ERANOS suite and its integrated cell and lattice code ECCO were used to tackle the first two phases of the ALFRED neutron benchmark. The first phase focused on the two dimensional study of the physics of the elementary cell, which comprises the fuel rod and the associated coolant. The second phase, on the other hand, involved the study of an entire sub-assembly, which was analyzed through three sub-cases: a two-dimensional model of a fuel assembly, a two-dimensional model of a control assembly surrounded by fuel assemblies, and a two-dimensional model of a shield assembly surrounded by fuel assemblies. The study investigated in depth the effects of various cross sections and the values of the main integral parameters of interest, such as the multiplication factor, the microscopic cross sections of the main isotopes, the reproduction factor, and the thermal utilization factor. Additionally, sensitivity and uncertainty analyses were conducted to evaluate the propagation of input perturbations to the output ones.

Contents

Chapter 1

Introduction

The increase in the global population and massive electrification means that the electricity demand is continuously rising. This requires the development and implementation of low-carbon-dioxide emission technologies to achieve the goal of net-zero emissions by 2050. Among the technologies known and already available today, energy produced through fission nuclear reactors, combined with renewables, is the most suitable to meet the aforementioned demands. However, such energy source does not enjoy total public support, which is certainly due to the fear of possible accidents, the most recent being the Fukushima accident in 2011. This fear is enhanced by concerns related to proliferation issues and long life nuclear waste management. It is precisely the analysis of these critical issues that has led to the creation of the GIF (Generation IV International Forum) [23], in which the objectives that the new generation of nuclear reactors (called Generation IV) must possess were discussed. From this, it emerged that future nuclear plants must guarantee high standards in terms of:

- Sustainability.
- Economic efficiency.
- Safety and reliability.
- Resistance to proliferation and physical protection.

Among the possible reactor models proposed by the GIF, the technology that is analyzed in this thesis is the one associated to LFR (Lead-cooled Fast Reactors). In these proposed nuclear reactors, the fissions due to neutrons in the fast component of the spectrum take the leading role. They can therefore be designed to achieve a closed fuel cycle, ensuring efficient conversion of fertile uranium to fissile plutonium and the management of actinides.
This type of reactor includes the reactor studied in the LEADER EU project (Lead-cooled European Advanced DEmonstration Reactor), focused on the review and improvement

of the design of ELFR (European Lead Fast Reactor), a reference commercial reactor with a capacity of 1500 MW_{th}, and the design of its demonstrator ALFRED (Advanced Lead-cooled Fast Reactor European Demonstrator), a 300 MW_{th} reactor [10].
After conclusion of the LEADER project, the ALFRED's design continued being developed by the Fostering ALFRED Construction (FALCON) International Consortium, which includes Ansaldo Nucleare (Italy), RATEN ICN (Romania), and ENEA (Italy). The main objective of the ALFRED project is to serve as a demonstrator for the European concept of LFR, demonstrating its safety and reliability. Also because of the collaborative framework within which the project is developed, it was chosen as reference system for an international benchmark on lead-cooled fast reactors, proposed by the OECD's Nuclear Energy Agency (NEA) jointly with the Italian National Agency for New Technologies, Energy and Sustainable Economic Development (ENEA) which, in its role of responsible for the core design within FALCON, can ensure access to all the necessary information for participants in the related ALFRED benchmark exercises.
One of the topics of the benchmark regards the physics of an LFR core, aimed at studying the neutronic behavior of an LFR, as well as at verifying the capability of current computational tools to simulate such innovative systems. The need for such benchmark arose from the lack of operational experience[1] to support their design, verification, and licensing.
The benchmark aims to assess the simulation capabilities for LFR systems through a gradual approach, starting from local models and progressing to full system simulations for both neutronics and thermal-hydraulics [20].
The three phases of the neutronic benchmark are:

- Phase 1: Fuel Pin Cell
  - Heterogeneous modeling of a fuel pin cell and criticality analysis in an infinite lattice.
- Phase 2: Sub-Assembly/Super-cell Simulations
  - Extension of the model to a full Sub-Assembly (S/A) or a super-cell comprising multiple S/As.
- Whole Core Simulations
  - Full-core modeling, including control, shutdown, and reflector/shield elements.

This thesis, developed in collaboration with ENEA, focuses on the analysis of the neutronic benchmark mentioned earlier. It specifically aims to present the simulation results

[1]The only exception derives from a dozen reactors built and operated in the ex-Soviet Union for submarine propulsion (the so called Alpha-class units). However, because of their classification as military secrets, no information is available in the public domain.

from the first two phases, obtained using the ECCO cell code [3] and the ERANOS reactor code [5]. The study offers an in-depth investigation of the effects of various cross sections and evaluates key integral parameters of interest, such as the multiplication factor, the microscopic cross sections of the main isotopes, the reproduction factor, and the thermal utilization factor. Moreover, sensitivity and uncertainty analyses were performed to assess how input perturbations propagate to the outputs.
In particular, the structure of the thesis is the following:
after this brief introduction, the second chapter gives an overview of LFR and in particular, the design of ALFRED, underlining the information useful for the reader to understand the benchmark. After that, the third chapter explains the numerical methods and the neutronic code used to solve the benchmark. The reader can find information about cell calculation for homogeneous and heterogeneous cells on the ECCO code and about sensitivity and uncertainty analysis on ERANOS. In the fourth chapter finally, the results of the first two phases of the benchmark are shown and discussed. At the end, the conclusions are presented.

Chapter 2

The Lead-Cooled Fast Reactor ALFRED

In this chapter, the concept of lead-cooled fast reactors (LFR) proposed by the GIF will be illustrated (see Figure 2.1), and the core design of the demonstrator reactor ALFRED - the main focus of the benchmark discussed in this thesis - will be explored in detail.

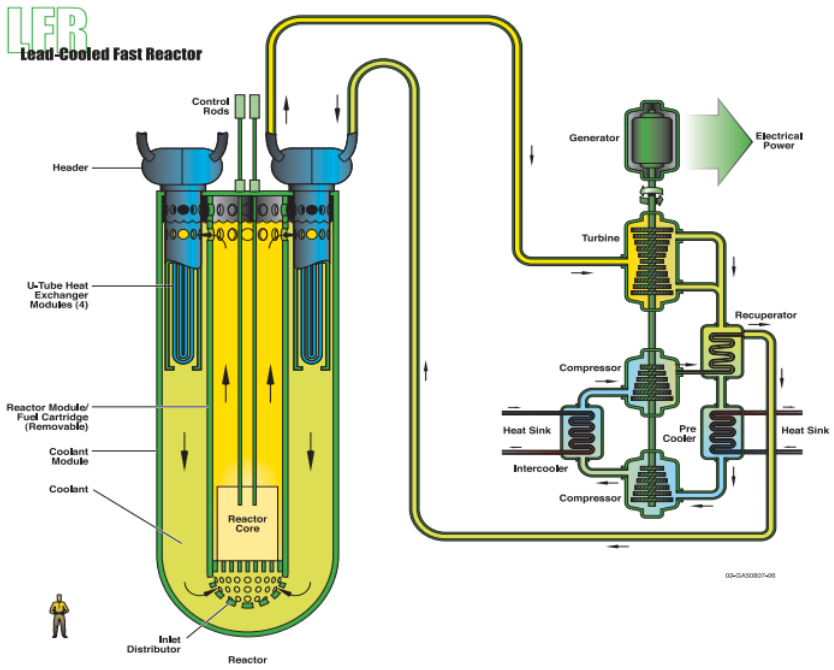

Figure 2.1: Scheme of LFR reactor [23].

2.1 Lead-Cooled Fast Reactors: Design Characteristics, Challenges, and Improvement

Lead-cooled fast reactors (LFRs) are fast-spectrum reactors that operate at high temperatures and pressures close to atmospheric conditions. Lead is chosen due to its high boiling point, approximately 1737°C [19]. In practice, the coolant may be pure lead or an alloy of lead and bismuth. Initially, the latter was preferred because its melting point of 125°C, lower than pure lead (327°C), was better suited for the original application of LFRs: submarine propulsion. However, the discussion here will focus only on reactors that use pure lead, as ALFRED is one of these.
In addition to its high boiling point, lead has the advantage of being chemically inert with water and air. This means that, unlike sodium-cooled fast reactors built between the 1970s and 1980s [9], LFRs do not present the risk of explosion in the event of contact between water/air and the coolant, so it avoids the need for an intermediate heat exchanger between the primary and secondary circuits [19].
These characteristics, along with its favourable thermodynamic properties, make lead intrinsically safe, allowing for a simplification of the reactor design. Indeed, with its excellent thermal inertia and high density, lead ensures efficient decay heat removal through natural circulation. This is facilitated by reduced pressure losses allowed by the increased spacing between fuel rods, permitted by the neutronic properties of lead without penalization to the fast neutron spectrum. The possibility of having such a spectrum is ensured by the absence of a true moderator, together with the nuclear properties of lead in terms of scattering and low absorption [19].
Currently, the coolant temperature at the core exit is designed to be between 480°C (for bare steels) and 530°C (for coated steels) due to material limitations in corrosion resistance, although it is anticipated that in the future it could be in the region between 750-880°C. The expected efficiency of the secondary cycle for the LFR system is at least 42% [18], higher than that of thermal reactors used to date.
The designs considered for this reactor were initially of two types: pool and loop; however, the former prevailed as it avoids seismic issues related to lead-filled piping (loop). The continuous study conducted over the past twenty years has led to various approaches in the design of the primary system for LFR reactors. Currently, Generation IV LFRs include three reference systems: the European Lead-cooled Fast Reactor (ELFR) (600 MWe), the Russian BREST-OD-300 system (300 MWe), and a small transportable system (SSTAR) (10-100 MWe) in the United States [18].
Both the ELFR and its demonstrator ALFRED, belonging to the European scenario, descend from a previous LFR project called European Lead-cooled System (ELSY). The latter played a fundamental role in the development of the lead-cooled reactor technology. With its pool-type approach, and the inclusion of steam generators with integrated pumps inside the vessel, ELSY achieved the goal of making this type of reactor more

compact (see Figure 2.2).

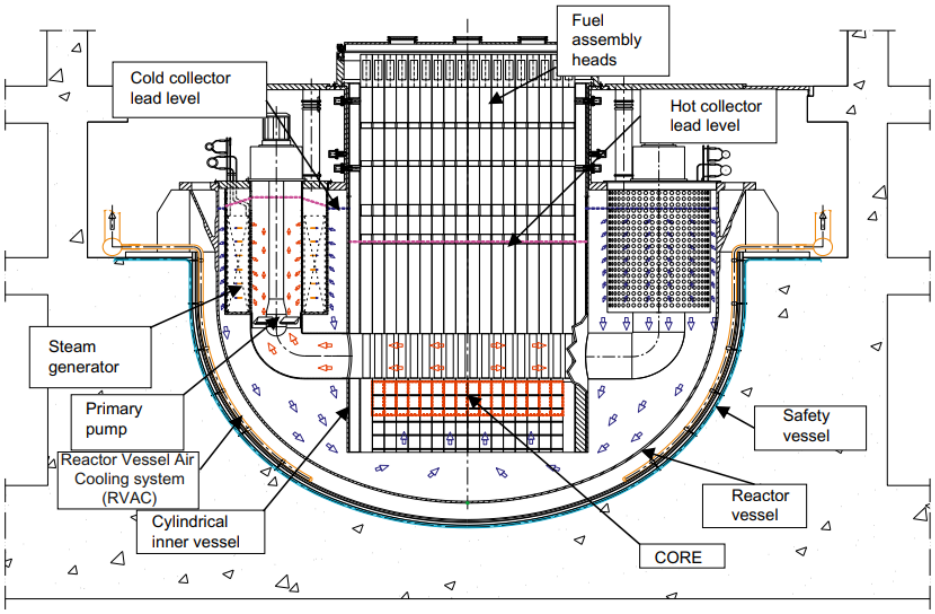

Figure 2.2: Scheme of ELSY's primary system [19].

It is worth outlining that, like all Generation IV technologies, LFRs also face challenges associated with their practical realization. In particular, for lead, it will be necessary to study materials capable of withstanding its high corrosive properties at elevated temperatures [19].

2.2 The ALFRED demonstrator

The following section will present the characteristics of ALFRED, highlighting the core-related aspects. The information provided will help the reader understand the case studies of the benchmark.

As previously explained, ALFRED is the demonstrator for the commercial LFR reactors developed in Europe. Furthermore, ALFRED can be considered a prorotype of an LFR Small Modular Reactor (LFR-SMR) [12], characterized by a power of $300 MW_{th}$ (corresponding to $125 MW_{el}$), and featuring a pool-type design that self-contains the whole primary system and other safety devices, as shown in Figure 2.3.

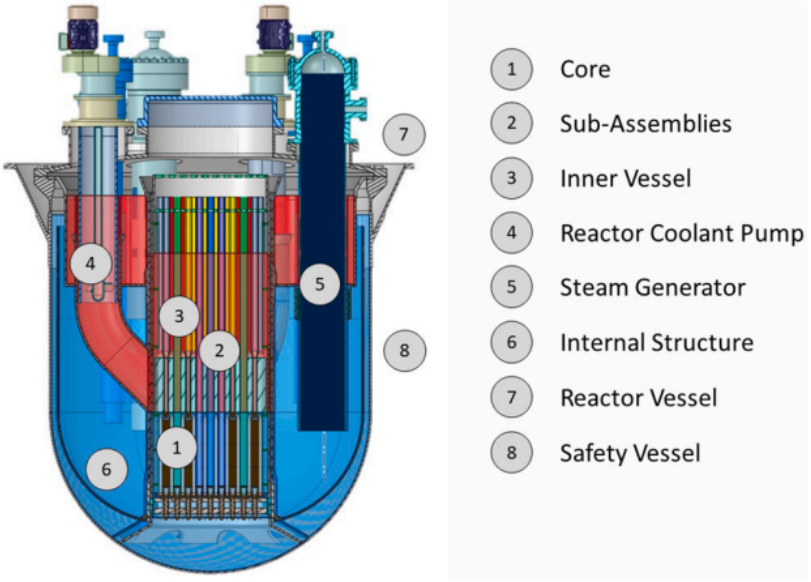

Figure 2.3: Scheme of ALFRED's primary system [14].

From the beginning, the design choices for ALFRED have prioritized safety, aiming for a reactor capable of operating at temperature limits imposed by materials, and ensuring the natural convection of lead in the event of a loss of flow. Regarding the temperature limits, it was decided to maintain the lead temperature above 380°C (lower limit), i.e., well above the freezing point of 327°C to prevent solidification, and below 600°C (upper limit) to prevent the corrosive effect of lead on the material coatings.
The problem of corrosion protection remains the main technological challenge for ALFRED and other LFRs. While protective strategies have been identified and characterized at laboratory scale, their demonstration under irradiation and ultimate qualification are still to be performed. Due to the shortage of irradiation reactors operating in fast spectrum, it was decided to adopt a new strategy for the qualification of coatings, that foresees the use of ALFRED itself as irradiation system for its own needs. Accordingly, a significant modification of the entire core design was performed in 2018. The following section will describe only the new reactor design; readers interested in the previous design are referred to [10].
To serve its irradiation needs, the new core has a special position at its center dedicated to material irradiation testing. Along with this, the reactor's operational phases have been divided into steps of increasing power and coolant temperatures, allowing for irradiation tests at progressively higher temperatures. This approach aims to achieve material self-qualification before moving to the subsequent phases, culminating with the final phase at nominal power [13]. All these considerations led to the core configuration shown in Figure 2.4, from which it is possible to observe that the updated core design

includes 151 main assemblies, consisting of 134 Fuel Assemblies (FAs), 12 Control Rods (CRs), 4 Safety Devices (SDs), and 1 Test Assembly for material qualification.

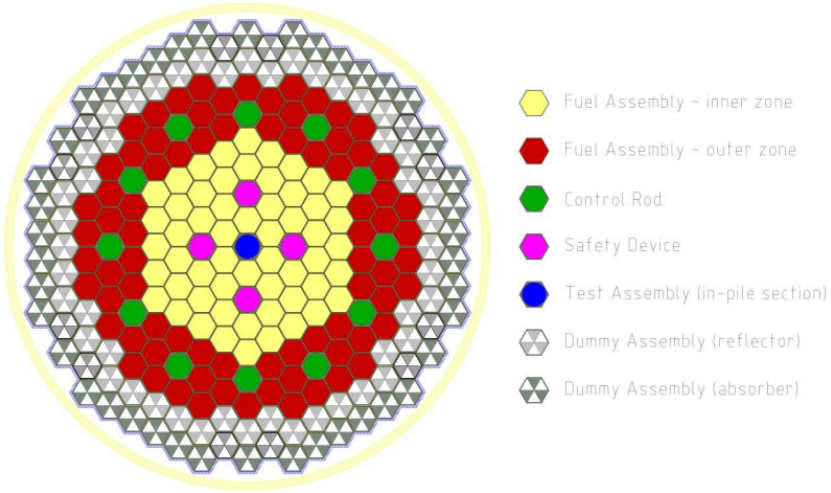

Figure 2.4: Cross sectional view of the new core map of ALFRED [13].

The main assemblies are surrounded by 102 Dummy Assemblies (DAs), arranged in two concentric rings, with the inner being the reflector, and the outer being the shielding. Through neutronic analyses, the MOX enrichment and the distribution required for assemblies with different enrichments was determined. The study aimed to:

- ensure criticality while operating;
- maintain the maximum expected burnup to 100 $\mathrm{MWd/kg_{HM}}$ with a five-batch refueling strategy (one year per sub-cycle);
- flatten the power distribution among the fuel rods and ensure the adequate reactivity worth for control and shutdown systems.

At the end of the analysis, it was decided to have 56 FAs with an enrichment of 20.5 wt.% in $PuO_{1.97}$ (inner type) and, around them, 78 FAs with an enrichment of 26.2 wt.% (outer type) [13].
After this overview of the new ALFRED core, it will be described in more detail what was simulated about the benchmark. Therefore, the design of a generic fuel pin, an FA, and a control rod assembly will be shown. It should be noted that their description will be made for a horizontal section at the height of the active zone, as the simulations shown in this thesis work will be two-dimensional.

2.2.1 The ALFRED Fuel Pin

Figure 2.5 shows the cross section of the ALFRED fuel pin, which is composed of sintered cylindrical fuel pellets enclosed in a stainless steel cladding. The pellets have a diameter of 9 mm, and an internal hole of 2 mm in diameter to reduce the pellet-cladding mechanical interaction (PCMI) at the peak burnup. The surrounding cladding is 0.6 mm thick, made of AIM1 steel, and acts as a barrier against fission gases release. There is a 0.15 mm gap between the pellets and the cladding, for assembling purposes and which contributes to preventing possible PCMI.

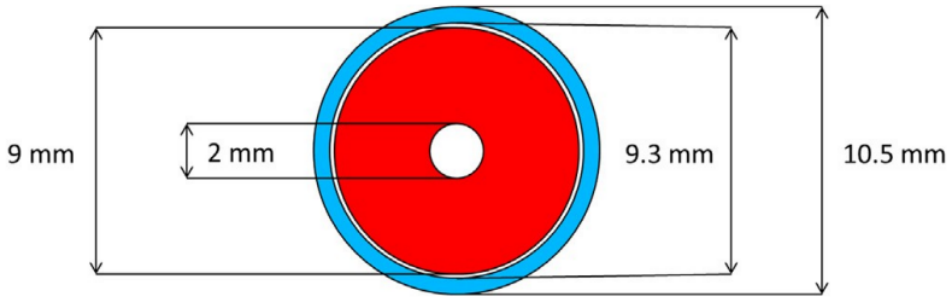

Figure 2.5: Cross section of the ALFRED fuel pin [10].

2.2.2 ALFRED Fuel Assembly

All the ALFRED assemblies have a hexagonal shape and are enclosed by AIM1 steel wrappers. The wrapper plays a crucial role in the reactor's safety, as it allows for monitoring the lead outlet temperature from each FA individually. The coolant flows both inside the wrapper -between the fuel pins- and outside it -between the various assemblies. Figure 2.6 shows a cross section of a FA at the level of the active region. Inside the wrapper, a triangular lattice identifies 127 positions, out of which 126 are occupied by fuel pins around a dummy pin at the center; the latter is present in all FAs and is used for inserting diagnostic instrumentation. The thickness of the wrapper and the pin lattice pitch are 3.5 mm and 13.6 mm, respectively. The 4 mm gap between two assemblies (dashed line) is also shown, providing for bypass lead flow.

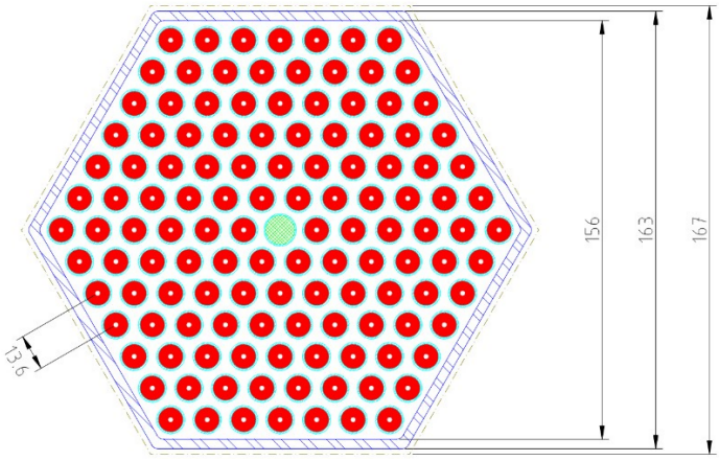

Figure 2.6: Cross section of a FA at the level of the active region (dimensions in mm) [13].

2.2.3 ALFRED Control Rod Assembly

Figure 2.7 represents the cross section of a control rod assembly (right frame) at the level of the absorber pins, which displays the 31 absorber pins inside the assembly surrounded by an AIM1 steel wrapper. The left frame of the same figure shows an equivalent representation of the latter for modelling purposes. The absorber pins within the individual control rod are made of boron carbide (B_4C) pellets, with two different ^{10}B enrichments for the lower (shutdown function) and the upper (control function) parts of the absorber column. The pins of the control part are enriched at 42 at.%, while those of shutdown one are enriched at 90 at.%. Figure 2.7 also shows the coolant flow and the bypass zones, the latter referring to the channels between the assemblies through which the lead cools the wrapper's outer surface.

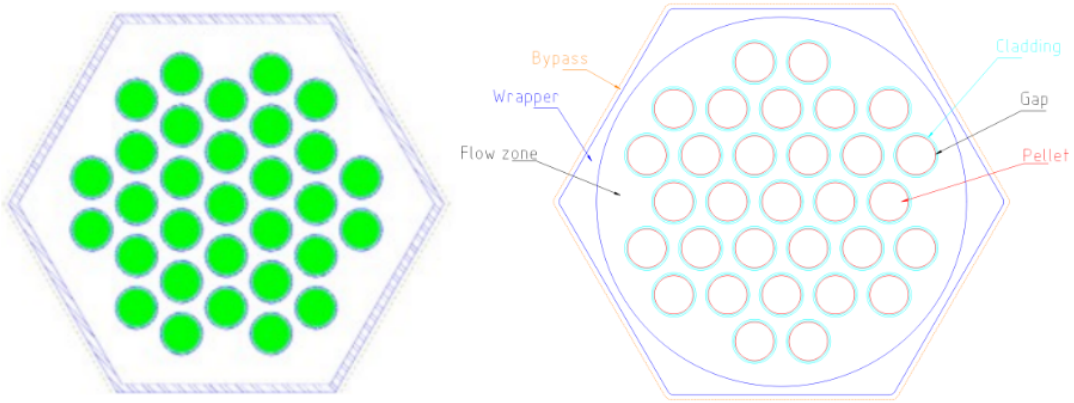

Figure 2.7: Cross section of a CR assembly at the level of the active region [17].

Chapter 3

The ECCO cell code and the ERANOS suite

This chapter provides an introduction to the European Cell COde (ECCO) and the European Reactor ANalysis Optimized calculation System (ERANOS), both of which were utilized for the benchmark activities that are the subject of this thesis. It focuses on the typical computational scheme for stationary problems, the cell flux calculation methods, and the sensitivity and uncertainty analysis procedures.

3.1 The Calculation Scheme for static calculations

The study of nuclear reactors requires the simulation of physical phenomena on a small scale, even when the geometrical domain under consideration spans several meters: this arises from the competing scales created by the neutron mean free paths in the various materials of a highly heterogeneous domain as well as macroscopic distribution of the neutron flux. To mitigate the computational cost of such simulations, it is necessary to split the calculation into two subsequent phases: a cell/lattice, and a reactor calculations. The primary objective of a cell calculation is to provide, starting from a general-purpose nuclear data library (e.g., JEFF or ENDF/B), a derived data set that is restricted and specific to the problem being analyzed. The cell code is typically applied to a limited domain, such as a single assembly, for which microscopic and macroscopic cross sections are computed through energy condensation and volume homogenization. Subsequently, for the reactor calculation, the data coming from the cell calculations are assigned to the different core regions, each one being considered homogeneous. The reactor code is then employed to solve the quasi-static transport equation and compute all the required quantities, such as integral parameters, sensitivity coefficients, and uncertainties. Other uses are possible for the reactor code, such as performing depletion calculations. For

this thesis, ECCO was used as the cell code. It is available within the ERANOS suite, which is among the reference codes for the core design of fast spectrum nuclear reactors. Within ERANOS, the BIdimensionnel Sn TRansport Optimisé (BISTRO) code is used for the reactor calculations, which allows for solving the transport (or diffusion) equation in one-dimensional or two-dimensional core geometries. It involves the discrete ordinates and the finite difference methods for discretizing neutron flight path direction and space, respectively. The overall calculation scheme that combines the two steps is schematized in Figure 3.1.

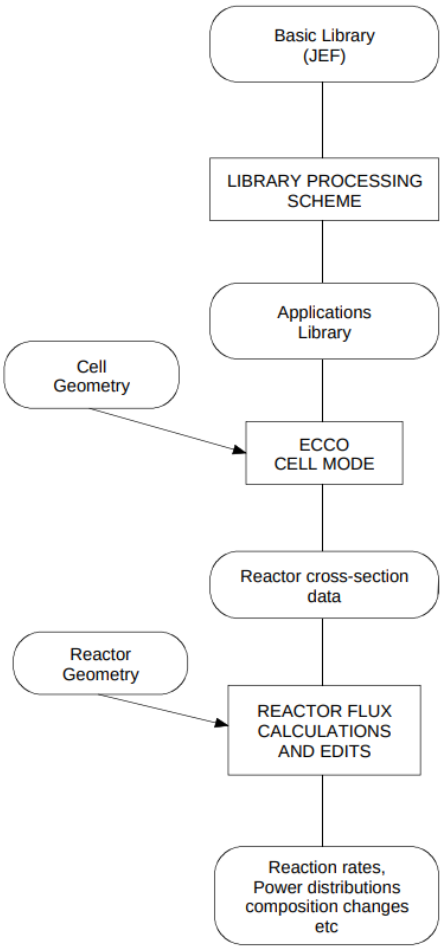

Figure 3.1: Schematic representation of the ECCO/ERANOS calculation [3].

The following section aims to briefly present the physics, mathematics, and numerical methods underlying the benchmark results discussed in this work. For a comprehensive reading, the reader is referred to the user's manual [3].

3.2 The physics of the ECCO cell code

As mentioned in the previous section, the ECCO cell code is designed to process the original libraries at 1968 (ultra-fine) energy groups (e.g., JEFF or ENDF/B) to produce the condensed cross sections for use in the reactor calculations. For computational reasons, the reactor calculations are typically performed with a smaller number of groups than those of the original libraries, and the material properties are homogenized within the calculation lattice cell. This leads to a simplified core model, but in which the cross sections and material properties were obtained using refined cells/lattices.
To perform condensation and homogenization, ECCO needs information about the geometry and materials of the cell to be analyzed. More specifically, the input data required by ECCO can be thought of as consisting of two parts: cell description and calculation procedure description. In the first part, the geometry, materials, and boundary conditions are defined, while in the second part, the number of calculation steps to be performed is specified along with the operations to be carried out in each of them.
Before analyzing the two parts just mentioned, it is important to emphasize that ECCO is a code capable of handling any type of cell, whether referring to a thermal or a fast reactor. However, the fast neutron spectrum requires certain specific considerations due to:

- the greater importance of inelastic scattering;
- the absence of a single moderator that solely determines the flux in the epithermal region;
- the greater relevance of self-shielding;
- the higher ratio between the neutron mean free path and the cell size;
- the possible need for a more accurate evaluation of the diffusion coefficient.

The aspects mentioned above are discussed in detail in the ECCO manual [3], which presents the various computation and modeling options.

3.2.1 The cell description

The geometric description of the cell entails constructing geometries with different levels of complexity, starting with simple geometric elements defined as 'links' in ECCO.' These links are of various types based on their dimensionality. They can be 0D (zero-dimensional, HOMOGENEOUS), 1D (CYLINDRICAL, PLANE), or 2D (SQUARE, RECTANGULAR LATTICE, HEXAGONAL LATTICE). More generally, links are classified as either simple or lattice-type. Each cell is represented by a tree structure, in which a simple model is a branch and a lattice is a node that capable of generating multiple

branches. The geometry is defined in a nested structure, progressing from the outermost link inward. Each link can contain other links, or be filled with a uniform material, for which the composition must be specified at a given temperature (thermal expansion coefficients can be provided to account for temperature changes). If the inner link does not completely fill the outer one, a uniform material must be defined between them.
A 'VOID' material can be used, reducing the densities of a generic material to zero. It is important to note that the allowed geometries depend on the method chosen for determining the neutron flux in the cell. For a more detailed analysis of this aspect, refer to the section on calculation methods.
The boundary condition is defined on the faces of the outermost link, except for the homogeneous cell where no conditions are required. Various boundary conditions are available in the ECCO manual, and the choice of conditions depends on the cell geometry. In summary, ECCO can treat both homogeneous and heterogeneous cells with appropriate resolution methods. Furthermore, as will be seen later, even heterogeneous cells can be homogenized automatically at some computational step of the cross sections' condensation process.

3.2.2 The calculation procedure description

The calculation procedure to produce the nuclear data library to be provided to the reactor code for the specific case requires several steps. The user usually determines the number of steps and, for each step, specifies how to handle: the geometrical schematization, the number of groups, the list of nuclides, the resonance shielding treatment, and the flux calculation. This is necessary because cross sections for different nuclides and reactions may be determined from calculations at varying levels of geometrical detail, or in different group schemes.
For example, the fine group (1968 groups in ECCO) calculations may be performed only for a homogenized cell (even if the original cell is heterogeneous) and specifically to condense elastic scattering matrices for light elements. In contrast, the standard broad group (33 groups in ECCO) calculations - utilizing the subgroup method - can be conducted for the heterogeneous version (if available) of the same cell geometry, to handle the remaining nuclides and reactions.
There are two main calculation routes already implemented in ECCO: 'Reference', and 'Fast'. The 'Reference' route consists of a fine group treatment of the elastic scattering, with the subgroup parameters also at the same fine group level for the resonance self-shielding treatment. The 'Fast' option also involves a fine group treatment of elastic scattering, but this time the subgroup parameters refer to the broad group level. Arbitrary group structures can be chosen too, keeping in mind that the outer boundaries of all the involved group structures must coincide with those of the finest group structure of the general library. More detailed information can be found in [3].
The condensation of flux, cross sections, and other useful quantities occurs whenever

transitioning from a fine group step to one with broader groups. Most of the cross sections are collapsed using flux weighting:

$$\sigma^{\mathcal{G}}_{x,e,i} = \frac{\sum_{g\in\mathcal{G}} \sigma^{g}_{x,e,i}\phi^{g}_{i}}{\phi^{G}_{i}}, \tag{3.1}$$

where:

- i is the cell region;
- e is the isotope;
- x is the reaction (e.g. total, capture, fission);
- g is the fine energy group;
- $\mathcal{G}$ is the broad energy group;
- $\phi^{G}_{i} = \sum_{g\in\mathcal{G}} \phi^{g}_{i}$ is the collapsed flux.

However, some quantities are weighted with the current instead of the flux [3].
The homogenization of quantities can be done in the calculation steps where multiple energy groups are used, or in the final step to produce data for reactor calculations. The microscopic cross sections are homogenized as a volume V, flux ϕ, and number density N weighted average [3]:

$$\sigma^{g}_{x,e} = \frac{\sum_i V_i \phi^{g}_{i} N_{e,i} \sigma^{g}_{x,e,i}}{V \phi^{g} N_e}, \tag{3.2}$$

where:

- $\phi^{g} = \dfrac{\sum_i V_i \phi^{g}_{i}}{V}$ is the homogenized flux;
- $N_e = \dfrac{\sum_i V_i N_{e,i}}{V}$ is the homogenized number density.

Following, the methods for determining the cell flux will be analyzed, as the latter is used to condense and homogenize the cross sections through a weighted average. Furthermore, grasping the method serves as the basis for understanding some choices made in Chapter 4, which is related to the benchmark results.

3.2.3 Calculation of the flux for a homogeneous cell: the fundamental mode method

The flux calculation starts from the pseudo-stationary Boltzmann equation in its integro-differential form. For position $\mathbf{r}$, neutron energy E, and neutron direction $\hat{\Omega}$, it is expressed as follows:

$$\hat{\Omega} \cdot \frac{\partial}{\partial \mathbf{r}} \Phi(\mathbf{r}, E, \hat{\Omega}) + \Sigma_t(\mathbf{r}, E)\, \Phi(\mathbf{r}, E, \hat{\Omega}) =$$

$$= \int_{4\pi} \int_0^{\infty} \Sigma_s(\mathbf{r}, E' \to E, \hat{\Omega}' \to \hat{\Omega})\, \Phi(\mathbf{r}, E', \hat{\Omega}')\, dE'\, d\hat{\Omega}' + S(\mathbf{r}, E, \hat{\Omega}), \tag{3.3}$$

where Φ is the angular neutron flux, Σ_t is the total macroscopic cross section, $\Sigma_s(\mathbf{r}, E' \to E, \hat{\Omega}' \to \hat{\Omega})$, is the double differential cross section related to the probability that an incident neutron with energy E' and direction $\hat{\Omega}'$ assumes energy E and direction $\hat{\Omega}$ through scattering, and $S(\mathbf{r}, E, \hat{\Omega})$ is the source term, which is the sum of the intrinsic fission source $S_f(\mathbf{r}, E)$ as well as all the other sources (either inside or outside the medium). In particular, considering a problem in which the source coincides with an isotropic fission source, an eigenvalue problem is obtained, with k being the eigenvalue:

$$S_f(\mathbf{r}, E) = \frac{\chi(E)}{4\pi k} \int_0^{\infty} \nu(\mathbf{r}, E') \Sigma_f(\mathbf{r}, E') \phi(\mathbf{r}, E') dE' \tag{3.4}$$

where $\nu(\mathbf{r}, E')$ represents the average number of neutrons emitted by fission induced at the energy E' and $\chi(E)$ is the fission spectrum. If a homogeneous and generally isotropic medium is considered, the equations become [16] :

$$\hat{\Omega} \cdot \frac{\partial}{\partial \mathbf{r}} \Phi(\mathbf{r}, E, \hat{\Omega}) + \Sigma_t(E)\, \Phi(\mathbf{r}, E, \hat{\Omega}) =$$

$$= \int_{4\pi} \int_0^{\infty} \Sigma_s(E' \to E, \hat{\Omega}' \to \hat{\Omega})\, \Phi(\mathbf{r}, E', \hat{\Omega}')\, dE'\, d\hat{\Omega}' + S(\mathbf{r}, E, \hat{\Omega}), \tag{3.5}$$

$$S_f(\mathbf{r}, E) = \frac{\chi(E)}{4\pi k} \int_0^{\infty} \nu(E') \Sigma_f(E') \phi(\mathbf{r}, E') dE'. \tag{3.6}$$

Notice that the cross sections in Eqs. (3.5) and (3.6) do not depend on $\mathbf{r}$, as the medium is homogeneous, and on $\hat{\Omega}$, as the medium is isotropic.
The first simplification that can be made in Eqs. (3.5) and (3.6) - for solving them numerically - is to turn the continuous energy variable into a discrete one, which is done by applying the multigroup approximation. In practice, the continuous variable E is divided into G intervals - the generic one being g of width ΔE_g - within which multigroup constants are defined while preserving the reaction rates.

For example, the macroscopic cross section for group g and generic reaction x is given by:

$$\Sigma_x^g = \frac{\int_{\Delta E_g} \Sigma_x(E)\phi(\mathbf{r},E)\,dE}{\phi^g(\mathbf{r})} \quad ; \quad g = 1,\ldots,\mathrm{G}, \tag{3.7}$$

where

$$\phi^g(\mathbf{r}) = \int_{\Delta E_g} \phi(\mathbf{r},E)\,dE. \tag{3.8}$$

The scalar neutron flux is used as a weighting function instead of the angular neutron flux when considering the averaging of macroscopic cross sections because it preserves the isotropy of the medium [15]. However, this means that the group averaged cross sections depend on the neutron flux, i.e. quantity that is to be determined. A system of G equations is obtained by formally integrating the neutron transport equation on a given energy group ΔE_g, which are coupled by the scattering source (yet to be defined) and the fission terms:

$$\hat{\Omega}\cdot\frac{\partial}{\partial\mathbf{r}}\Phi^g(\mathbf{r},\hat{\Omega}) + \Sigma_t^g\,\Phi^g(\mathbf{r},\hat{\Omega}) =$$

$$= \sum_{g'=1}^{G}\int_{4\pi}\Sigma_s^{g'\to g}(\hat{\Omega}'\to\hat{\Omega})\,\Phi^{g'}(\mathbf{r},\hat{\Omega}')\,d\hat{\Omega}' + S^g(\mathbf{r},\hat{\Omega}), \tag{3.9}$$

$$S_f^g(\mathbf{r}) = \frac{\chi^g}{4\pi k}\sum_{g'=1}^{G}\nu^{g'}\Sigma_f^{g'}\phi^{g'}(\mathbf{r}). \tag{3.10}$$

From now onwards, for the treatment of the fundamental method, the source $S^g(\mathbf{r},\hat{\Omega})$, which includes the extrinsic term and the fission source, will be treated as a generic source, though it should be remembered that the fission source represented by Eq. (3.10) depends on the flux and will therefore be handled in ECCO through iterative algorithms. Furthermore, in the ECCO manual [3], the solution for a homogeneous infinite medium with a constant and isotropic source in group g is given, where the flux in each group is isotropic and spatially constant, so the solution becomes:

$$\phi^g = \frac{S^g}{\Sigma_r^g}, \tag{3.11}$$

where:

- ϕ^g is the position-independent scalar neutron flux for group g (any scalar neutron flux is formally obtained by angular integration of the corresponding angular neutron flux),
- S^g is the position-independent fission and scattering source for group g,

- Σ_r^g is the removal macroscopic cross section for group g, and is given by

$$\Sigma_r^g = \Sigma_t^g - \Sigma_{el}^{gg} - \Sigma_{in}^{gg} - \Sigma_{(n,Xn)}^{gg},$$

  in which:

  - Σ_t^g is the total macroscopic cross section for group g,
  - Σ_{el}^{gg} is the elastic macroscopic cross section within group g, i.e. in which the incident neutron energy remains in the group g after the scattering,
  - Σ_{in}^{gg} is the inelastic macroscopic cross section within group g,
  - $\Sigma_{(n,Xn)}^{gg}$ is the macroscopic cross section for (n, Xn) reactions within group g.

For a finite homogeneous medium, on the other hand, the angular flux can vary with space and it can be assumed that its spatial variations and those of the source follow the fundamental mode shape determined by the square root of buckling (B^2). The angular flux and the source for group g can therefore be written as the product of an angle-dependent term and a space-dependent one [7]:

$$\Phi^g(\mathbf{r}, \hat{\Omega}) = \psi^g(\hat{\Omega}) e^{\mathrm{iB}\mathbf{r}} \quad S^g(\mathbf{r}, \hat{\Omega}) = S^g(\hat{\Omega}) e^{\mathrm{iB}\mathbf{r}} \tag{3.12}$$

Now, for simplicity, let's consider the one-dimensional case in plane geometry and recall that for an isotropic medium in the case of elastic scattering with rotational invariance (independence from the azimuthal angle φ), the following holds:

$$\Sigma_s^{g' \to g}(\hat{\Omega}' \to \hat{\Omega}) = \Sigma_s^{g' \to g}(\hat{\Omega}' \cdot \hat{\Omega}) = \Sigma_s^{g' \to g}(\mu_0), \tag{3.13}$$

in which μ_0 is the cosine of the scattering angle ϑ_0 in the laboratory reference system. For it, the following can be written [16]:

$$\hat{\Omega}' \cdot \hat{\Omega} = \cos\vartheta_0 = \mu_0 = \mu\mu' + \sqrt{1-\mu^2}\sqrt{1-\mu'^2}\cos(\varphi - \varphi'), \tag{3.14}$$

where:

- $\hat{\Omega}'$ is the neutron flight direction before the scattering event in the laboratory reference frame;
- $\hat{\Omega}$ is the neutron flight direction after the scattering event in the laboratory reference frame;
- $\mu' = \cos\vartheta'$, with ϑ' being the polar angle (with respect to the polar axis x) of the neutron before the scattering event in the laboratory reference frame;
- $\mu = \cos\vartheta$, with ϑ being the polar angle of the neutron after the scattering event in the laboratory reference frame;

- φ' is the azimuthal angle of the neutron before the scattering event in the laboratory reference frame;
- φ is the azimuthal angle of the neutron after the scattering event in the laboratory reference frame.

With these assumptions, the system of G equations represented by Eq. (3.9), becomes:

$$\mu\frac{\partial}{\partial x}\Phi^g(x,\mu)+\Sigma_t^g\,\Phi^g(x,\mu)=$$

$$=\sum_{g'}^{G}\int_{-1}^{1}\int_{0}^{2\pi}\Sigma_s^{g'\to g}(\mu_0)\,\Phi^{g'}(x,\mu')\,d\varphi' d\mu'+S^g(x,\mu), \tag{3.15}$$

in which the following modifications have been made in accordance with the one-dimensional geometry:

$$S(\mathbf{r},\hat{\Omega})\to S(x,\mu)$$
$$\Phi(\mathbf{r},\hat{\Omega})\to\Phi(x,\mu)$$
$$\hat{\Omega}\cdot\frac{\partial}{\partial\mathbf{r}}\to\mu\frac{\partial}{\partial x},$$

where x is the polar axis coordinate to which the polar angles refer to.
Substituting the expressions for the flux and the source (Eq. (3.12)) and dividing everything by e^{iBx}, the following is obtained:

$$\mu\mathrm{iB}\psi^{\mathrm{g}}(\mu)+\Sigma_{\mathrm{t}}^{\mathrm{g}}\,\psi^{\mathrm{g}}(\mu)=\sum_{\mathrm{g}'}^{\mathrm{G}}\int_{-1}^{1}\int_{0}^{2\pi}\Sigma_{\mathrm{s}}^{\mathrm{g}'\to\mathrm{g}}(\mu_0)\,\psi^{\mathrm{g}'}(\mu')\,\mathrm{d}\varphi'\mathrm{d}\mu'+\mathrm{S}^{\mathrm{g}}(\mu) \tag{3.16}$$

At this point, the angular dependence can be expressed using Legendre polynomials (for functions not depending on φ, spherical harmonics reduce to Legendre polynomials), which form a complete set of orthogonal functions over the interval $[-1,1]$. These polynomials are denoted by $P_\ell(\mu)$. Since they constitute a complete orthogonal set, any function depending on $\mu\in[-1,1]$ can be expanded in a series of the $P_\ell(\mu)$. Therefore, the following series expansions are substituted into the system of Eq. (3.16):

$$\begin{aligned}
\Sigma_s^{g'\to g}(\mu_0)&=\sum_{\ell=0}^{\infty}\frac{2\ell+1}{4\pi}\Sigma_{s,\ell}^{g'\to g}P_\ell(\mu_0)\quad\text{with}\quad\Sigma_{s,\ell}^{g'\to g}=2\pi\int_{-1}^{1}P_\ell(\mu_0)\Sigma_s^{g'\to g}(\mu_0)\,d\mu_0,\\
\psi^g(\mu)&=\sum_{\ell=0}^{\infty}\frac{2\ell+1}{4\pi}\psi_\ell^g P_\ell(\mu)\quad\text{with}\quad\psi_\ell^g=2\pi\int_{-1}^{1}P_\ell(\mu)\psi^g(\mu)\,d\mu,\\
S^g(\mu)&=\sum_{\ell=0}^{\infty}\frac{2\ell+1}{4\pi}S_\ell^g P_\ell(\mu)\quad\text{with}\quad S_\ell^g=2\pi\int_{-1}^{1}P_\ell(\mu)S^g(\mu)\,d\mu.
\end{aligned} \tag{3.17}$$

Before substituting the expressions into Eq. (3.16), it is useful to rewrite the scattering term as a function of μ' [16], since the integral is over μ' and not μ_0. The scattering term in Eq. (3.16) becomes:

$$\begin{aligned}
&\sum_{g'=1}^{G}\int_{-1}^{1}\int_{0}^{2\pi}\Sigma_s^{g'\to g}(\mu_0)\,\psi^{g'}(\mu')\,d\varphi' d\mu' = \\
&=\sum_{g'=1}^{G}\int_{-1}^{1}\int_{0}^{2\pi}\sum_{\ell=0}^{\infty}\frac{2\ell+1}{4\pi}\Sigma_{s,\ell}^{g'\to g}P_\ell(\mu_0)\psi^{g'}(\mu')\,d\varphi' d\mu' = \\
&=\sum_{g'=1}^{G}\sum_{\ell=0}^{\infty}\frac{2\ell+1}{4\pi}\Sigma_{s,\ell}^{g'\to g}P_\ell(\mu)2\pi\int_{-1}^{1}P_\ell(\mu')\psi^{g'}(\mu')\,d\mu'
\end{aligned} \tag{3.18}$$

where the addition theorem for Legendre polynomials has been applied, and the independence from the angles φ and φ' has been exploited. At this point, by substituting the scattering term and the series expansions, the following is obtained:

$$\begin{aligned}
&\sum_{\ell=0}^{\infty}\mu\mathrm{iB}\frac{2\ell+1}{4\pi}\psi_\ell^{\mathrm{g}}\mathrm{P}_\ell(\mu)+\Sigma_{\mathrm{t}}^{\mathrm{g}}\sum_{\ell=0}^{\infty}\frac{2\ell+1}{4\pi}\psi_\ell^{\mathrm{g}}\mathrm{P}_\ell(\mu) = \\
&=\sum_{g'}^{G}\sum_{\ell=0}^{\infty}\frac{2\ell+1}{4\pi}\Sigma_{s,\ell}^{g'\to g}P_\ell(\mu)2\pi\int_{-1}^{1}P_\ell(\mu')\psi^{g'}(\mu')\,d\mu'+\sum_{\ell=0}^{\infty}\frac{2\ell+1}{4\pi}S_\ell^g P_\ell(\mu)
\end{aligned} \tag{3.19}$$

Recalling the orthogonality property of the Legendre polynomials, it is noted that

$$2\pi\int_{-1}^{1}P_\ell(\mu')\psi^{g'}(\mu')\,d\mu' = \psi_\ell^{g'}. \tag{3.20}$$

Thus, by substituting into the equation, the following is obtained:

$$\begin{aligned}
&\sum_{\ell=0}^{\infty}\mu\mathrm{iB}\frac{2\ell+1}{4\pi}\psi_\ell^{\mathrm{g}}\mathrm{P}_\ell(\mu)+\Sigma_{\mathrm{t}}^{\mathrm{g}}\sum_{\ell=0}^{\infty}\frac{2\ell+1}{4\pi}\psi_\ell^{\mathrm{g}}\mathrm{P}_\ell(\mu) = \\
&=\sum_{g'=1}^{G}\sum_{\ell=0}^{\infty}\frac{2\ell+1}{4\pi}\Sigma_{s,\ell}^{g'\to g}P_\ell(\mu)\psi_\ell^{g'}+\sum_{\ell=0}^{\infty}\frac{2\ell+1}{4\pi}S_\ell^g P_\ell(\mu).
\end{aligned} \tag{3.21}$$

At this point, $(2\ell+1)\mu P_\ell(\mu)$ can be replaced using the recurrence formula of the Legendre polynomials, and the entire equation is multiplied by P_m. Integration over μ from $[-1,1]$ and the use of the orthogonality property transforms each equation for each group g (see Eq. (3.21)) into a system of infinite equations, with the moments of the flux ψ_ℓ^g as the unknown. For them, the following recursive formula can be used:

$$\frac{\ell+1}{2\ell+1}\mathrm{iB}\psi_{\ell+1}^{\mathrm{g}}+\frac{\ell}{2\ell+1}\mathrm{iB}\psi_{\ell-1}^{\mathrm{g}}+\Sigma_{\mathrm{t}}^{\mathrm{g}}\psi_\ell^{\mathrm{g}}=\sum_{\mathrm{g}'=1}^{\mathrm{G}}\Sigma_{\mathrm{s},\ell}^{\mathrm{g}'\to\mathrm{g}}\psi_\ell^{\mathrm{g}'}+\mathrm{S}_\ell^{\mathrm{g}}. \tag{3.22}$$

From now onwards, for simplicity, the group index g will only appear in the coupling terms. since the focus will be on solving the system of infinite equations for a specific group. To do this, an approximation is necessary, as it is impossible to solve infinite equations. A possibility is to use the P_N consistent method - this was the method adopted in ECCO for the benchmarking activities of this work -, through which the infinite system is reduced to N equations by imposing that the flux moment of order $\ell = N + 1$ is equal to zero: $\psi_{N+1} = 0$. With this assumption, the system of equations for $\psi_0, \psi_1, \ldots, \psi_N$, after being rearranged, becomes [2]:

$$\begin{aligned} &\mathrm{iB}\psi_1 + \Sigma_\mathrm{t}\psi_0 = \sum_{\mathrm{g}'} \Sigma_{\mathrm{s},0}^{\mathrm{g}'\to\mathrm{g}}\psi_0^{\mathrm{g}'} + \mathrm{S}_0; \quad \ell = 0, \\ &\frac{\mathrm{iB}}{3}\psi_0 + A_1(B,N)\psi_1 = \sum_{g'} \Sigma_{s,1}^{g'\to g}\psi_1^{g'} + S_1; \quad \ell = 1, \\ &\psi_\ell = -\frac{\ell}{2\ell+1}\frac{\mathrm{iB}\psi_{\ell-1}}{A_\ell(B,N)}; \quad \ell = 2, \ldots, N. \end{aligned} \tag{3.23}$$

The transport-like cross sections, A_ℓ [3], depend on B and the order N.
For $\ell = 1, ..., N-1$ a continued fraction expresses them:

$$\mathrm{A}_\ell = \mathrm{b}_{\ell-1} + \cfrac{\mathrm{a}_\ell}{\mathrm{b}_\ell + \cfrac{\mathrm{a}_{\ell+1}}{\mathrm{b}_{\ell+1} + ... + \cfrac{\mathrm{a}_{\mathrm{N}-1}}{\mathrm{b}_{\mathrm{N}-1}}}}, \tag{3.24}$$

while, for $\ell = \mathrm{N}$, they are given by

$$A_N = b_{N-1}. \tag{3.25}$$

The quantities a_ℓ are required for $\ell = 1, ..., N-1$ and are given by

$$\mathrm{a}_\ell = \frac{(\ell+1)^2 B^2}{(2\ell+1)(2\ell+3)}. \tag{3.26}$$

Considering b_ℓ:

- If $\ell = 0$, $b_0 = \Sigma_t$;
- If $\ell > 0$, $b_\ell = \Sigma_t - \Sigma_{s^*,\ell+1}$, where $\Sigma_{s^*,\ell+1} = \sum_{g'\neq g} \Sigma_{s,\ell+1}^{g'\to g}$ is the $(\ell+1)$-th moment of scattering cross section with $(\ell+1)$-th moment self-scattering correction.

Before considering the specific case of the P_1 approximation, that is, truncating the system of infinite equations by imposing $\psi_2 = 0$, it is important to highlight that the moments ψ_ℓ are complex quantities. In particular, if the buckling B^2 is positive, there is

an alternation of real and imaginary moments. To express the solutions as real quantities, they must be obtained using the following equation [3]:

$$\psi_\ell = \mathrm{i}^\ell \psi_\ell; \quad \ell = 2, \ldots, \mathrm{N}.$$

For $\ell = 0$, $\psi_0 = \phi$ is the scalar flux. For $\ell = 1$, $\psi_1 = J$ is the current.
Proceeding with the P_1 approximation and substituting the zero and first-order flux moments, the system in Eq. (3.27) becomes:

$$\begin{aligned} BJ + \Sigma_t \phi &= \sum_{g'}^{G}, \Sigma_{s,0}^{g' \to g} \phi^{g'} + S_0 \\ \frac{-B}{3}\phi + \Sigma_t J &= \sum_{g'}^{G} \Sigma_{s,1}^{g' \to g} J^{g'} + S_1. \end{aligned} \tag{3.27}$$

This system thus becomes solvable once the flux and current for the other groups are known. For this reason, iterative algorithms will be used, in which at each cycle the sources for group g (including positive scattering terms from $g' \to g$) are computed from the previous cycle. This process will repeat until consistency between sources and fluxes is achieved.

3.2.4 Calculation of the flux for a heterogeneous cell, the collision probabilities method

The flux for a heterogeneous medium is generally found using the collision probability method. This method solves the Boltzmann equation in its steady-state integral form. The advantage of an integral approach lies in the fact that it allows for the assumption of isotropic scattering and sources in the laboratory system. This assumption eliminates the directional variable $\hat{\Omega}$, which is not possible when solving the integral-differential transport equation. Anisotropies can still be considered using the 'transport correction' [15]. This correction involves truncating the expansion of the macroscopic scattering cross section in Legendre polynomials up to order m while retaining anisotropy up to order $m + 1$. This is achieved by adding a corrective term to the macroscopic scattering cross section. Considering the monoenergetic case, the aforementioned correction, which is obtained by truncating the series at $m = 0$ [15], is:

$$\Sigma_{s0}^0(\mathbf{r}) = \Sigma_{s0}(\mathbf{r}) - \Sigma_{s1}(\mathbf{r}) \tag{3.28}$$

$$\Sigma_{s0}^0(\mathbf{r}) = \Sigma_{s0}(\mathbf{r}) - \Sigma_{s1}(\mathbf{r}) \tag{3.29}$$

where:

- $\Sigma_{s0}^0(\mathbf{r})$ is the transport-corrected macroscopic scattering cross section;

- $\Sigma_{s0}(\mathbf{r})$ is the zeroth-order moment of the macroscopic scattering cross section;
- $\Sigma_{s1}(\mathbf{r})$ is the first-order moment of the macroscopic scattering cross section.

Σ^0_{s0} can be rewritten by substituting $\Sigma_{s1} = \mu\Sigma_0$, with μ cosine of the scattering angle in the laboratory reference frame.

$$\Sigma^0_{s0}(\mathbf{r}) = [1 - \mu(\mathbf{r})]\,\Sigma_{s0}(\mathbf{r}). \tag{3.30}$$

The whole can be repeated for the multigroup case:

$$\Sigma^0_{s0,g'\to g}(\mathbf{r}) = \Sigma_{s0,g'\to g}(\mathbf{r}) - \delta_{gg'}\sum_{g=1}^{G}\Sigma_{s1,g'\to g}(\mathbf{r}). \tag{3.31}$$

With this consideration, the integral equation becomes [15]:

$$\phi(\mathbf{r}, E) = \int_V Q\left(\mathbf{r}', E\right)\frac{\exp\left[-\tau\left(\mathbf{r}, \mathbf{r}', E\right)\right]}{4\pi\left|\mathbf{r} - \mathbf{r}'\right|^2}d_3\mathbf{r}'. \tag{3.32}$$

where τ is the optical path length and the source Q is given by:

$$Q\left(\mathbf{r}', E\right) = \int_0^\infty\left[\Sigma^0_{s0}\left(\mathbf{r}', E' \to E\right) + \frac{\chi\left(\mathbf{r}', E\right)}{k}\nu\left(\mathbf{r}', E'\right)\Sigma_f\left(\mathbf{r}', E'\right)\right]\phi\left(\mathbf{r}', E'\right)dE'. \tag{3.33}$$

The collision probability method solves the Eq. (3.32) through spatial discretization. The domain is divided into $\mathcal{R}$ regions where neutron parameters are considered constant. Furthermore, if the regions V_j (with $j = 1, \ldots, \mathcal{R}$) are sufficiently small, a constant source can be assumed within each region. This consideration is very important as it greatly simplifies the calculation of probabilities, as will be shown later.
The discretized form of Eq. (3.32) becomes:

$$\phi(\mathbf{r}, E) = \sum_{j=1}^{\mathcal{R}}\int_{V_j}\frac{\exp\left[-\tau\left(\mathbf{r}, \mathbf{r}', E\right)\right]}{4\pi\left|\mathbf{r} - \mathbf{r}'\right|^2}Q\left(\mathbf{r}', E\right)d_3\mathbf{r}'. \tag{3.34}$$

The equation solved by the method is obtained by multiplying Eq. (3.34) by the transport-corrected total cross section [15], $\Sigma^0_t(\mathbf{r}, E) = \Sigma_a(\mathbf{r}, E) + \Sigma^0_s(\mathbf{r}, E)$, and integrating it over a volume V_i:

$$\int_{V_i}\Sigma^0_t(\mathbf{r}, E)\phi(\mathbf{r}, E)d_3\mathbf{r} = \sum_{j=1}^{\mathcal{R}}\int_{V_j}Q\left(\mathbf{r}', E\right)\int_{V_i}\Sigma^0_t(\mathbf{r}, E)\frac{\exp\left[-\tau\left(\mathbf{r}, \mathbf{r}', E\right)\right]}{4\pi\left|\mathbf{r} - \mathbf{r}'\right|^2}d_3\mathbf{r}d_3\mathbf{r}'. \tag{3.35}$$

The equation then becomes:

$$\Sigma^0_{t,i}(E)\phi_i(E)V_i = \sum_{j=1}^{\mathcal{R}}P_{j\to i}(E)Q_j(E)V_j, \tag{3.36}$$

with the following volume average quantities preserving reaction rates:

- $\phi_i(E) = \frac{1}{V_i} \int_{V_i} \phi(\mathbf{r}, E) d_3\mathbf{r}$;
- $Q_j(E) = \frac{1}{V_j} \int_{V_j} Q(\mathbf{r}, E) d_3\mathbf{r}$;
- $\Sigma^0_{t,i}(E) = \frac{\int_{V_i} \Sigma^0_t(\mathbf{r}, E)\phi(\mathbf{r}, E) d_3\mathbf{r}}{V_i \phi_i(E)}$.

$P_{j\to i}$ is the probability that a neutron emitted isotropically in region V_j collides for the first time in region V_i. it is defined as:

$$P_{j\to i}(E) = \frac{\int_{V_j} Q(\mathbf{r}', E) \int_{V_i} \Sigma^0_t(\mathbf{r}, E) \frac{\exp[-\tau(\mathbf{r}, \mathbf{r}', E)]}{4\pi |\mathbf{r} - \mathbf{r}'|^2} d_3\mathbf{r} d_3\mathbf{r}'}{\int_{V_j} Q(\mathbf{r}', E)\, d_3\mathbf{r}'}. \tag{3.37}$$

Eq. (3.37) is further simplified by considering the assumption of small V_j, in which the source $Q(\mathbf{r}, E)$ is uniform. It becomes:

$$P_{j\to i}(E) = \frac{\Sigma^0_{t,i}(E)}{V_j} \int_{V_j} \int_{V_i} \frac{\exp[-\tau(\mathbf{r}, \mathbf{r}', E)]}{4\pi |\mathbf{r} - \mathbf{r}'|^2} d_3\mathbf{r} d_3\mathbf{r}'. \tag{3.38}$$

Eq. (3.38) thus expresses the probability that a neutron, generated uniformly and isotropically in region V_j, will undergo its first collision in region V_i.
However, to apply the collision probability method to a finite cell, additional quantities need to be defined. These will not be derived in this work; for interested readers, refer to pages 125-127 of reference [15]. To understand the definition of the quantities in the integrals, see Figure 3.2.
The quantity to define is:

$$P_{i\to S}(E) = \frac{1}{V_i} \int_{V_i} \int_S \frac{\exp[-\tau(\mathbf{r}', \mathbf{r}, E)]}{4\pi |\mathbf{r} - \mathbf{r}'|^2} \left|\hat{\Omega} \cdot \mathbf{N}'\right| d_2\mathbf{r}' d_3\mathbf{r}, \tag{3.39}$$

where $P_{i\to S}(E)$ represents the escape probability, i.e., the probability that a neutron emitted isotropically and uniformly in volume V_i exits the surface S of the cell without colliding (without interacting).
This quantity is also calculated as $P_{i\to S} = 1 - P_{i\to i}$.

$$P_{S\to i}(E) = \frac{\Sigma^0_{t,i}(E)}{\pi S} \int_S |\hat{\Omega} \cdot \mathbf{N}| \int_{V_i} \frac{\exp[-\tau(\mathbf{r}', \mathbf{r}, E)]}{|\mathbf{r} - \mathbf{r}'|^2} d_3\mathbf{r} d_2\mathbf{r}', \tag{3.40}$$

where $P_{S\to i}(E)$ represents the probability of collision in i for a neutron entering isotropically and homogeneously through the surface S. This quantity is also calculated as

$P_{S\to i} = \dfrac{4V_i}{S}\Sigma^0_{t,i}P_{i\to S}$.

$$P_{S\to S}(E) = \frac{1}{\pi S}\int_S |\hat{\Omega}\cdot\mathbf{N}| \int_S \frac{\exp\left[-\tau\left(\mathbf{r}',\mathbf{r},E\right)\right]}{\left|\mathbf{r}-\mathbf{r}'\right|^2}\left|\hat{\Omega}\cdot\mathbf{N}'\right| d_2\mathbf{r}'d_2\mathbf{r}, \tag{3.41}$$

where $P_{S\to S}(E)$ represents the transmission probability, i.e., the probability that a neutron has to homogeneously and isotropically enter cell i by traversing surface S, and exit the cell without colliding. This quantity is also calculated as $P_{S\to S} = 1 - P_{S\to i}$.

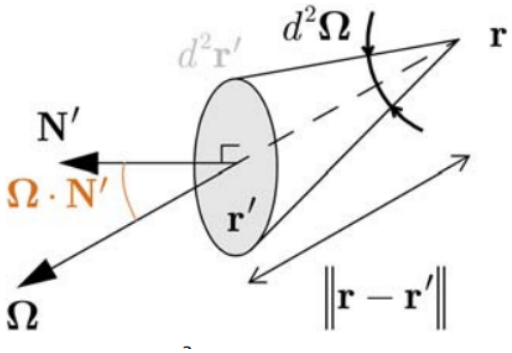

Figure 3.2: Illustration of the solid angle $d_2\hat{\Omega}$ embedding an elementary surface $d_2\boldsymbol{r}'$ from a point $\mathbf{r}$ [15].

After analyzing the quantities involved, it is possible to define the steps for solving Eq. (3.36). The solution proceeds in two steps. The first step involves solving the collision probabilities defined previously, while the second step involves calculating the fluxes by solving a linear system. The computational challenge thus lies in the double integrals of the collision probabilities, especially for more complex geometries.
Before briefly describing approximate methods for calculations in complex geometries, it is worth highlighting that the above description is useful if one wants to calculate the scalar flux. However, it is also possible to calculate the angular flux without eliminating the angle $\hat{\Omega}$ from the variables; in this case, directional collision probabilities are considered. Moreover, a problem common to both types of calculation is that, for empty or low-density regions, the $P_{j\to i}$ tends to zero along with the $\Sigma^0_{t,i}$ (see Eq. (3.38)). To address this issue, reduced collision probabilities are used, which remain finite as the density approaches zero:

$$p_{j\to i} = \frac{P_{j\to i}}{\Sigma^0_{t,i}}. \tag{3.42}$$

Returning to approximate methods, in ECCO, one of them is the Roth method, which is heavily involved in this work. It decomposes complex geometries into elementary 'links' (usually one-dimensional), for which exact routines can be applied, and then combines

the results to yield the probability matrix of the entire cell. The calculation consists of three main steps. Here for, simplicity, a cell decomposed into two links, named X and Y respectively, is considered.

- Phase 1:
  - Calculation of the collision probabilities within link X, $P^X_{i\to j}$, where i and j are the regions inside link X,
  - Calculation of the escape probability $P^X_{i\to S} = 1 - \sum_j P^X_{i\to j}$;
- Phase 2: Calculation of the probability $\mathcal{P}_{XY}$ that a neutron exiting the surface of link X reaches the surface of link Y. It is calculated as:

$$\mathcal{P}_{XY} = R_{XY} + \sum_{\kappa=1}^{\mathcal{L}} R_{X\kappa} P^{\kappa}_{S\to S}\, \mathcal{P}_{\kappa Y}, \tag{3.43}$$

  where:
  - $\mathcal{L}$ is the number of links (in this case, $\mathcal{L} = 2$),
  - R_{XY} and $R_{X\kappa}$ are the number of neutrons that reach link Y and link κ, respectively, for a neutron leaving link X (without crossing any other link). These are geometric quantities that depend on the average of the external surfaces between the links,
  - $P^{\kappa}_{S\to S}$ is the probability that the neutron passes through link κ without colliding, and it is calculated as $P^{\kappa}_{S\to S} = 1 - \sum_i P^{\kappa}_{S\to i} = 1 - \sum_i \frac{4V_i}{S}\Sigma_{t,i} P^{\kappa}_{i\to S}$,
  - $\mathcal{P}_{\kappa Y}$ is the probability that a neutron exiting the surface of link κ reaches the surface of link Y;
- Phase 3: Linear combination of the results obtained from the previous phases, in order to calculate the probability that a neutron born in region i of link X collides for the first time in region j of link B, which is calculated as:

$$\begin{aligned} &P_{i_X\to j_Y} = P^X_{i\to j} + P^X_{i\to S}\mathcal{P}_{XY}P^Y_{S\to j} && \text{if } X = Y,\\ &P_{i_X\to j_Y} = P^X_{i\to S}\mathcal{P}_{XY}P^Y_{S\to j} && \text{if } X \neq Y, \end{aligned} \tag{3.44}$$

  which can be compacted using the Kronecker delta function:

  $P_{i_X\to j_Y} = \delta_{XY}P^X_{i\to j} + P^X_{i\to S}\mathcal{P}_{XY}P^Y_{S\to j}$.

The Roth method has been further improved to provide a more accurate calculation of collision probabilities. In practice, it has been decided to divide the surface of the link into several faces, with the number varying depending on the geometry, and to calculate

not a single transmission probability for the link $P^X_{S\to S}$, but multiple transmission probabilities $P^X_{S_\alpha\to S_\beta}$, where α and β are the faces of the link considered. This improvement led to the Roth 4 method for rectangular lattices and the Roth 6 method for hexagonal lattices. Finally, there is another method in ECCO, used for special situations (e.g., HEXAGONAL LATTICE IN HEXAGON), called the Double Step method. It involves dividing the geometry into an isolated internal link and an external one considered infinite, applying the Roth method to both.
In general, until version 1.2 of the code, only the first two levels were calculated for geometries with two or more levels, i.e. the calculation only solved the first nesting level using the Double Step method. Three types of nesting were permitted:

- hexagonal lattice in a hexagon;
- rectangular lattice in a square;
- cylinder in a cylinder.

Since version 2.0 a new calculation method has been defined that overcomes these limitations, so it is possible to define and solve (previously described but not solved) multi-level nesting geometries in which all links are allowed. This method, born from the combination of the Double Step (calculates the collision probabilities between the regions of two nested links) and Roth (calculates the collision probabilities between the areas of two links located within the same lattice) methods, is called the General method and is called up by the code by default, whenever the cell is solved in heterogeneous geometry. Currently, it is still possible to define the old methods for cells that allow it. For more details on the General method and its validation, it is possible to refer to the report [4].

3.3 The Flux Calculation in BISTRO, the S_N Method

As previously mentioned, the flux calculation for the reactor is carried out within the ERANOS suite. The BISTRO code is used to solve the 1D and 2D integro-differential transport equations using the discrete ordinates method, commonly referred to as S_N method. In this section, the S_N method will be explained under the assumption of the equation:

- monoenergetic;
- monodimensional (plane geometry);
- isotropic scattering and fission source.

Adopting these assumptions aims to simplify the discussion, focusing on the peculiarity of the discrete ordinates method, which solves the transport equation by discretizing the

angular variable into N finite directions.
With the given assumptions, the integrodifferential transport equation becomes:

$$\mu\frac{\partial\Phi(x,\mu)}{\partial x}+\Sigma_t(x)\Phi(x,\mu)=\frac{1}{2}(\Sigma_s(x)+\frac{\nu\Sigma_f(x)}{k})\int_{-1}^{1}\Phi(x,\mu')d\mu'+S_{ext}(x,\mu). \quad (3.45)$$

To solve Eq. (3.45), N discrete flight directions and weight coefficients are defined. The discretization of the flight directions results in μ_n $(n=1,...,N)$, the cosines used to describe the angular variable, while the weight coefficients w_n $(n=1,...,N)$ are used to approximate the integral using the quadrature formula:

$$\int_{-1}^{1}\Phi(x,\mu')\,d\mu'\approx\sum_{n=1}^{N}w_n\Phi(x,\mu_n). \quad (3.46)$$

With this discretization, a single equation in the continuous variables (x,μ) is turned into N equations - continuous in the variable x, but discrete in the variable μ - which take the form:

$$\mu_j\frac{\partial\Phi(x,\mu_j)}{\partial x}+\Sigma_t(x)\Phi(x,\mu_j)=\frac{1}{2}(\Sigma_s(x)+\frac{\nu\Sigma_f(x)}{k})\sum_{n=1}^{N}w_n\Phi(x,\mu_n)+S_{ext}(x,\mu_j), \quad (3.47)$$

$j=1,...,N.$

Some aspects related to the weight functions w_n and the discrete ordinates μ_n need to be highlighted. Typically, an even number of μ_n values, symmetric about $\mu=0$, are chosen. It is given that for $n=1,...\frac{N}{2}$:

$$\mu_n>0 \quad \mu_{N+1-n}=-\mu_n \quad w_{N+1-n}=w_n.$$

The choice of values symmetric with respect to $\mu=0$ is because, physically, neutrons coming from the right or the left hold equal importance. Furthermore, opting for an even number of directions avoids having $\mu_n=0$, which would eliminate the flux derivative in the equation.
To obtain a good approximation of the integral, the Gauss-Legendre quadrature parameters are introduced (Figure 3.3). The reason why this technique is particularly advantageous for integration is related to the fact that a symmetric interval is involved, i.e. $-1\leq\mu\leq+1$, and to the fact that the integration nodes μ_n, i.e. the points where the function is evaluated (see Eq. (3.46)), are the zeros of the N-th order Legendre polynomial. This is significant because Legendre polynomials are symmetric around zero. Moreover, thanks to this choice, it is possible to integrate polynomials exactly up to a certain order, which is fundamental when approximating complex functions with polynomials.

$\pm\mu_n$	w_n	$\pm\mu_n$	w_n
$N = 2$		$N = 10$	
0.57735 02691	1.00000 00000	0.14887 43389	0.29552 42247
$N = 4$		0.43339 53941	0.26926 67193
0.33998 10435	0.65214 51549	0.67940 95682	0.21908 63625
0.86113 63115	0.34785 48451	0.86506 336663	0.14945 13492
$N = 6$		0.97390 65285	0.06667 13443
0.23861 91860	0.46791 39346	$N = 12$	
0.66120 93864	0.36076 15730	0.12523 34085	0.24914 70458
0.93246 95142	0.17132 44924	0.36783 14989	0.23349 25365
$N = 8$		0.58731 79542	0.20316 74267
0.18343 46424	0.36268 37834	0.76990 26741	0.16007 83286
0.52553 24099	0.31370 66459	0.90411 72563	0.10693 93260
0.79666 64774	0.22238 10344	0.98156 06342	0.04717 53364
0.96028 98564	0.10122 85363		

Figure 3.3: Gauss-Legendre quadrature parameters [1]

With the choice of such quadrature parameters, the boundary conditions for a flat slab immersed in a vacuum with $x \in [0, a]$, can be written as:

$$\Phi(0, \mu_j) = \Phi(a, -\mu_j) = 0 \quad \text{with } j = 1, ..., \frac{N}{2}. \tag{3.48}$$

Proceeding with the resolution of the system of equations 3.47, it can be rewritten by regrouping the term on the right-hand side as:

$$\begin{aligned} &\mu_j \frac{\partial \Phi(x, \mu_j)}{\partial x} + \Sigma_t(x)\Phi(x, \mu_j) = Q(x, \mu_j), \\ &\text{with} \quad Q(x, \mu_j) = \frac{1}{2}(\Sigma_s(x) + \frac{\nu\Sigma_f(x)}{k}) \sum_{n=1}^{N} w_n \Phi(x, \mu_n) + S_{ext}(x, \mu_j), \\ &j = 1..., N. \end{aligned} \tag{3.49}$$

At this point, all that remains is to discretize the spatial variable (see Figure 3.4), which is divided into I intervals, in which the material properties are constant. Therefore, for each equation in the system of Eq. (3.49), there will be a system of equations with I unknowns, consisting of the flux at the center of the interval $\Phi(x_i, \mu_j)$ with $i = 1, ..., I$.

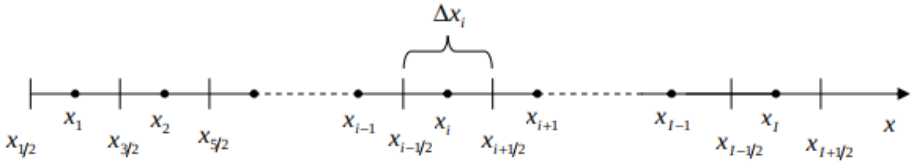

Figure 3.4: Spatial discretization for the discrete ordinates method in the planar case [22]

The system, using the compact subscript notation $(i, j) = (x_i, \mu_j)$, becomes

$$\begin{aligned} &\mu_j \frac{\Phi_{i+1/2,j} - \Phi_{i-1/2,j}}{\Delta x_i} + \Sigma_{ti}\Phi_{i,j} = Q_{i,j}, \\ &i = 1, ..., I \quad j = 1..., N. \end{aligned} \tag{3.50}$$

The choice of replacing the derivative with a finite difference also introduces the fluxes at the nodes of the spatial discretization. To solve this system, the approximation known as the Diamond Rule can be used, which consists of imposing that the flux at the center of the interval is equal to the arithmetic mean of the fluxes at the nodes:

$$\Phi_{i,j} = \frac{\Phi_{i+1/2,j} - \Phi_{i-1/2,j}}{2}.$$

This rule is applied in the numerical implementation for spatial resolution, resulting in two distinct equations depending on whether the equation corresponds to $\mu_j > 0$ or $\mu_j < 0$. Therefore, depending on the value of μ_j, the following applies:

- for $\mu_j > 0$,
  the calculation proceeds from left to right starting from the first node of the first interval, for which $\Phi_{i=1/2,j}$ is known from the boundary condition. Note that the index for the fluxes at the cell center is defined from 1 to I. The Diamond Rule is then rewritten as:
  $$\Phi_{i+1/2,j} = 2\Phi_{i,j} - \Phi_{i-1/2,j}. \tag{3.51}$$
  Eq. (3.51) is then substituted into Eq. (3.50), which, when rearranged, gives us the flux at the cell center:
  $$\Phi_{i,j} = \frac{\Phi_{i-1/2,j} + \dfrac{\Delta x}{2\mu_j} Q_{i,j}}{1 + \dfrac{\Delta x}{2\mu_j}\Sigma_{ti}}. \tag{3.52}$$
  Once the flux at the center of the interval is known, it will be possible to find $\Phi_{i+1/2,j}$, which will then become the starting point for the calculation of the flux for the next interval;

- for $\mu_j < 0$,
  the calculation will be similar to that for the case of $\mu_j > 0$, with the only difference being that this time the calculation starts from the last node of the last interval, which is also known from the boundary condition. The equations that allow the calculation of the flux at the center of the interval will be:
  $$\Phi_{i-1/2,j} = 2\Phi_{i,j} - \Phi_{i+1/2,j}, \tag{3.53}$$

which, when substituted into Eq. (3.50), gives:

$$\Phi_{i,j} = \frac{\frac{\Delta x}{2\mu_j} Q_{i,j} - \Phi_{i+1/2,j}}{\frac{\Delta x}{2\mu_j}\Sigma_{ti} - 1}. \tag{3.54}$$

Similarly, once the flux at the center of the interval is known, it can be substituted into Eq. (3.53) to find the flux at the node, which will be used as the starting point for the subsequent spatial iteration.

The calculation explained previously refers to the direct flux. However, in BISTRO, it is possible to repeat the same calculation for solving the adjoint transport equation (which contains the adjoint operators) in the pseudo-steady-state form. This gives as a solution the neutronic importance function $\Phi^*(\mathbf{r}, E, \hat{\Omega})$ (the adjoint flux), which represents the average asymptotic increase of N_0 (the number of neutrons present in the stationary reactor) for a single neutron inserted at point $\mathbf{r}$, with energy E, and direction $\hat{\mathbf{\Omega}}$.
The procedure to derive the adjoint transport equation (Eq. (3.55)) can be of two types: a mathematical approach, which utilizes the properties of adjoint operators on direct operators, or a physical approach, which derives it through the balance of the importance function and demonstrates that it satisfies the same equation obtained with the analytical approach.

$$\begin{aligned} &-\hat{\Omega}\cdot\nabla\Phi^*(\mathbf{r}, E, \hat{\Omega}) + \Sigma_t(\mathbf{r}, E)\Phi^*(\mathbf{r}, E, \hat{\Omega}) = \\ &\int_0^\infty \mathrm{d}E' \int_{4\pi} \mathrm{d}\hat{\Omega}'\Sigma_s(\mathbf{r}, E \to E', \hat{\Omega} \to \hat{\Omega}')\Phi^*(\mathbf{r}, E', \hat{\Omega}') + \\ &+ \frac{1}{k^*}\frac{\chi(E)}{4\pi}\int_0^\infty \int_{4\pi} \nu(\mathbf{r}, E)\Sigma_f(\mathbf{r}, E)\Phi^*(\mathbf{r}, E', \hat{\Omega}')\mathrm{d}\hat{\Omega}'\mathrm{d}E'. \end{aligned} \tag{3.55}$$

Further observations on $\Phi^*(\mathbf{r}, E, \hat{\Omega})$ are the following [16]:

- this quantity cannot be less than zero, thus the function in question is non-negative;
- given the definition, it is logical that the function must be continuous in $\mathbf{r}$ in every direction;
- the contribution of a neutron located on the boundary of the medium and moving outward must be zero since it escapes and therefore does not contribute. It can be written with $\hat{\mathbf{n}}$ as the normal to the outer surface S, where $(\hat{\mathbf{\Omega}} \cdot \hat{\mathbf{n}}) > 0$:

$$\Phi^*(\mathbf{r}_s, E, \hat{\mathbf{\Omega}}) = 0 \quad \text{for} \quad \mathbf{r}_s \in S \quad \text{and} \quad \hat{\mathbf{\Omega}} \cdot \hat{\mathbf{n}} > 0,$$

which represents the boundary condition for Eq. (3.55).

In the next paragraph, it will be explained how the adjoint flux is used to calculate the relative sensitivity coefficients for k applying the first-order Standard Perturbation Theory.

3.4 The Adjoint Flux and Standard Perturbation Theory for the Calculation of the Sensitivity Coefficient of k

This section briefly introduces the properties of adjoint operators and the application of these properties to the Boltzmann equation for the direct flux and the importance function (adjoint flux). An approximate expression for the relative sensitivity coefficient of k will then be derived using the first-order Standard Perturbation Theory (SPT) under the assumption of small perturbations.

3.4.1 Definition of Adjoint Operators

Given two real functions f and h (i.e. they map real numbers to real numbers) belonging to a set I and defined on a domain D associated with the generic variable (or set of variables) ξ, their inner product is defined by the following operation:

$$\langle f, h \rangle = \int_D f h \, d\xi.$$

Considering now two operators $\mathcal{F}$ and $\mathcal{H}$ defined on the set I, they are said to be adjoint to one another if, for any given pair of functions $(f, h) \in I$ [16], the following holds:

$$\langle f, \mathcal{H}h \rangle = \langle \mathcal{F}f, h \rangle, \tag{3.56}$$

that is

$$\int_D f \, (\mathcal{H}h) \, d\xi = \int_D (\mathcal{F}f) \, h \, d\xi. \tag{3.57}$$

Now, considering the pseudo-stationary Boltzmann equation for the direct flux

$$\begin{aligned} &\hat{\Omega} \cdot \nabla \Phi(\mathbf{r}, E, \hat{\Omega}) + \Sigma_t(\mathbf{r}, E) \Phi(\mathbf{r}, E, \hat{\Omega}) = \\ &\int_0^\infty \int_{4\pi} \Sigma_s(\mathbf{r}, E \to E', \hat{\Omega} \to \hat{\Omega}') \Phi(\mathbf{r}, E', \hat{\Omega}') \, \mathrm{d}\hat{\Omega}' \mathrm{d}E' + \\ &+ \frac{1}{k} \frac{\chi(E)}{4\pi} \int_0^\infty \int_{4\pi} \nu(\mathbf{r}, E) \Sigma_f(\mathbf{r}, E) \Phi(\mathbf{r}, E', \hat{\Omega}') \, \mathrm{d}\hat{\Omega}' \mathrm{d}E', \end{aligned} \tag{3.58}$$

it can be written in terms of operators as follows:

$$B\Phi = \left(A - \frac{F}{k} \right) \Phi = 0. \tag{3.59}$$

where:

- $A = \hat{\Omega} \cdot \nabla \square + \Sigma_t(\mathbf{r}, E)\square - \int_0^\infty \int_{4\pi} \Sigma_s(\mathbf{r}, E \to E', \hat{\Omega} \to \hat{\Omega}')\square \, \mathrm{d}E' \mathrm{d}\hat{\Omega}'$;
- $F = \dfrac{\chi(E)}{4\pi} \int_0^\infty \int_{4\pi} \nu(\mathbf{r}, E)\Sigma_f(\mathbf{r}, E)\square \mathrm{d}\hat{\Omega}' \mathrm{d}E'$.

The same can be done by taking Eq. (3.55) for the importance function:

$$B^*\Phi^* = \left(A^* - \frac{F^*}{k^*}\right)\Phi^* = 0, \tag{3.60}$$

where:

- $A^* = -\hat{\Omega} \cdot \nabla \square + \Sigma_t(\mathbf{r}, E)\square - \int_0^\infty \int_{4\pi} \Sigma_s(\mathbf{r}, E \to E', \hat{\Omega} \to \hat{\Omega}')\square \, \mathrm{d}E' \mathrm{d}\hat{\Omega}'$;
- $F^* = \dfrac{\chi(E)}{4\pi} \int_0^\infty \int_{4\pi} \nu(\mathbf{r}, E)\Sigma_f(\mathbf{r}, E)\square \mathrm{d}\hat{\Omega}' \mathrm{d}E'$;
- $k^* = k$.

It is then proven that the following equality holds (provided that the boundary conditions are the standard ones, i.e. there is no neutron flux entering the reactor from outside, and that neutrons exiting the reactor have no importance [16]):

$$\int_V \int_0^\infty \int_{4\pi} \Phi^* \, B\Phi \, d\hat{\Omega} dE d\mathbf{r} = \int_V \int_0^\infty \int_{4\pi} \Phi \; B^*\Phi^* \, d\hat{\Omega} dE d\mathbf{r}, \tag{3.61}$$

which, by comparison with the definition of adjoint operator expressed by Eq. (3.57), indicates that B^* is the adjoint operator of B (and vice-versa). Therefore, the (angular) neutron importance function Φ^* is also called the adjoint (angular) neutron flux, because the operator applied to it is the adjoint of the pseudo-stationary Boltzmann operator. The same is true for the scalar neutron importance ϕ^*.
The perturbation theory behind sensitivity analyses makes extensive use of the definition of adjoint operators, as discussed below.

3.4.2 The Relative Sensitivity Coefficient

This section aims to determine the coefficient that quantifies the sensitivity of k to variations in an input parameter α, e.g. a small change in a microscopic cross section or an isotopic concentration. The perturbed quantities within the pseudo-stationary Boltzmann operator B reflecting a generic small input perturbation $\delta\alpha$ are:

$$\begin{cases} A \longrightarrow A' = A + \delta A, \\ F \longrightarrow F' = F + \delta F, \\ k \longrightarrow k' = k + \delta k, \end{cases} \tag{3.62}$$

where, generically, $\square'$ is the perturbed value of $\square$, and $\delta\square$ indicates a small variation of $\square$. After the perturbation, the flux Φ, which is the solution of Eq. (3.59), also changes:

$$\Phi \longrightarrow \Phi' = \Phi + \delta\Phi. \tag{3.63}$$

Thus, the perturbed pseudo-stationary Boltzmann equation for the direct flux can be expressed as:

$$B'\Phi' = \left(A' - \frac{F'}{k'}\right)\Phi' = 0. \tag{3.64}$$

where $B' = B + \delta B$. To determine the value of δk, i.e. the effect of $\delta\alpha$ on the quantity of interest k, the starting point is to consider the inner products of the perturbed direct equation with Φ^*, and of the unperturbed adjoint equation with Φ':

$$\langle B^*\Phi^*, \Phi'\rangle = 0, \tag{3.65}$$

$$\langle \Phi^*, B'\Phi'\rangle = 0. \tag{3.66}$$

Subtracting them term by term yields:

$$\langle B^*\Phi^*, \Phi'\rangle - \langle \Phi^*, B'\Phi'\rangle = 0. \tag{3.67}$$

At this point, the goal is to make appear the variations $\delta\square$. Before doing so, the commutation property of adjoint operators (Eq. (3.57)) is utilized, which allows for the following expression to be written:

$$\langle B^*\Phi^*, \Phi\rangle = \langle \Phi^*, B\Phi\rangle.$$

This results in:

$$\langle \Phi^*, B\Phi'\rangle - \langle \Phi^*, B'\Phi'\rangle = 0. \tag{3.68}$$

If B and B' are written in explicit form, then:

$$\left\langle \Phi^*, \left(A - \frac{F}{k}\right)\Phi' \right\rangle - \left\langle \Phi^*, \left(A' - \frac{F'}{k'}\right)\Phi' \right\rangle = 0. \tag{3.69}$$

The terms can be rearranged to give:

$$\langle \Phi^*, \big(\underbrace{A - A'}_{-\delta A}\big)\Phi'\rangle - \langle \Phi^*, \left(\frac{F}{k} - \frac{F'}{k'}\right)\Phi'\rangle = 0. \tag{3.70}$$

Now, if the quantity $\langle \Phi^*, \frac{F}{k'}\Phi'\rangle$ is added and subtracted in the previous equation, manipulating the terms leads to:

$$-\langle \Phi^*, \delta A\Phi'\rangle - \frac{1}{k'}\langle \Phi^*, F\Phi'\rangle - \left(\frac{1}{k} - \frac{1}{k'}\right)\langle \Phi^*, F\Phi'\rangle + \frac{1}{k'}\langle \Phi^*, F'\Phi'\rangle = 0. \tag{3.71}$$

From the second and fourth terms:

$$\frac{1}{k'}\langle\Phi^*, \delta F\Phi'\rangle = \frac{1}{k'}\langle\Phi^*, F'\Phi'\rangle - \frac{1}{k'}\langle\Phi^*, F\Phi'\rangle. \tag{3.72}$$

In relation to the term $-\big(\frac{1}{k} - \frac{1}{k'}\big)\langle\Phi^*, F\Phi'\rangle$, the goal is to express δk by utilizing the assumption of small perturbations. Since $\delta k = k' - k$, it can be assumed that $k' \simeq k$, thus the term becomes:

$$-\left(\frac{1}{k} - \frac{1}{k'}\right)\langle\Phi^*, F\Phi'\rangle = -\frac{k'-k}{kk'}\langle\Phi^*, F\Phi'\rangle = -\frac{\delta k}{k'k}\langle\Phi^*, F\Phi'\rangle \simeq -\frac{\delta k}{k^2}\langle\Phi^*, F\Phi'\rangle. \tag{3.73}$$

At this point, substituting the results obtained from Eq. (3.72) and Eq. (3.73) into Eq. (3.71) yields

$$-\langle\Phi^*, \delta A\Phi'\rangle + \frac{1}{k'}\langle\Phi^*, \delta F\Phi'\rangle \simeq \frac{\delta k}{k^2}\langle\Phi^*, F\Phi'\rangle. \tag{3.74}$$

The quantity $\delta k/k^2$ can be expressed by rearranging the previous equation and using $k' \simeq k$ as:

$$\frac{\delta k}{k^2} \simeq \frac{-\langle\Phi^*, \delta A\Phi'\rangle + \frac{1}{k}\langle\Phi^*, \delta F\Phi'\rangle}{\langle\Phi^*, F\Phi'\rangle}. \tag{3.75}$$

At this point, if the perturbed flux is written as $\Phi' = \Phi + \delta\Phi$, higher-order terms in δ appear. These terms can be neglected due to the small perturbation assumption made earlier (neglecting these terms is what makes it a first-order approach). This leads to:

$$\begin{aligned} \delta A\Phi' &= \delta A(\Phi + \delta\Phi) = \delta A\Phi + \underbrace{\delta A\delta\Phi}_{\simeq 0} \simeq \delta A\Phi, \\ \delta F\Phi' &= \delta F(\Phi + \delta\Phi) = \delta F\Phi + \underbrace{\delta F\delta\Phi}_{\simeq 0} \simeq \delta F\Phi. \end{aligned} \tag{3.76}$$

Thus, Eq. (3.75) becomes:

$$\frac{\delta k}{k^2} \simeq \frac{-\langle\Phi^*, \delta A\Phi\rangle + \frac{1}{k}\langle\Phi^*, \delta F\Phi\rangle}{\langle\Phi^*, F\Phi'\rangle}, \tag{3.77}$$

Using the assumption $\Phi' \simeq \Phi$ and combining the terms, the equation can be rewritten in a more elegant form:

$$\frac{\delta k}{k} \simeq -k\frac{\langle\Phi^*, \big(\delta A - \frac{\delta F}{k}\big)\Phi\rangle}{\langle\Phi^*, F\Phi\rangle} \tag{3.78}$$

Eq. (3.78) shows the relative variation of k due to a perturbation on the Boltzmann operator. The adjoint flux acts as a weighting function, and both it and the direct flux

appear as unperturbed quantities: they can be computed once and for all, independently of any perturbation, andused for estimating the propagation of perturbations from input data to k.
Starting from this formula, the relative sensitivity coefficient $S(k,\alpha)$ of k with respect to an input parameter α can be defined:

$$S(k,\alpha) = \frac{\delta k}{k} \Big/ \frac{\delta \alpha}{\alpha} = \frac{\alpha}{k}\frac{\partial k}{\partial \alpha} \simeq -k \frac{\langle \Phi^*, \big(\alpha \frac{\partial A}{\partial \alpha} - \frac{\alpha}{k}\frac{\partial F}{\partial \alpha}\big)\Phi \rangle}{\langle \Phi^*, F\Phi \rangle}, \tag{3.79}$$

or, equivalently,

$$S(k,\alpha) = -k \frac{\langle \Phi^*, \alpha \frac{\partial B}{\partial \alpha}\Phi \rangle}{\langle \Phi^*, F\Phi \rangle}. \tag{3.80}$$

In practice, the sensitivity coefficient acts as a factor of amplification or reduction between the relative input variation $\delta\alpha/\alpha$ and the associated output one $\delta k/k$. In practice, it indicates that the relative variation of k due to a change in an input parameter α (e.g., the concentration or microscopic cross section of an isotope) is given by:

$$\frac{\delta k}{k} = S(k,\alpha)\frac{\delta \alpha}{\alpha}. \tag{3.81}$$

In summary, the adjoint flux is used to determine the sensitivity coefficient of the multiplication factor k, for which, thanks to the SPT theory with first-order approximation, it is not necessary to involve perturbed quantities. Moreover, the components of the Boltzmann operator are linear in the microscopic cross sections and in the isotopic concentrations, making the term $\alpha\dfrac{\partial B}{\partial \alpha}$ easy to compute.
It should be noted that the presence of multiple materials (multiple cross sections) implies that, within ERANOS, α assumes more than one value during a single computation, leading to multiple corresponding $S(k,\alpha)$, which results in a vector $\bar{S}$ (or set) of sensitivity coefficients. This vector is then used in combination with input data uncertainties to compute output uncertainties on k through an uncertainty analysis.

3.5 Uncertainty Analysis in ERANOS

Nuclear data found in libraries are associated with uncertainties. These uncertainties are calculated based on how errors propagate during the phases leading to the production of the nuclear data (i.e., errors made during experimental measurements, errors in the evaluation phases associated with the nuclear models used, etc.).
Typically, uncertainties in cross sections are correlated and are not independent from one another. In particular, correlations may occur between:

- the energy ranges of a given cross section;
- the different cross sections of a given isotope;
- the cross sections of different isotopes.

Correlations are contained in the so-called dispersion matrix which is a square, symmetric, positive-definite matrix that includes variance and covariance data related to the multigroup nuclear data used by the code. In ERANOS, three methods are implemented for constructing the dispersion matrix. The method used in this thesis employs the sub-directive AMERE_FILE. The format of the file to be provided with the AMERE_FILE sub-directive contains multiple blocks, with each block relating to the dispersion data between, for instance, reaction $\mathtt{R}_1$ of nuclide $\mathtt{N}_1$ and reaction $\mathtt{R}_2$ of nuclide $\mathtt{N}_2$, formatted as follows [6]:

- a line containing the names of the reactions and nuclides involved: $\mathtt{R}_1$, $\mathtt{N}_1$, $\mathtt{R}_2$, $\mathtt{N}_2$;
- a line containing the G values ($g = 1, ..., G$) of the standard deviations for reaction $\mathtt{R}_1$ on nuclide $\mathtt{N}_1$;
- a line containing the G values ($g = 1, ..., G$) of the standard deviations for reaction $\mathtt{R}_2$ on nuclide $\mathtt{N}_2$;
- a $G \times G$ table T (with the first index being the line index, the second index being column index, while g, g_1, and g_2 are the group indices ranging between 1 and G), which involves $\mathtt{R}_1$, $\mathtt{N}_1$, $\mathtt{R}_2$, and $\mathtt{N}_2$ according to the following:
  - if $\mathtt{R}_1 = \mathtt{R}_2 = \mathtt{R}$ and $\mathtt{N}_1 = \mathtt{N}_2 = \mathtt{N}$, then $T(g, g) = 1$, and for $g_1 \neq g_2$, $T(g_1, g_2) = T(g_2, g_1)$ represents the correlation between group g_1 and group g_2 for reaction $\mathtt{R}$ of nuclide $\mathtt{N}$;
  - if $\mathtt{R}_1 \neq \mathtt{R}_2$ or $\mathtt{N}_1 \neq \mathtt{N}_2$, then $T(g_1, g_2)$ represents the correlation between reaction $\mathtt{R}_1$ of nuclide $\mathtt{N}_1$ in group g_2 and reaction $\mathtt{R}_2$ of nuclide $\mathtt{N}_2$ in group g_1 (note the order of the group indices!).

An example is shown in Figure 3.5, where two blocks of reactions and nuclides are involved and only 3 energy groups are considered ($g = 1, 2, 3$), and thus T is a 3×3 table:

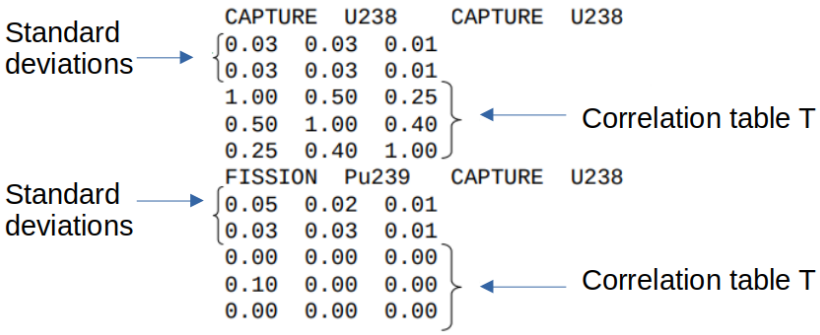

Figure 3.5: Example of the format of the file to be provided with the AMERE_FILE sub-directive for defining the dispersion matrix.

In summary, the file used with the AMERE_FILE sub-directive contains two things. The first one corresponds to the values of the standard deviations

$$\boldsymbol{\sigma}_{\mathtt{X}} = \sqrt{\mathbb{E}\left[(\mathtt{X} - \mathbb{E}[\mathtt{X}])^2\right]}, \tag{3.82}$$

where:

- $\mathtt{X}$ is the generic input quantity of interest (e.g. the microscopic cross section for a given triad isotope, reaction, and energy group);
- $\mathbb{E}[\mathtt{X}]$ is the expected value of $\mathtt{X}$;
- $\mathbb{E}\left[(\mathtt{X} - \mathbb{E}[\mathtt{X}])^2\right]$ is the expected value of the square of the difference between $\mathtt{X}$ and its expected value, i.e. it is the variance $\boldsymbol{\sigma}^2_{\mathtt{X}}$.

The second thing corresponds to a matrix of correlations (dispersion matrix), whose generic element is

$$\rho_{\mathtt{X}_1\mathtt{X}_2} = \frac{\mathrm{Cov}(\mathtt{X}_1, \mathtt{X}_2)}{\boldsymbol{\sigma}_{\mathtt{X}_1}\boldsymbol{\sigma}_{\mathtt{X}_2}} \quad -1 \leq \rho_{\mathtt{X}_1\mathtt{X}_2} \leq 1, \tag{3.83}$$

where $\mathrm{Cov}(\mathtt{X}_1, \mathtt{X}_2)$ is the covariance between $\mathtt{X}_1$ and $\mathtt{X}_2$ given by

$$\mathrm{Cov}(\mathtt{X}_1, \mathtt{X}_2) = \mathbb{E}\left[(\mathtt{X}_1 - \mathbb{E}[\mathtt{X}_1])(\mathtt{X}_2 - \mathbb{E}[\mathtt{X}_2])\right] = (\boldsymbol{\sigma}_{\mathtt{X}_1}\boldsymbol{\sigma}_{\mathtt{X}_2})\rho_{\mathtt{X}_1\mathtt{X}_2}. \tag{3.84}$$

More precisely, if $\mathbf{D}$ is the dispersion matrix, then its element D_{ij}, which is indexed by composite indices $i = (r, g, n)$ and $j = (r', g', n')$, where r, r' are the reaction indices, g, g' are the group indices, and n, n' are the nuclide indices, is given by:

- D_{ii} (on the main diagonal, where $i = j$), i.e. variance of the cross section of index i, as the covariance coincides with the variance if $\mathtt{X}_1 = \mathtt{X}_2$ (Eq 3.84);

- D_{ij} (outside the main diagonal, where $i \neq j$), i.e. the covariance between cross sections of composite indices i and j.

Once the dispersion matrix has been obtained, the square of the uncertainty ε is calculated using the well-known sandwich formula [6]:

$$\varepsilon^2 = \bar{S}^T \mathbf{D} \bar{S} = \sum_{n,r,g,n',r',g'} S_{n,r,g} D_{n,r,g;n',r',g'} S_{n',r',g'}, \tag{3.85}$$

where:

- $S_{n,r,g}$ is the sensitivity coefficient (belonging to the sensitivity column vector $\bar{S}$) of a given fixed output quantity $\mathcal{Q}$ (e.g. k) with respect to the microscopic cross section of nuclide n for reaction r and group g:

$$S_{n,r,g} = S(\mathcal{Q}, \sigma_{n,r,g}) = \frac{\delta \mathcal{Q}}{\mathcal{Q}} \Big/ \frac{\delta \sigma_{n,r,g}}{\sigma_{n,r,g}}; \tag{3.86}$$

- $\bar{S}^T$ is the transpose of $\bar{S}$.

Specifically, in ERANOS, the module that calculates the uncertainty [6] provides three tables containing the square root of each partial sum:

- the sum over the energy groups, which is presented as a table (nuclides against reactions), where the generic term is

$$\varepsilon_g(n,r) = \sqrt{\sum_{g,g',n',r'} S_{n,r,g} D_{n,r,g;n',r',g'} S_{n',r',g'}}; \tag{3.87}$$

- the sum over the nuclides, which is presented as a table (groups against reactions), where the generic term is

$$\varepsilon_n(g,r) = \sqrt{\sum_{n,n',r',g'} S_{n,r,g} D_{n,r,g;n',r',g'} S_{n',r',g'}}; \tag{3.88}$$

- the sum over the reactions, which is presented as a table (groups against nuclides), where the generic term is

$$\varepsilon_r(g,n) = \sqrt{\sum_{r,r',n',g'} S_{n,r,g} D_{n,r,g;n',r',g'} S_{n',r',g'}}. \tag{3.89}$$

Each of these tables also presents the total value, which corresponds to the result of Eq. (3.85):

$$\sum_{n,r} \varepsilon_g^2(n,r) = \sum_{g,r} \varepsilon_n^2(g,r) = \sum_{g,n} \varepsilon_r^2(g,n) = \varepsilon^2. \tag{3.90}$$

Chapter 4

ALFRED's benchmark

This chapter introduces the ALFRED benchmark cases and presents the results obtained from this work. For each case, the modeling process using ECCO and ERANOS is described, followed by an analysis of the corresponding results.

4.1 Introduction to the Benchmark

The ALFRED benchmark is organized into three phases, with the second phase further divided into three sub-cases. The structure is:

- Phase 1: fuel pin elementary cell;
- Phase 2: cells and super-cells:
  - 2.1: fuel assembly,
  - 2.2: absorber super-cell,
  - 2.3: shield super-cell;
- Phase 3: full core (not taken into account for this work).

Each case was solved using ECCO for cell calculations and ERANOS for uncertainty and sensitivity analysis. The ENDF/B-VIII.0 nuclear data set was used as reference library. In ECCO, materials were defined based on either their complete elementary and isotopic composition (providing weight or volume percentages on the whole) or their chemical composition (thus only providing the isotopy of elements combined by their stoichiometry). As per benchmark's specifications, the density for all materials was set at 20°C, consistent with cold model, except for lead, which was assigned a density of 10502.9 kg/m^3, corresponding to the average coolant temperature in the core. Subsequently, media were defined by combining these materials and specifying their volume fraction.

Cells were then defined by arranging the various media in a 2-D geometry and specifying the required boundary conditions for the benchmark.
Once the cell was characterized, it was possible to perform the calculation scheme deputed to homogenization and condensation of cross sections, which were then transferred to the reactor portion of ERANOS for post-processing and/or their use in flux calculations necessary to perform sensitivity and uncertainty analyses. The data post-processing was automated in ERANOS by creating custom files using LU (*Langage Utilisateur*) functions. This approach was implemented to minimize reading errors, ensuring streamlined post-processing for all cases.

4.2 PHASE 1: fuel pin elementary cell simulations

Phase 1 focuses on the study of the bi-dimensional heterogeneous model of the fuel pin elementary cell. It was modeled considering a typical ALFRED inner fuel pin (see Section 2.2), surrounded by lead corresponding to the coolant fraction assigned to that pin (see Figure 4.1). The cell was considered to be immersed in an infinite lattice of identical cells with the axial dimension assumed infinite by reflection boundary conditions.

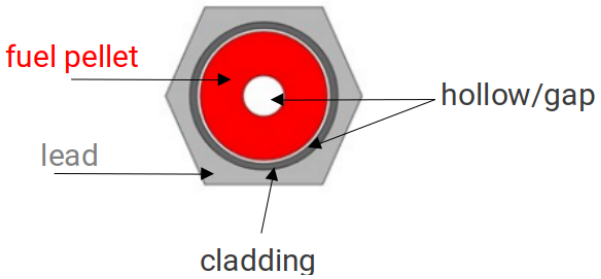

Figure 4.1: Fuel pin cell model.

The benchmark requires to find the following quantities:

- the infinite multiplication factor k_∞;
- the fission and capture microscopic 1-group cross sections for ^{239}Pu, ^{241}Pu, ^{235}U, and ^{238}U, together with their average number of neutrons emitted per fission event ν;
- the 1-group inelastic scattering microscopic cross section for ^{238}U and ^{208}Pb;
- the 1-group capture microscopic cross sections for ^{56}Fe and ^{208}Pb;
- the 172-group neutron spectrum;

- the reproduction factor $\eta = \dfrac{\nu\Sigma_f}{\Sigma_{a,fuel}}$;
- the utilization factor $f = \dfrac{\Sigma_{a,fuel}}{\Sigma_{a,tot}}$;
- the transport cross section $\Sigma_{tr} = \Sigma_t - \mu_0\Sigma_s$;
- the five isotope and reaction combinations that give the highest k_∞ sensitivity coefficients and uncertainties.

Furthermore, the benchmark requires finding the buckling B^2 that makes the cell critical. For comparison purposes only, the calculations for the infinite configuration (buckling is zero) were repeated also for the critical configuration (in which the buckling is greater than zero, but the radially infinite condition is retained), sensitivity and uncertainty analyses excluded.

4.2.1 Phase 1 Execution

The Phase 1 case was treated using the ECCO cell code, within which the materials 'lead', 'AIM1' (stainless steel), 'UO_2' (uranium dioxide), and 'PuO_2' (plutonium dioxide) were implemented. Subsequently, the media 'lead' and 'AIM1' were defined by simply associating a 100% volume fraction of the respective materials. For the definition of the MOX fuel medium, the uranium dioxide and plutonium dioxide materials were used with the volume fraction given by the enrichment of the inner-type fuel. Furthermore, to speed up the computation time, the cell geometry was simplified by removing the hollow and the gap, which were combined into a single homogeneous region proceeding with a dilution of the volume fraction (density) of the materials within the MOX (see Figure 4.2).

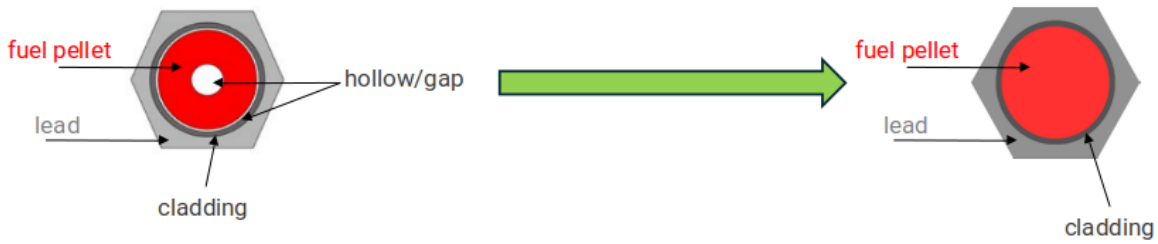

Figure 4.2: Simplified Fuel pin cell model.

After implementing the materials, the geometry was defined on ECCO as in Listing 4.1.

```
1  CELL    'PIN_CELL'
2    COMPOSITION_ORDER 'lead_med' 'AIM1_med' 'MOX_med'
3    GEOMETRY DATA
4      HEXAGON 1 (PIN_PITCH)
5       CYLINDRICAL 2
6       (R_EXT_FUEL)    REGION 1  'fuel' COMP 3   (TEMP_CELSIUS+273.15)
7       (R_EXT_CLAD)    REGION 2  'clad' COMP 2   (TEMP_CELSIUS+273.15)
8       IN
9       REGION  3  'lead' COMP 1   (TEMP_CELSIUS+273.15)
10     REFLECT
11   END OF GEOMETRY DATA
12 ;
```

Listing 4.1: Geometry of the pin cell for benchmark Phase 1.

As it can be seen from line 10 of Listing 4.1, the reflection boundary condition was applied to the outer face of the hexagon. This condition was necessary to recreate the infinite lattice required by the benchmark. As required by ECCO, the geometry was defined from the outside inwards, with the gaps between the various geometric boundaries representing the regions. The media were assigned to each region using the `COMP` keyword followed by the number with which the medium appears in the `COMPOSITION_ORDER` list. After defining the geometry, the cell calculation routine was executed, with the following inputs: the cell name (line 1 of the listing), the cross section library (see Section 4.1), and the temperatures in Kelvin associated with each region. These temperatures differ from those used for material definition in the cold model because they are specifically used for modeling the Doppler effect (i.e., the broadening of the resonance absorption cross sections due to temperature rising).
As mentioned earlier, the Phase 1 calculations were performed for this work both considering an infinite configuration (following the benchmark requirements) and a critical one (not required). In ECCO, the cell can be characterized to assume an infinite or a critical configuration through the buckling. In particular, an infinite cell (both radially, as a consequence of the boundary conditions, and axially) is obtained by imposing $B^2 = 0$, while a critical configuration (only radially infinite) requires to perform buckling searches, i.e., the code iteratively finds the buckling that gives a given multiplication factor provided by the user (typically, 1). Performing calculations in ECCO involves a series of steps aimed at homogenizing the cross sections in space and condensing them into the energy groups required by the user.

Description of the calculation algorithms

In the first step, the cell is homogenized, and using the 172-group cross section library, the fluxes are found by imposing or searching the buckling, depending on the desired cell configuration (infinite or critical, respectively). In the second step, the calculation is carried out in original geometry (i.e., heterogeneous) starting from the buckling of the previous step and keeping the same number of energy groups. In the third step, the

calculation is repeated exploding the energy description to the 1968-group (fine) structure library (fine groups) For the main isotopes, a standard library is used, while for the remaining ones the 172 structure is deconvoluted to 1968 groups. Then the cross sections are condensed to the number of groups **n** chosen as indicated in the benchmark. In the fourth step, the calculation is carried out in the original geometry with the condensed groups and the buckling is updated (in the infinite configuration, this does not change the buckling). In the last step, the buckling is taken from the previous step and the homogenization of the cell -hence of the cross sections- is performed. The newly condensed and homogenized cross sections are saved and sent to ERANOS. From now onwards, the scheme for the critical cell (schematized in Figure 4.3) will be called "Critical" while the scheme for the infinite cell (schematized in Figure 4.4) will be called "Axially Infinite", to emphasize that both cells have the radial reflection condition and are therefore limitless in that direction.

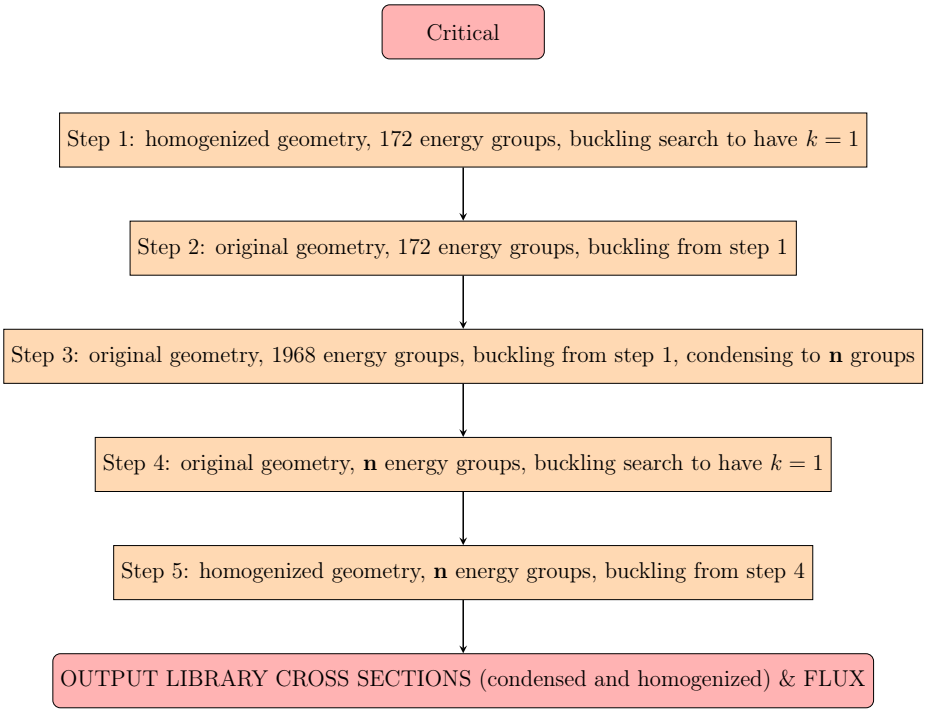

Figure 4.3: Block diagram of the ECCO steps for the critical cell (condensation to **n** groups).

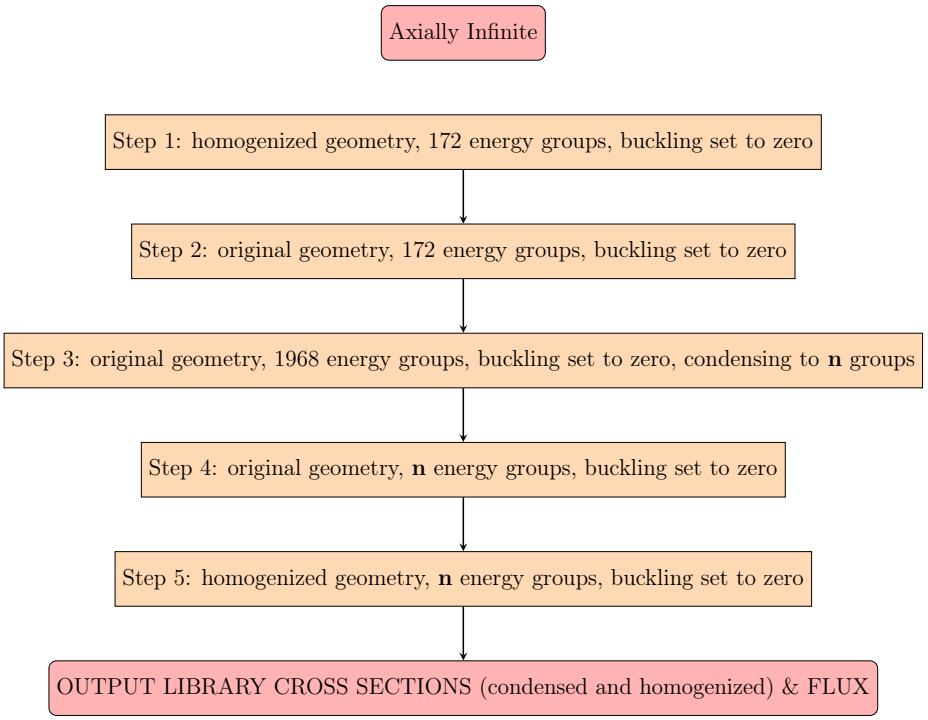

Figure 4.4: Block diagram of the ECCO steps for the infinite cell (condensation to **n** groups).

4.2.2 Phase 1 Results

This subsection presents the results for both the Critical and Axially Infinite calculations, which are then compared. Sensitivity and uncertainty analyses are excluded from the comparison as they are performed only for the Axially Infinite calculations.

172-group neutron spectum

The neutron spectrum at 172 groups has been calculated using the previously mentioned routines with **n=172**. Figure 4.5 shows, for both cell configurations, the neutron spectrum normalized with respect to the total flux as:

$$\phi_i^{\text{norm}} = \frac{\phi_i}{\sum_{j=1}^{172} \phi_j}, \tag{4.1}$$

where:

- ϕ_i^{norm} is the normalized flux of the i-th group,
- ϕ_i is the flux of the i-th group,
- $\sum_{j=1}^{172} \phi_j$ is the total flux, which is the sum of the fluxes of the 172 groups.

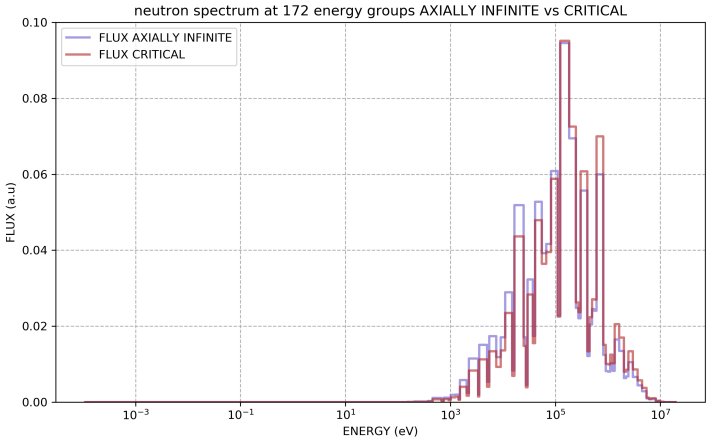

Figure 4.5: Neutron spectrum at 172 groups normalized on the total flux: critical case (red) vs axially infinite case (blue).

From Figure 4.5, it can be observed that the flux calculated for the critical cell is harder compared to that calculated for the infinite one. This behavior is justified by the fact that in an infinite cell, neutrons undergo more collisions since they cannot escape from it, thus losing more energy. This observation is also confirmed by the cross sections shown in Table 4.1.
In addition to the normalization over the total flux, a weighted normalization over the energy range of each group was also done to better observe the distribution that flux takes over the various energy groups. The same was repeated using lethargy widths in place of the energy ones.
The flux of the i-th group is normalized in energy as a weighted average of the flux ϕ_i by the energy group width ΔE_i of the i-th group using the following equation:

$$\phi_i^{\text{norm}} = \frac{\phi_i \cdot \Delta E_i}{\sum_{j=1}^{172} \phi_j \cdot \Delta E_j}, \tag{4.2}$$

where:

- ΔE_i is the energy group width of the i-th group;
- $\sum_{j=1}^{172} \phi_j \cdot \Delta E_j$ is the total flux weighted by the energy group widths of the 172 groups.

The flux of the i-th group is normalized in lethargy $u(E) = \ln \frac{E_0}{E}$ (E_0 is an arbitrary reference neutron energy), where the flux ϕ_i is weighted by the lethargy width $\Delta u_i =$

$\ln \frac{E_i}{E_{i+1}} = u(E_{i+1}) - u(E_i)$ associated with the i-th group using the following equation:

$$\phi_i^{\text{norm}} = \frac{\phi_i \cdot \Delta u_i}{\sum_{j=1}^{172} \phi_j \cdot \Delta u_j} \tag{4.3}$$

As observed in Figures 4.6 and 4.7, the harder nature of the neutron spectrum in the critical case is even more evident when normalized in energy and lethargy, as hinted by the vertical axis scale.

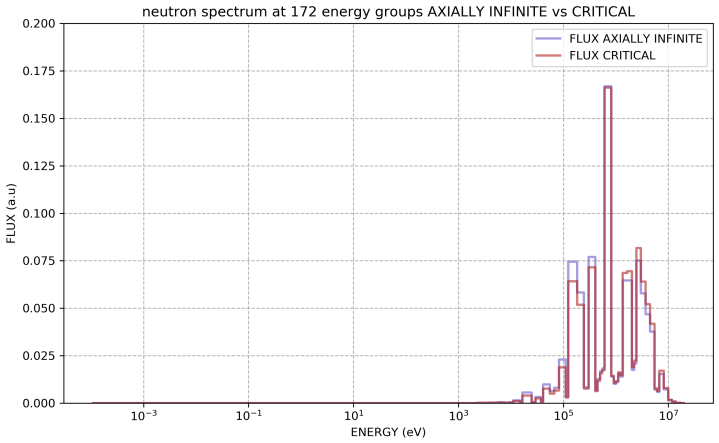

Figure 4.6: Neutron spectrum at 172 groups normalized on energy: critical case (red) vs axially infinite case (blue).

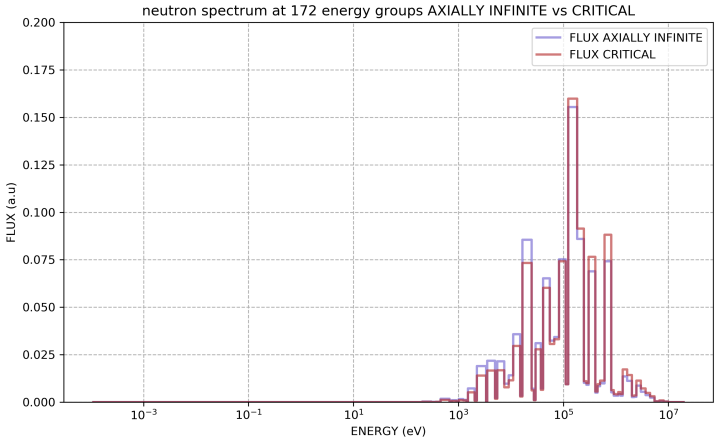

Figure 4.7: Neutron spectrum at 172 groups normalized on lethargy: critical case (red) vs axially infinite case (blue).

1-group microscopic quantities

For this part of Phase 1, the calculation schemes were used with **n=1**. As can be deduced from Table 4.1, the microscopic fission cross section for fissile isotopes is higher for the infinite cell case than the critical one, the opposite happens for fissionable isotopes; this is consistent with what was found for the 172 group neutron spectrum. In fact, for a fissile isotope, the microscopic fission cross section increases as the energy of the incident neutron decreases, whereas, for fissionable ones, the opposite is true because of the fission threshold energy (see Figure 4.8). This is confirmed by the values found, as the ^{238}U fission cross section is higher for the critical case, where the spectrum is harder. Another parameter that confirms what has been discussed so far is ν, a number that increases with the energy of the neutrons for both fissile and fissionable isotopes (see Figure 4.9). What has been observed for the microscopic cross sections will also influence the macroscopic ones and the criticality factors.

Isotope	Quantity	Axially Infinite configuration	Critical configuration	Unit
^{239}Pu	σ_c	4.46348×10^{-1}	3.73400×10^{-1}	b
^{239}Pu	σ_f	1.72480	1.69814	b
^{239}Pu	ν	2.93925	2.95080	#
^{241}Pu	σ_c	4.05293×10^{-1}	3.55038×10^{-1}	b
^{241}Pu	σ_f	2.39221	2.24477	b
^{241}Pu	ν	2.96546	2.97244	#
^{235}U	σ_c	5.10091×10^{-1}	4.46780×10^{-1}	b
^{235}U	σ_f	1.82902	1.70896	b
^{235}U	ν	2.45511	2.46391	#
^{238}U	σ_c	2.70765×10^{-1}	2.39577×10^{-1}	b
^{238}U	σ_f	3.66421×10^{-2}	4.66242×10^{-2}	b
^{238}U	ν	2.72276	2.72579	#
^{56}Fe	σ_c	8.17717×10^{-3}	7.49093×10^{-3}	b
^{208}Pb	σ_c	6.74317×10^{-4}	7.27047×10^{-4}	b
^{208}Pb	σ_{in}	2.59467×10^{-2}	3.37407×10^{-2}	b

Table 4.1: 1-group microscopic cross sections σ and the average number of neutrons emitted per fission event ν for Phase 1. The values are presented for both the axially infinite and critical configurations. The subscripts c, f, and in represent the capture, fission, and inelastic reactions respectively.

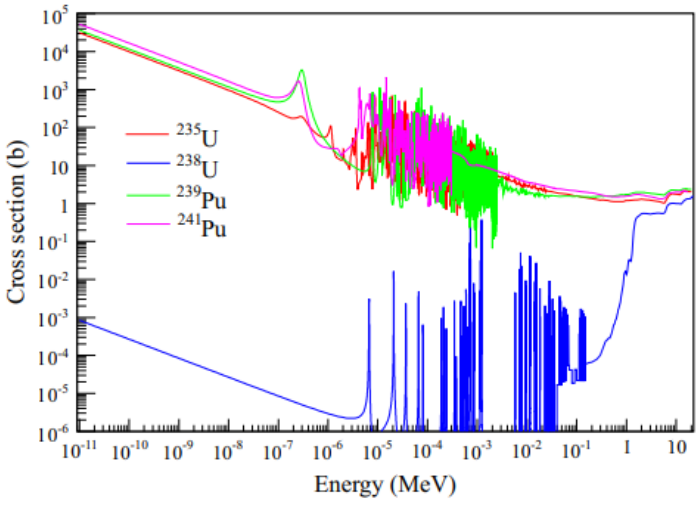

Figure 4.8: Microscopic fission cross sections of ^{235}U, ^{238}U, ^{239}Pu, and ^{241}Pu in barn [11].

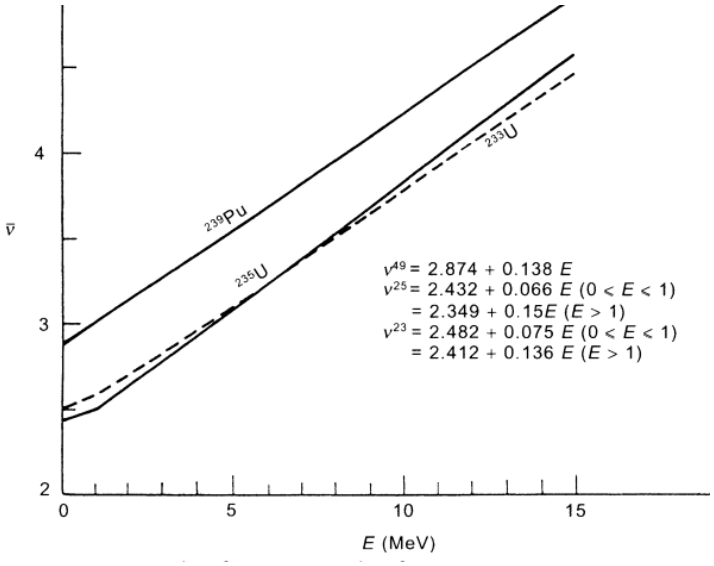

Figure 4.9: The average number of neutrons emitted per fission ν for ^{239}Pu, ^{235}U and ^{233}U [8].

1-group macroscopic cross sections and integral parameters

In Table 4.2, the parameters that are input data for the calculation schemes (see Figures 4.4 and 4.3) are highlighted in red. Actually, while B^2 can be set to 0, $k = 1$ is only a consequence of a buckling search. Therefore, the value of k corresponding to the buckling search can be 1, very close to 1, or far from it, depending on the effectiveness of the iterative search method, which can be influenced by aspects such as the cell complexity. Comparing the results for the two configurations, the most striking one is Σ_f, which is larger in the critical case. This occurs even though the microscopic fission cross sections for fissile isotopes are larger in the infinite cell case, and those for fissionable isotopes are two orders of magnitude smaller in both case. To understand this, it is necessary to highlight that both cases have the same concentration, and what influences the macroscopic fission cross section is the product between concentrations and microscopic cross sections of the various isotopes, as it is shown in the following equation:

$$\Sigma_f(E) = \sum_{i=1}^{\mathcal{N}_i} N_i \sigma_{f,i}(E) \tag{4.4}$$

where:

- $\Sigma_f(E)$ is the macroscopic fission cross section,
- N_i is the concentration of the i-th isotope,

- $\sigma_{f,i}(E)$ is the microscopic fission cross section of the i-th isotope,
- $\mathcal{N}_i$ is the total number of isotopes considered.

It is then understood how, within the critical case (harder spectrum), the fissionable component plays a fundamental role in the balance for the calculation of Σ_f. Indeed, although both cases have the same concentrations and the microscopic cross sections of fissile isotopes seem to favor the infinite case, in reality, the higher concentration of fissionable material in the fuel (only 20% enrichment) is predominant, in particular thanks to ^{238}U.

Quantity	**Axially Infinite configuration**	**Critical configuration**	**Unit**
k	1.35207	1.00000	#
B^2	0.0000	1.86698×10^{-3}	cm^{-2}
Σ_a	5.47884×10^{-3}	5.19005×10^{-3}	cm^{-1}
$\Sigma_{\mathrm{a,fuel}}$	5.26678×10^{-3}	4.99338×10^{-3}	cm^{-1}
$\nu\Sigma_f$	7.38894×10^{-3}	7.59000×10^{-3}	cm^{-1}
Σ_f	2.52561×10^{-3}	2.58861×10^{-3}	cm^{-1}
Σ_{tr}	2.70825×10^{-1}	2.57346×10^{-1}	cm^{-1}
η	1.40293	1.52001	#
f	9.61294×10^{-1}	9.62107×10^{-1}	#

Table 4.2: 1-group output quantities for Phase 1: multiplication factor k, buckling B^2, main macroscopic cross sections, reproduction factor η, and utilization factor f. The values are presented both for axially infinite and critical configurations.

Another aspect evidenced by the table is a lower Σ_{tr} in the critical case than the infinite one, which translates into a higher diffusion coefficient $D = \dfrac{1}{3\Sigma_{tr}}$. This result still confirms the presence of a harder spectrum compared to the infinite case.

Uncertainty and sensitivity analysis for the axially infinite configuration

The uncertainty and sensitivity analyses were carried out using BISTRO (see Sections 3.4 and 3.5), with the cross sections provided by ECCO. The cross sections were calculated using the Axially Infinite routine, in which they were condensed to 33 groups (**n=33**), although the results for each isotope are the sum of the groups (see Eq. (3.87)). The benchmark does not provide any information about the number of groups for performing sensitivity and uncertainty analyses. Therefore, the choice of using 33 groups was related to multiple reasons:

- it is a standard discretization adopted for fast reactors;

- ENEA has access to 33-group nuclear data variances and correlations for uncertainty calculations;
- it is a good trade-off between precision, physics, and computational time (when compared to the 1-group and the 172-group discretizations).

This discretization allowed for a sufficiently accurate calculation of the direct flux and the adjoint flux (importance function), which in turn were used to calculate the sensitivity coefficients for k.
Table 4.3 shows the five most relevant combinations of isotopes and reactions in terms of k sensitivity, regardless of the sign. This ranking was made on the isotopes involved in the previous benchmark requests.

$\boldsymbol{\alpha}$	$\mathbf{S}(\mathbf{k}, \boldsymbol{\alpha})$
$\sigma_f^{^{239}\mathrm{Pu}}$	4.549614×10^{-1}
$\sigma_c^{^{238}\mathrm{U}}$	-2.244481×10^{-1}
$\sigma_{in}^{^{238}\mathrm{U}}$	-7.289689×10^{-2}
$\sigma_f^{^{241}\mathrm{Pu}}$	6.995399×10^{-2}
$\sigma_c^{^{239}\mathrm{Pu}}$	-5.146001×10^{-2}

Table 4.3: Most relevant sensitivity coefficients $S(k, \alpha)$ of the multiplication factor k to the cross sections as input data α for Phase 1.

Naturally, the infinite multiplication factor is most sensitive to the fission of ^{239}Pu, as it is the primary fissile isotope in MOX fuel. In general, the high relevance of ^{239}Pu fission for nuclear reactors is associated with particularly low uncertainties regarding its cross section data in libraries. Therefore, it was expected that the output uncertainties on k originated from the ^{239}Pu fission were relatively low, even in presence of high sensitivities. However, the uncertainty in the fission reaction turns out to be the highest among those calculated (see Table 4.4). Despite this, when considering the order of magnitude, it is practically the same as the other reactions in the top five and is twice as small as the sensitivity coefficient.

$\boldsymbol{\alpha}$	$\boldsymbol{\varepsilon(k, \alpha)}$
$\sigma_f^{^{239}\mathrm{Pu}}$	5.41360×10^{-3}
$\sigma_c^{^{238}\mathrm{U}}$	3.39680×10^{-3}
$\sigma_{in}^{^{238}\mathrm{U}}$	3.32530×10^{-3}
$\sigma_c^{^{239}\mathrm{Pu}}$	3.01970×10^{-3}
$\sigma_{in}^{^{239}\mathrm{Pu}}$	1.61000×10^{-3}

Table 4.4: Most relevant uncertainties $\varepsilon(k, \alpha)$ of the multiplication factor k to the cross sections as input data α for Phase 1.

The sensitivity and uncertainty analysis with $\alpha = \nu$ for k are shown in Table 4.5 considering the main fissile and fissionable isotopes. The results underline the relevance of ^{239}Pu on the infinite multiplication factor and they highlight how ^{238}U contributes more than ^{235}U, confirming what was said for the macroscopic fission cross sections and η.

$\boldsymbol{\alpha}$	$\boldsymbol{S(k,\alpha)}$	$\boldsymbol{\varepsilon(k,\alpha)}$
$\nu^{^{235}\mathrm{U}}$	8.593767×10^{-3}	4.45340×10^{-5}
$\nu^{^{238}\mathrm{U}}$	9.415277×10^{-2}	1.17110×10^{-3}
$\nu^{^{239}\mathrm{Pu}}$	6.904930×10^{-1}	1.88950×10^{-3}
$\nu^{^{241}\mathrm{Pu}}$	1.028110×10^{-1}	2.54970×10^{-4}

Table 4.5: Values of sensitivity coefficients $S(k,\alpha)$ and the uncertainty $\varepsilon(k,\alpha)$ of the multiplication factor k to ν for fissile and fissionable isotopes in Phase 1.

4.2.3 Further Considerations on Phase 1

The results reported so far were obtained using the default General method in the ECCO calculation routines in relation to flux calculations for heterogeneous cells (see Section 3.2.4). However, the results were also obtained using the Roth 6 method, which, as suggested by its name, was developed specifically for treating hexagonal lattices, which in general involve multiple rings of hexagons. Since Phase 1 involves only a single hexagon, the geometry was created unconventionally by assembling a degenerate lattice consisting of one ring only, i.e. the single hexagonal pin. The results obtained with the two methods are compared in Tables 4.6 and 4.7.

	General		**Roth 6**		
Quantity	**A. Infinite**	**Critical**	**A. Infinite**	**Critical**	**Unit**
k	1.35207	1.0000	1.35221	1.0000	#
B^2	0.0000	1.86698×10^{-3}	0.0000	1.86806×10^{-3}	cm^{-2}
Σ_a	5.47884×10^{-3}	5.19005×10^{-3}	5.47899×10^{-3}	5.19066×10^{-3}	cm^{-1}
$\Sigma_{\mathrm{a,fuel}}$	5.26678×10^{-3}	4.99338×10^{-3}	5.26679×10^{-3}	4.99389×10^{-3}	cm^{-1}
$\nu\Sigma_f$	7.38894×10^{-3}	7.59000×10^{-3}	7.38991×10^{-3}	7.59159×10^{-3}	cm^{-1}
Σ_{tr}	2.70825×10^{-1}	2.57346×10^{-1}	2.70880×10^{-1}	2.57390×10^{-1}	cm^{-1}
η	1.40293	1.52001	1.40311	1.52018	#
f	9.61294×10^{-1}	9.62107×10^{-1}	9.61271×10^{-1}	9.62092×10^{-1}	#

Table 4.6: 1-group quantities for Phase 1: multiplication factor k, buckling B^2, main macroscopic cross sections, reproduction factor η, and utilization factor f. The values are compared both for axially infinite and critical configurations for General and Roth 6 methods.

		General		Roth 6		
Isotope	**Quantity**	**A. Infinite**	**Critical**	**A. Infinite**	**Critical**	**Unit**
^{239}Pu	σ_c	4.46348E-1	3.73400E-1	4.46438E-1	3.73500E-1	b
^{239}Pu	σ_f	1.72480	1.69814	1.72490	1.69833	b
^{239}Pu	ν	2.93925	2.95080	2.93927	2.95082	#
^{241}Pu	σ_c	4.05293E-1	3.55038E-1	4.05356E-1	3.55111E-1	b
^{241}Pu	σ_f	2.39221	2.24477	2.39245	2.24509	b
^{241}Pu	ν	2.96546	2.97244	2.96547	2.97246	#
^{235}U	σ_c	5.10091E-1	4.46780E-1	5.10167E-1	4.46868E-1	b
^{235}U	σ_f	1.82902	1.70896	1.82921	1.70923	b
^{235}U	ν	2.45511	2.46391	2.45512	2.46392	#
^{238}U	σ_c	2.70765E-1	2.39577E-1	2.70699E-1	2.39548E-1	b
^{238}U	σ_f	3.66421E-2	4.66242E-2	3.66637E-2	4.66569E-2	b
^{238}U	ν	2.72276	2.72579	2.72290	2.72593	#
^{56}Fe	σ_c	8.17717E-3	7.49093E-3	8.19216E-3	7.50305E-3	b
^{208}Pb	σ_c	6.74317E-4	7.27047E-4	6.74395E-4	7.27088E-4	b
^{208}Pb	σ_{in}	2.59467E-2	3.37407E-2	2.59114E-2	3.36930E-2	b

Table 4.7: 1-group microscopic cross sections σ and the average number of neutrons emitted per fission event ν for Phase 1. The subscripts c, f, and in represent the capture, fission, and inelastic reactions. The values are compared both for axially infinite and critical configurations for General vs Roth 6 methods.

As shown in Tables 4.6 and 4.7, the differences in results between the two methods are practically negligible, at least for these simple geometries. To further illustrate this, Table 4.8 presents the differences (in absolute value) in microscopic cross sections between calculation methods for both axially infinite and critical cases, with the values expressed in pcm.

Isotope	Quantity	Δ A. Infinite [pcm]	Δ Critical [pcm]	Unit
^{239}Pu	σ_c	9	10	b
^{239}Pu	σ_f	10	19	b
^{239}Pu	ν	2	2	#
^{241}Pu	σ_c	6	7	b
^{241}Pu	σ_f	24	32	b
^{241}Pu	ν	1	2	#
^{235}U	σ_c	8	9	b
^{235}U	σ_f	19	27	b
^{235}U	ν	1	1	#
^{238}U	σ_c	7	3	b
^{238}U	σ_f	2	3	b
^{238}U	ν	14	14	#
^{56}Fe	σ_c	1	1	b
^{208}Pb	σ_c	0	0	b
^{208}Pb	σ_{in}	4	5	b

Table 4.8: Differences Δ (in absolute value) for microscopic cross sections and ν between the Roth 6 and General methods, Phase 1 axially infinite and critical configurations.

4.3 PHASE 2.1: Fuel Assembly Simulations

Phase 2.1 of the benchmark focuses on the study of a two-dimensional heterogeneous model of an inner-type fuel assembly (see Section 2.2). In modeling the cell, it was decided to include the fraction of inter-assembly lead corresponding to the coolant of the analyzed assembly (see Figure 4.10). As in the previous case, the boundary conditions were set in such a way as to recreate an infinite lattice of identical and axially infinite cells.

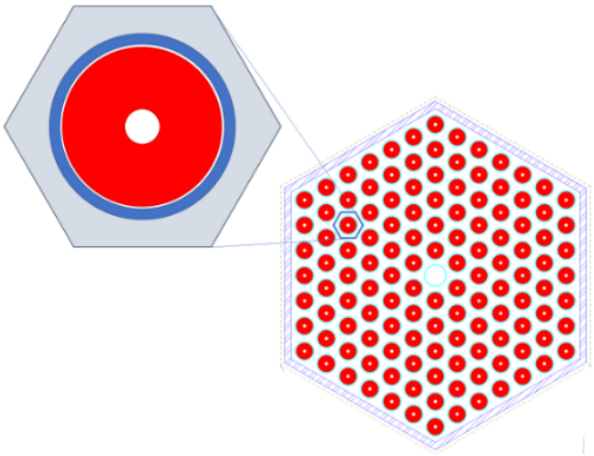

Figure 4.10: Fuel assembly model [20].

The benchmark requires to find the following quantities:

- The multiplication factor k.
- The fission and capture microscopic 1-group cross sections for ^{239}Pu, ^{241}Pu, ^{235}U, and ^{238}U, together with their average number of neutrons emitted per fission event ν.
- The 1-group inelastic scattering microscopic cross section for ^{238}U and ^{208}Pb.
- The 1-group capture microscopic cross sections for ^{56}Fe and ^{208}Pb.
- The reproduction factor $\eta = \dfrac{\nu\Sigma_f}{\Sigma_{a,fuel}}$.
- The utilization factor $f = \dfrac{\Sigma_{a,fuel}}{\Sigma_{a,tot}}$.
- The transport cross section $\Sigma_{tr} = \Sigma_t - \mu_0\Sigma_s$.

- The macroscopic fission, capture, elastic, and inelastic cross sections for the 7-group discretization.
- The five isotope and reaction combinations that give the highest k sensitivity coefficients and uncertainties.

Furthermore, for comparing purposes only, the calculation for the critical configuration (Critical calculation routine was used) was repeated, as in Phase 1.

4.3.1 Phase 2.1 Execution

As for the previous case, Phase 2.1 was studied using the ECCO cell code. For this case, in addition to the materials and media defined previously, the 'VOID' medium was implemented, which was used to model the dummy pin region (see Section 2.2.2). After implementing the materials, the geometry was defined as in Listing 4.2.

```
1  CELL   'FUEL_ASSEMBLY_CELL'
2  COMPOSITION_ORDER
3    'lead_med' 'AIM1_med' 'MOX_med' 'VOID_med'
4  GEOMETRY DATA
5   HEXAGON 3 (W_IN)
6    HEXAGONAL LATTICE (N_RING) (PIN_PITCH) 2
7      CYLINDRICAL 2
8       (R_D_CLAD_IN) REGION 1  'void_dummy' COMP 4 (TEMP_CELSIUS+273.15)
9       (R_D_CLAD_OUT) REGION 2  'clad_dummy' COMP 2 (TEMP_CELSIUS+273.15)
10     IN
11     REGION  3  'lead_dummy' COMP 1   (TEMP_CELSIUS+273.15)
12     CYLINDRICAL 2
13      (R_EXT_GAP)   REGION 4  'fuel' COMP 3   (TEMP_CELSIUS+273.15)
14      (R_EXT_CLAD)  REGION 5  'clad' COMP 2   (TEMP_CELSIUS+273.15)
15     IN
16     REGION  6  'lead' COMP 1   (TEMP_CELSIUS+273.15)
17     1 2 2 2 2 2 2
18     IN
19     REGION  7  'lead_flow' COMP 1   (TEMP_CELSIUS+273.15)
20     (W_OUT)
21     REGION  8   'wrapper' COMP 2  (TEMP_CELSIUS+273.15)
22     (SA_PITCH)
23     REGION  9   'bypass'  COMP 1  (TEMP_CELSIUS+273.15)
24   REFLECT
25 END OF GEOMETRY DATA
26 ;
```

Listing 4.2: Geometry of fuel assembly cell for benchmark Phase 2.1.

As can be seen from line 24, the reflection boundary condition was applied to the outer face of the hexagon. The geometry was defined starting from the three nested hexagons that define the region of the assembly wrapper and the fraction of coolant outside it, called 'bypass' in the listing. Subsequently, the hexagonal pin lattice was defined using the HEXAGON LATTICE command, in which the number of rings characterizing the lattice and the types of pins implemented were specified. In this case, the two types of pins that were implemented are the dummy pin and the fuel pin, respectively. In line

17, the type of pin contained in each ring of the lattice was defined starting from the innermost ring, repeated as many times as the number of rings previously defined.
Then, the ECCO routines defined for Phase 1 were used to obtain the required results and to provide the condensed and homogenized cross sections to ERANOS for performing the sensitivity and uncertainty analysis. For Phase 2.1, the results obtained using the General method will be presented first, followed by a comparison with those achieved using the Roth 6 method.

4.3.2 Phase 2.1 Results

1-group macroscopic cross sections and integral parameters

In Table 4.9, the parameters that are input data for the calculation routines are highlighted in red. It can be seen that, as in Phase 1, the critical cell presents a harder neutron spectrum and shows higher values of ν and Σ_f, even though, again, the microscopic fission cross section for fissile isotopes is higher in the axially infinite case (see Table 4.10). This remarks the importance of fissionable isotopes in a cell/reactor characterized by a fast neutron spectrum.

Quantity	**Axially Infinite configuration**	**Critical configuration**	**Unit**
k	1.27819	1.0000	#
B^2	0.0000	1.33006×10^{-3}	cm^{-2}
Σ_a	4.87732×10^{-3}	4.64099×10^{-3}	cm^{-1}
$\Sigma_{\mathrm{a,fuel}}$	4.58094×10^{-3}	4.36394×10^{-3}	cm^{-1}
$\nu\Sigma_f$	6.22053×10^{-3}	6.32225×10^{-3}	cm^{-1}
Σ_f	2.12810×10^{-3}	2.15909×10^{-3}	cm^{-1}
Σ_{tr}	2.73044×10^{-1}	2.61599×10^{-1}	cm^{-1}
η	1.35792	1.44875	#
f	9.39232×10^{-1}	9.40305×10^{-1}	#

Table 4.9: 1-group output quantities for Phase 2.1: multiplication factor k, buckling B^2, main macroscopic cross sections, reproduction factor η, and utilization factor f. The values are presented both for axially infinite and critical configurations.

Isotope	Quantity	Axially Infinite configuration	Critical configuration	Unit
^{239}Pu	σ_c	4.97566×10^{-1}	4.30927×10^{-1}	b
^{239}Pu	σ_f	1.76403	1.73502	b
^{239}Pu	ν	2.93500	2.94393	#
^{241}Pu	σ_c	4.36060×10^{-1}	3.91242×10^{-1}	b
^{241}Pu	σ_f	2.49383	2.36006	b
^{241}Pu	ν	2.96309	2.96820	#
^{235}U	σ_c	5.47788×10^{-1}	4.91494×10^{-1}	b
^{235}U	σ_f	1.91086	1.80196	b
^{235}U	ν	2.45248	2.45899	#
^{238}U	σ_c	2.87142×10^{-1}	2.60123×10^{-1}	b
^{238}U	σ_f	3.33734×10^{-2}	4.09367×10^{-2}	b
^{238}U	ν	2.71981	2.72227	#
^{56}Fe	σ_c	8.25634×10^{-3}	7.64046×10^{-3}	b
^{208}Pb	σ_c	6.65240×10^{-4}	7.08432×10^{-4}	b
^{208}Pb	σ_{in}	2.24075×10^{-2}	2.79476×10^{-2}	b

Table 4.10: 1-group microscopic cross sections σ and the average number of neutrons emitted per fission event ν for Phase 2.1. The values are presented for both the axially infinite and critical configurations. The subscripts c, f, and in represent the capture, fission, and inelastic reactions.

What might be less obvious is seeing the values of k, η, and f decrease in the case of the fuel assembly cell compared to the fuel pin cell, for both types of calculations. This is due to a decrease in the fuel volume fraction within the assembly, as each cell has a fraction of void and wrapper that was not present in the pin case. Therefore, even in the case of an infinite lattice, where the fuel is infinite, there is still a lower fraction of fuel per individual cell. Another important aspect is the buckling found for the Critical calculation routine. Comparing the buckling with that of Phase 1 (see Table 4.2), it is observed that it is larger in the case of the single fuel pin. This reinforces what has been said so far regarding the higher volumetric fraction of fuel in the pin cell compared to that of the assembly, and therefore in the former a smaller volume of material is required to achieve criticality.

Uncertainty and sensitivity analysis for the axially infinte configuration

The five most impactful isotope and reaction combinations in terms on k sensitivity and uncertainty (see Sections 3.4 and 3.5) were chosen among the main isotopes involved in the previous benchmark requests. Similarly to Phase 1, they were calculated in ERANOS with condensed cross sections at 33 groups. In Table 4.11, where sensitivities are

displayed as sums of the contributions related to all energy groups, it can be seen that the k is particularly sensible to the ^{239}Pu fission, as in Phase 1. It can be noticed that, in Phase 2.1, the sensitivities due to fission microscopic cross sections of fissile isotopes are higher than those recorded in the single fuel pin case. This is due to the different fuel fractions contained in the two cells and the distribution of the neutron spectrum. Comparing the microscopic cross sections reported in Tables 4.1 and 4.10, it emerges that the neutron spectrum in the case of the fuel assembly is softer, as the fission microscopic cross sections for fissile isotopes are higher than those of the fuel pin case, and vice versa for the fission microscopic cross sections of the fissionable isotopes.

$\boldsymbol{\alpha}$	$\boldsymbol{S(k,\alpha)}$
$\sigma_f^{^{239}\mathrm{Pu}}$	4.7166×10^{-1}
$\sigma_c^{^{238}\mathrm{U}}$	-2.2671×10^{-1}
$\sigma_f^{^{241}\mathrm{Pu}}$	7.3591×10^{-2}
$\sigma_{in}^{^{238}\mathrm{U}}$	-6.2494×10^{-2}
$\sigma_c^{^{239}\mathrm{Pu}}$	-5.4890×10^{-2}

Table 4.11: Most relevant sensitivity coefficients $S(k,\alpha)$ of the multiplication factor k to the input data α for Phase 2.1.

Considering the higher output uncertainties reported in Table 4.12, it can be observed that, although the fission cross section of plutonium gives the largest contribution in terms of sensitivity, it also has the greatest uncertainty. However, as observed in Phase 1, this uncertainty is comparable to those present in the ranking and is two orders of magnitude smaller than the own sensitivity coefficient.

$\boldsymbol{\alpha}$	$\boldsymbol{\varepsilon(k,\alpha)}$
$\sigma_f^{^{239}\mathrm{Pu}}$	5.53310×10^{-3}
$\sigma_c^{^{238}\mathrm{U}}$	3.28260×10^{-3}
$\sigma_c^{^{239}\mathrm{Pu}}$	3.06630×10^{-3}
$\sigma_{in}^{^{238}\mathrm{U}}$	2.95370×10^{-3}
$\sigma_{in}^{^{239}\mathrm{Pu}}$	1.43420×10^{-3}

Table 4.12: Most relevant uncertainties $\varepsilon(k,\alpha)$ of the multiplication factor k to the input data α for Phase 2.1.

7-group macroscopic cross sections for the axially infinite configuration

Table 4.13 shows the macroscopic fission, capture, elastic and inelastic cross sections at 7 energy groups, for the infinite cell case. The groups are numbered from 1 to 7

in descending energy order. It can be observed that the fission cross sections initially decrease, and then follow an increasing trend. For group 1, which includes neutrons with energies above 2 MeV, the fission cross section is larger compared to groups 2, 3, 4, and 5. This is due to fissions occurring in the fast region, involving fissionable isotopes that exhibit higher microscopic fission cross sections at high energies. Starting from group 5, the likelihood of fission increases until it reaches a maximum in group 7, which corresponds to thermal neutrons. In fact, at thermal energies, fissile materials have microscopic cross sections that are orders of magnitude larger than those of fissionable materials (see Figure 4.8). The difference of only two orders of magnitude between the values of group 1 and group 7 is due to the higher concentration of fissionable isotopes compared to fissile ones, which increases the fission cross section of group 1 (see Eq. (4.4)).

Group	$\boldsymbol{\Sigma_f}$ **[cm^{-1}]**	$\boldsymbol{\Sigma_c}$ **[cm^{-1}]**	$\boldsymbol{\Sigma_{el}}$ **[cm^{-1}]**	$\boldsymbol{\Sigma_{in}}$ **[cm^{-1}]**
1	6.16505×10^{-3}	1.10511×10^{-3}	1.70487×10^{-1}	5.70061×10^{-2}
2	2.72180×10^{-3}	8.57478×10^{-4}	1.99223×10^{-1}	2.16799×10^{-2}
3	1.55154×10^{-3}	1.37110×10^{-3}	3.12897×10^{-1}	7.28359×10^{-3}
4	1.93563×10^{-3}	4.81136×10^{-3}	4.38265×10^{-1}	7.14300×10^{-4}
5	5.70937×10^{-3}	1.52861×10^{-2}	4.67522×10^{-1}	7.70350×10^{-12}
6	5.09056×10^{-2}	9.91938×10^{-2}	4.77298×10^{-1}	3.53622×10^{-18}
7	2.19376×10^{-1}	2.08257×10^{-1}	5.16920×10^{-1}	2.54689×10^{-18}

Table 4.13: 7-group macroscopic cross sections Σ for Phase 2.1. The values are presented for the axially infinite configuration. The subscripts f, c, el, and in represent the fission, capture, elastic, and inelastic reactions.

4.3.3 Further Considerations on Phase 2.1

Tables 4.14 and 4.15 compare the results obtained using the two methods, as for Phase 1. It is evident that, unlike the previous phase, there is a greater discrepancy between the results obtained with the two methods, which is due to the increased complexity of the geometry. Moreover, as previously explained, the Roth 6 method was specifically developed to handle hexagonal lattices, so it can be considered more reliable in this case. The differences with respect to the Roth 6 method for the Axially Infinite case are presented in Tables 4.16 and 4.17 (the values are expressed in pcm rounding decimal numbers).

	General		Roth 6		
Quantity	**A. Infinite**	**Critical**	**A. Infinite**	**Critical**	**Unit**
k	1.27819	1.0000	1.28283	1.0000	#
B^2	0.0000	1.33006×10^{-3}	0.0000	1.34121×10^{-3}	cm^{-2}
Σ_a	4.87732×10^{-3}	4.64099×10^{-3}	4.85933×10^{-3}	4.62680×10^{-3}	cm^{-1}
$\Sigma_{a,fuel}$	4.58094×10^{-3}	4.36394×10^{-3}	4.56424×10^{-3}	4.35097×10^{-3}	cm^{-1}
$\nu\Sigma_f$	6.22053×10^{-3}	6.32225×10^{-3}	6.21994×10^{-3}	6.32494×10^{-3}	cm^{-1}
Σ_f	2.12810×10^{-3}	2.15909×10^{-3}	2.12774×10^{-3}	2.15982×10^{-3}	cm^{-1}
Σ_{tr}	2.73044×10^{-1}	2.61599×10^{-1}	2.72558×10^{-1}	2.61175×10^{-1}	cm^{-1}
η	1.35792	1.44875	1.36276	1.45368	#
f	9.39232×10^{-1}	9.40305×10^{-1}	9.39272×10^{-1}	9.40384×10^{-1}	#

Table 4.14: 1-group quantities for Phase 2.1: multiplication factor k, buckling B^2, main macroscopic cross sections, reproduction factor η, and utilization factor f. The values are compared both for axially infinite and critical configurations for General vs Roth 6 methods.

		General		Roth 6		
Isotope	**Quantity**	**A. Infinite**	**Critical**	**A. Infinite**	**Critical**	**Unit**
^{239}Pu	σ_c	4.97566E-1	4.30927E-1	4.93653E-1	4.27648E-1	b
^{239}Pu	σ_f	1.76403	1.73502	1.76208	1.73379	b
^{239}Pu	ν	2.93500	2.94393	2.93530	2.94426	#
^{241}Pu	σ_c	4.36060E-1	3.91242E-1	4.33637E-1	3.89194E-1	b
^{241}Pu	σ_f	2.49383	2.36006	2.48648	2.35414	b
^{241}Pu	ν	2.96309	2.96820	2.96327	2.96841	#
^{235}U	σ_c	5.47788E-1	4.91494E-1	5.44892E-1	4.89041E-1	b
^{235}U	σ_f	1.91086	1.80196	1.90488	1.79712	b
^{235}U	ν	2.45248	2.45899	2.45274	2.45928	#
^{238}U	σ_c	2.87142E-1	2.60123E-1	2.85236E-1	2.58516E-1	b
^{238}U	σ_f	3.33734E-2	4.09367E-2	3.36093E-2	4.12174E-2	b
^{238}U	ν	2.71981	2.72227	2.72030	2.72277	#
^{56}Fe	σ_c	8.25634E-3	7.64046E-3	8.22405E-3	7.60986E-3	b
^{208}Pb	σ_c	6.65240E-4	7.08432E-4	6.67805E-4	7.10718E-4	b
^{208}Pb	σ_{in}	2.24075E-2	2.79476E-2	2.24779E-2	2.80199E-2	b

Table 4.15: 1-group microscopic cross sections σ and the average number of neutrons emitted per fission event ν for Phase 2.1. The subscripts c, f, and in represent the capture, fission, and inelastic reactions. The values are compared both for axially infinite and critical configurations for General vs Roth 6 methods.

Isotope	Quantity	Δ A. Infinite [pcm]	Unit
^{239}Pu	σ_c	-391	b
^{239}Pu	σ_f	-195	b
^{239}Pu	ν	30	#
^{241}Pu	σ_c	-242	b
^{241}Pu	σ_f	-735	b
^{241}Pu	ν	18	#
^{235}U	σ_c	-290	b
^{235}U	σ_f	-598	b
^{235}U	ν	26	#
^{238}U	σ_c	-191	b
^{238}U	σ_f	24	b
^{238}U	ν	49	#
^{56}Fe	σ_c	-3	b
^{208}Pb	σ_c	0	b
^{208}Pb	σ_{in}	7	b

Table 4.16: Differences Δ with respect to Roth 6 for microscopic cross sections and ν, Phase 2.1 axially infinite configuration.

Quantity	Δ A. Infinite [pcm]	Unit
k	464	#
B^2	0	cm^{-2}
Σ_a	-2	cm^{-1}
$\Sigma_{\mathrm{a,fuel}}$	-2	cm^{-1}
$\nu\Sigma_f$	0	cm^{-1}
Σ_f	0	cm^{-1}
Σ_{tr}	-49	cm^{-1}
η	484	#
f	4	#

Table 4.17: Differences with respect to Roth 6 method for 1-group quantities: multiplication factor k, buckling B^2, main macroscopic cross sections, reproduction factor η, and utilization factor f, Phase 2.1 axially infinite configuration.

Table 4.17 highlights how the difference in k is larger than in the previous phase (only 14 pcm). However, this value decreases from 464 pcm to about 100 pcm when comparing the multiplication factor obtained through a 7-group energy condensation.
It may be interesting to further investigate these differences based on the validation tests of the General method shown in [4].

4.4 PHASE 2.2: Absorber Super-cell Simulations

Phase 2.2 of the benchmark focuses on studying a two-dimensional heterogeneous model of a control rod assembly (see Subsection 2.2.3) surrounded by inner-type fuel assemblies (see Section 2.2). In modeling the super-cell, it was decided to include the fraction of inter-assembly lead corresponding to the coolant of the analyzed assemblies (see Figure 4.11), and as in the previous case, the boundary conditions were set to recreate an infinite lattice of identical and axially infinite super-cells.

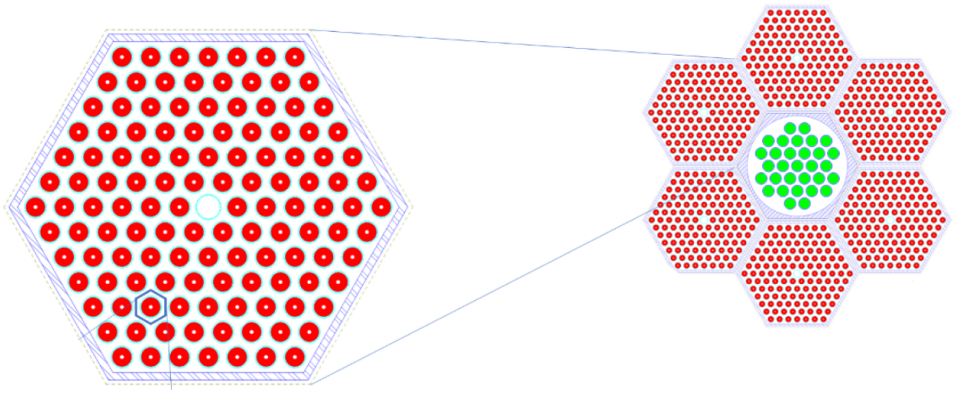

Figure 4.11: Control rod assembly surrounded by fuel assembly model [20].

The benchmark requires to find the following quantities:

- The multiplication factor k.
- The fission and capture microscopic 1-group cross sections for ^{239}Pu, ^{241}Pu, ^{235}U, and ^{238}U, together with their average number of neutrons emitted per fission event ν.
- The 1-group inelastic scattering microscopic cross section for ^{238}U and ^{208}Pb.
- The 1-group capture microscopic cross sections for ^{56}Fe and ^{208}Pb.
- The 1-group capture microscopic cross sections for ^{10}B.
- The reproduction factor $\eta = \dfrac{\nu\Sigma_f}{\Sigma_{a,fuel}}$.
- The utilization factor $f = \dfrac{\Sigma_{a,fuel}}{\Sigma_{a,tot}}$.
- The transport cross section $\Sigma_{tr} = \Sigma_t - \mu_0\Sigma_s$.

- The macroscopic fission, capture, elastic, and inelastic cross sections for the 7-group discretization.
- The five isotope and reaction combinations that give the highest k sensitivity coefficients and uncertainties.

Notice that, unlike the previous cases, a comparison between the critical and the axially infinite case is not made, since in Phase 2.2, it is decided to adopt a single fuel ring, which does not ensure the criticality of the cell. This choice will be justified during the analysis of the results.
Moreover, Phase 2.2 was carried out using two approaches: the first approach was the same as that used for all other phases, in which a single geometry for the whole model was defined and resolved using the computational routines developed for Phase 1; the second one was used to observe how the 1-group microscopic capture cross sections for ^{10}B vary when studying the control rod assembly as a subcritical cell, which receives the flux from a fuel assembly. This explanation will be elaborated further below.

4.4.1 Phase 2.2 Execution with the First Approach

As for the previous case, Phase 2.2 was solved using the ECCO cell code; however, unlike Phase 2.1, only the General method was used, as Roth cannot handle a lattice of lattices. In this case, the 'B$_4$C' medium, with the enrichment of the control part, was implemented in addition to materials and media defined previously. After that, the geometry was defined through Listing4.3.

```
CELL   'CONTROL_super-cell'
  COMPOSITION_ORDER
    'lead_med' 'AIM1_med' 'MOX_med' 'VOID_med' 'B4C_med'
 GEOMETRY DATA
 HEXAGONAL LATTICE (N_RING_SUPER) (SA_PITCH) 2 !START LAT super-cell
   HEXAGON 2 (W_IN)        !DEFINITION OF FUEL ASSEMBLY
   HEXAGONAL LATTICE (N_RING) (PIN_PITCH) 2
   CYLINDRICAL 2
   (R_D_CLAD_IN) REGION 1  'void_dummy' COMP 4 (TEMP_CELSIUS+273.15)
   (R_D_CLAD_OUT) REGION 2  'clad_dummy' COMP 2 (TEMP_CELSIUS+273.15)
   IN
   REGION  3  'lead_dummy' COMP 1   (TEMP_CELSIUS+273.15)
   CYLINDRICAL 2
   (R_EXT_GAP)   REGION 4  'fuel' COMP 3   (TEMP_CELSIUS+273.15)
   (R_EXT_CLAD)  REGION 5  'clad' COMP 2   (TEMP_CELSIUS+273.15)
   IN
   REGION  6  'lead' COMP 1   (TEMP_CELSIUS+273.15)
   1 2 2 2 2 2 2
   IN
   REGION  7  'lead_flow' COMP 1   (TEMP_CELSIUS+273.15)
   (W_OUT)
   REGION  8   'wrapper' COMP 2  (TEMP_CELSIUS+273.15)
   IN
   REGION  9   'bypass'  COMP 1  (TEMP_CELSIUS+273.15) ! END DEFINITION FUEL ASSEMBLY

   HEXAGON 1 (W_OUT)   !DEFINITION OF CONTROL ASSEMBLY
```

```
27    CYLINDRICAL 1 (R_W_CR)
28    HEXAGONAL LATTICE (N_RING_CR) (PIN_PITCH_CR) 2
29    CYLINDRICAL 1
30    (R_CR) REGION 10  'lead_pin' COMP 1 (TEMP_CELSIUS+273.15)
31    IN
32    REGION  11  'lead_cr' COMP 1   (TEMP_CELSIUS+273.15)
33    CYLINDRICAL 3
34    (R_CR)   REGION 12  'absorber' COMP 5   (TEMP_CELSIUS+273.15)
35    (R_CR_CLAD_IN)  REGION 13  'void_cr' COMP 4 (TEMP_CELSIUS+273.15)
36    (R_CR_CLAD_OUT)  REGION 14 'clad_cr' COMP 2 (TEMP_CELSIUS+273.15)
37    IN
38    REGION  15  'lead' COMP 1   (TEMP_CELSIUS+273.15)
39    GENERAL
40    2
41    2 2 2 2 2 2
42    2 2 2 2 2 2 2 2 2 2 2 2
43    1 2 2 1 2 2 1 2 2 1 2 2 1 2 2 1 2 2
44    IN
45    REGION  16  'lead_flow_cr' COMP 1   (TEMP_CELSIUS+273.15)
46    IN
47    REGION  17   'wrapper_cr' COMP 2  (TEMP_CELSIUS+273.15)
48    IN
49    REGION  18   'bypass_cr'  COMP 1  (TEMP_CELSIUS+273.15) ! END CONTROL ASSEMBLY
50  2 1          ! END LATTICE super-cell
51    REFLECT     ! BOUNDARY CONDITION super-cell
52    END OF GEOMETRY DATA
53
54  ;
```

Listing 4.3: Geometry of control super-cell for benchmark Phase 2.2.

In line 51, the reflection boundary condition was applied to the outer face of geometry. The geometry of the super-cell was defined as an assembly of control rods surrounded by one ring of fuel assemblies. This macrostructure was created using the HEXAGONAL LATTICE command on line 5, setting the option for the number of cell types in the lattice to 2. The cell of type 1 is the fuel cell, which is identical to that defined in Phase 2.1. The cell of type 2, on the other hand, is that of the control rods. It is itself a hexagonal lattice composed of two types of pins. It was necessary to define an absorber pin and a dummy pin filled with lead because, within the assembly, the control rods form a lattice where in some positions the control rod gives way to the coolant (see Figure 2.7). Given the presence of different pins within the same ring, the GENERAL command was used to choose the type of each pin that makes up the lattice (see lines 39 to 43). Finally, on line 50, the two rings that make up the super-cell are defined, with the innermost being the control ring.
Notice that the choice to adopt a single fuel assembly ring derived from the fact that with more than two rings of hexagons that are themselves hexagonal lattice, the geometry was too complicated and the results are wrong. For instance, with two fuel assembly rings, the k is 1.75 and this is impossible since it was 1.27819 in Phase 2.1, where there are only fuel assemblies in the infinite lattice.

4.4.2 Phase 2.2 Results

1-group macroscopic cross sections and integral parameters

Table 4.18 shows the results obtained using the Axially Infinite ECCO computational routines, with input data highlighted in red (see Figure 4.4).

Quantity	Axially Infinite configuration	Unit
k	8.73467×10^{-1}	#
B^2	0.0000	cm^{-2}
Σ_a	6.35599×10^{-3}	cm^{-1}
$\Sigma_{a,fuel}$	3.71542×10^{-3}	cm^{-1}
$\nu\Sigma_f$	5.54086×10^{-3}	cm^{-1}
Σ_f	1.89132×10^{-3}	cm^{-1}
Σ_{tr}	3.01011×10^{-1}	cm^{-1}
η	1.49131	#
f	5.84555×10^{-1}	#

Table 4.18: 1-group output quantities for Phase 2.2: multiplication factor k, buckling B^2, main macroscopic cross sections, reproduction factor η, and utilization factor f.

It can be seen that k is less than one, confirming the subcriticality of the super-cell. An important aspect noted during the simulations is that in Phase 2.2, contrary to simple cells (i.e. those of Phase 1 and 2.1) for which the k calculated with a 1-group condensation matches those obtained in multi-group calculations, the greater cell complexity requires increased calculation precision. Table 4.19 compares the values of k calculated by condensing to 1, 7 and 33 groups both in ECCO and BISTRO.

G	k (ECCO)	k (BISTRO)
1	8.73467×10^{-1}	8.73905×10^{-1}
7	9.07372×10^{-1}	9.06960×10^{-1}
33	9.13384×10^{-1}	9.13018×10^{-1}

Table 4.19: Comparison of k between ECCO and BISTRO or 1, 7, and 33 group condensations for Phase 2.2.

In BISTRO, a Cartesian geometry with reflective boundary conditions was defined, to which the macroscopic cross sections, condensed and homogenized in ECCO, were applied. The transport equation was solved for this geometry using the discrete ordinate and the finite difference methods (see Section 3.3). It is important to note that, in general, when studying an infinite homogeneous domain in BISTRO, that represents a

single cell in ECCO, the actual adopted geometry becomes of minor significance since there is no spatial variation in the neutron flux to consider. For example, a complex heterogeneous infinite cell can be modeled in BISTRO (after homogenization in ECCO) using a simple slab of arbitrary length with reflective boundary conditions. The only true concern is selecting a proper spatial discretization.
Regarding the integral parameters (see Table 4.18), it can be observed that, due to the presence of ^{10}B in the absorber pins, the Σ_a is larger than in Phase 2.1. This, combined with a smaller $\Sigma_{\text{a,fuel}}$, leads to a lower utilization factor for Phase 2.2. Furthermore, although ν is higher for Phase 2.2 compared to that of the axially infinite configuration for Phase 2.1 (this indicates a harder neutron spectrum), the Σ_f is lower. This is caused by the reduced fuel concentrations in the super-cell under consideration, as it contains a non-fuel assembly.

1-group microscopic quantities

Table 4.20 confirms that the neutron spectrum is harder compared to Phase 2.1 since the ^{238}U fission microscopic cross section is larger.

Isotope	**Quantity**	**Axially Infinite configuration**	**Unit**
^{239}Pu	σ_c	4.01244×10^{-1}	b
^{239}Pu	σ_f	1.76328	b
^{239}Pu	ν	2.94623	#
^{241}Pu	σ_c	3.76655×10^{-1}	b
^{241}Pu	σ_f	2.35030	b
^{241}Pu	ν	2.96959	#
^{235}U	σ_c	4.74038×10^{-1}	b
^{235}U	σ_f	1.78972	b
^{235}U	ν	2.46136	#
^{238}U	σ_c	2.53228×10^{-1}	b
^{238}U	σ_f	4.31081×10^{-2}	b
^{238}U	ν	2.72212	#
^{56}Fe	σ_c	7.13324×10^{-3}	b
^{208}Pb	σ_c	7.14255×10^{-4}	b
^{208}Pb	σ_{in}	2.67603×10^{-2}	b
^{10}B	σ_c	1.51920	b

Table 4.20: 1-group microscopic cross sections σ and the average number of neutrons emitted per fission event ν for Phase 2.2. The subscripts c, f, and in represent the capture, fission, and inelastic reactions.

7-group macroscopic cross sections

Considering the 7-group macroscopic cross sections displayed in Table 4.21, a similar trend to that described for the Phase 2.1 infinite cell can be observed. However, a lower value for the respective groups can be noted for the fission cross sections due to the dilution of the fuel concentrations. This can be observed in Table 4.22, which shows the relative differences of Σ_f between Phases 2.1 and 2.2. On the other hand, Table 4.23 shows increased capture cross sections in Phase 2.2, which can be attributed to the presence of ^{10}B. This difference would be much larger if the absorber rods were shutdown rods rather than control ones. The value for Phase 2.2 increases towards the thermal group 7, as the capture of ^{10}B increases at thermal energies, as shown in Figure 4.12.

Group	$\mathbf{\Sigma_f}$ **[cm^{-1}]**	$\mathbf{\Sigma_c}$ **[cm^{-1}]**	$\mathbf{\Sigma_{el}}$ **[cm^{-1}]**	$\mathbf{\Sigma_{in}}$ **[cm^{-1}]**
1	5.75845×10^{-3}	1.37239×10^{-3}	1.71854×10^{-1}	5.62675×10^{-2}
2	2.45154×10^{-3}	1.27979×10^{-3}	2.00286×10^{-1}	2.02639×10^{-2}
3	1.36684×10^{-3}	3.07829×10^{-3}	3.13065×10^{-1}	6.58684×10^{-3}
4	1.68897×10^{-3}	8.49664×10^{-3}	4.34572×10^{-1}	7.28260×10^{-4}
5	5.08689×10^{-3}	2.24821×10^{-2}	4.67512×10^{-1}	7.44856×10^{-12}
6	4.71473×10^{-2}	1.04724×10^{-1}	4.77161×10^{-1}	3.25805×10^{-18}
7	1.65882×10^{-1}	2.21601×10^{-1}	5.20491×10^{-1}	2.63935×10^{-18}

Table 4.21: 7-group macroscopic cross sections Σ for Phase 2.2. The subscripts f, c, el, and in represent the fission, capture, elastic, and inelastic reactions.

Group	$\mathbf{\Sigma_f}$ **Case 2.2 [cm^{-1}]**	$\mathbf{\Sigma_f}$ **Case 2.1 [cm^{-1}]**	**Relative difference**
1	5.75845×10^{-3}	6.16505×10^{-3}	-6.60%
2	2.45154×10^{-3}	2.72180×10^{-3}	-9.93%
3	1.36684×10^{-3}	1.55154×10^{-3}	-11.90%
4	1.68897×10^{-3}	1.93563×10^{-3}	-12.74%
5	5.08689×10^{-3}	5.70937×10^{-3}	-10.90%
6	4.71473×10^{-2}	5.09056×10^{-2}	-7.38%
7	1.65882×10^{-1}	2.19376×10^{-1}	-24.38%

Table 4.22: Relative differences in fission macroscopic cross-sections Σ_f between Phases 2.2 and 2.1, where the values are presented for the axially infinite configuration.

Group	Σ_c Case 2.2 (cm^{-1})	Σ_c Case 2.1 (cm^{-1})	Relative difference
1	1.37239×10^{-3}	1.10511×10^{-3}	24.19%
2	1.27979×10^{-3}	8.57478×10^{-4}	49.25%
3	3.07829×10^{-3}	1.37110×10^{-3}	124.51%
4	8.49664×10^{-3}	4.81136×10^{-3}	76.60%
5	2.24821×10^{-2}	1.52861×10^{-2}	47.08%
6	1.04724×10^{-1}	9.91938×10^{-2}	5.58%
7	2.21601×10^{-1}	2.08257×10^{-1}	6.41%

Table 4.23: Relative differences in capture macroscopic cross-sections Σ_c between Phases 2.2 and 2.1 for the axially infinite configuration.

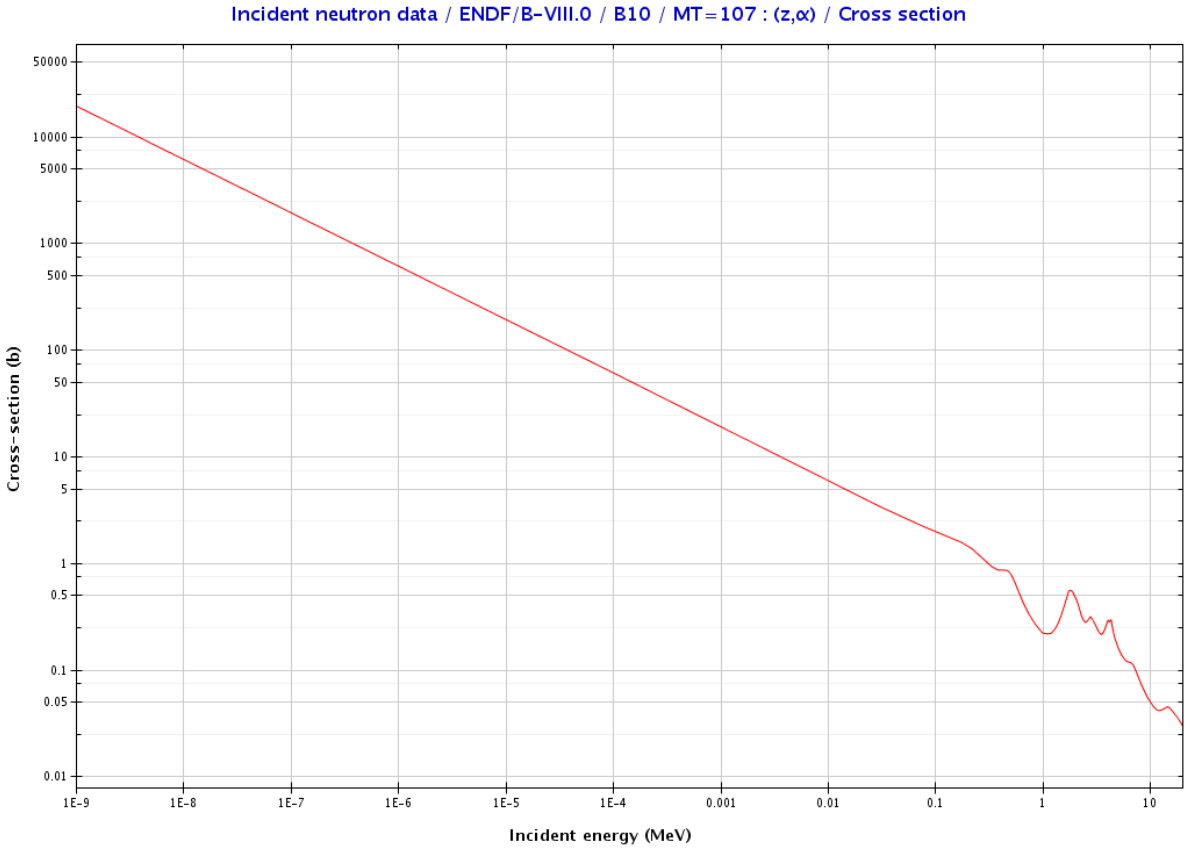

Figure 4.12: ^{10}B microscopic capture cross section from ENDF/B-VIII.0 Nuclear Data Library [21].

Uncertainty and sensitivity analysis

The five most impactful isotope and reaction combinations in terms of k sensitivity and uncertainty (see Sections 3.4 and 3.5) were chosen among the main isotopes involved in the previous benchmark requests. Similarly to Phase 1, they were calculated in ERANOS with condensed cross sections at 33 groups.

$\boldsymbol{\alpha}$	$\boldsymbol{S(k,\alpha)}$
$\sigma_f^{^{239}\mathrm{Pu}}$	5.2549×10^{-1}
$\sigma_c^{^{10}\mathrm{B}}$	-2.1244×10^{-1}
$\sigma_c^{^{238}\mathrm{U}}$	-1.1964×10^{-1}
$\sigma_{in}^{^{238}\mathrm{U}}$	-7.8427×10^{-2}
$\sigma_f^{^{241}\mathrm{Pu}}$	7.5585×10^{-2}

Table 4.24: Most relevant sensitivity coefficients $S(k,\alpha)$ of the multiplication factor k to the input data α for Phase 2.2.

As in the previous case, the leading sensitivity coefficient is that with respect to the fission of ^{239}Pu (see Table 4.24). The second one is ^{10}B, with a negative contribution on k. Considering the highest uncertainties reported in Table 4.25, it can be observed that, although the fission cross section of plutonium gives the largest contribution in terms of sensitivity, it also has the greatest uncertainty. However, as observed in Phase 1, this uncertainty is comparable to those present in the ranking and is two orders of magnitude smaller than the associated sensitivity coefficient. Interestingly, the k uncertainty related to ^{10}B does not feature among the most relevant, despite the related sensitivity being ranked 2nd.

$\boldsymbol{\alpha}$	$\boldsymbol{\varepsilon(k,\alpha)}$
$\sigma_f^{^{239}\mathrm{Pu}}$	6.34510×10^{-3}
$\sigma_{in}^{^{238}\mathrm{U}}$	2.87070×10^{-3}
$\sigma_c^{^{238}\mathrm{U}}$	2.04920×10^{-3}
$\sigma_{in}^{^{239}\mathrm{Pu}}$	1.55840×10^{-3}
$\sigma_c^{^{239}\mathrm{Pu}}$	1.48280×10^{-3}

Table 4.25: Most relevant uncertainties $\varepsilon(k,\alpha)$ of the multiplication factor k to the input data α for Phase 2.2.

4.4.3 Phase 2.2 Study of the ^{10}B Capture Cross section with Subcritical Cell

The investigation of the ^{10}B capture cross section also was conducted using the subcritical cell approach. This approach involves defining the fuel assembly and the absorber assembly separately, without implementing a hexagonal lattice (super-cell) in which the rings of assemblies are defined. The geometry of the fuel assembly was treated in ECCO using the axially infinite calculation routine, from which the flux was extracted and sent to the control assembly, acting as an imposed neutron source. The routine for the fuel assembly alone was analogous to that of the model considered for Phase 2.1. Once the flux was obtained, it was possible to study the control cell, providing it with the flux and defining its buckling as

$$B^2 = \frac{5}{8}\left(\frac{\pi}{\mathrm{H}}\right)^2, \tag{4.5}$$

where H is a characteristic dimension of the cell, corresponding in this case to its radial thickness [3]. This buckling accounts for neutron leakage from the cell. After performing the calculation steps by condensing the cross sections to a single energy group, the ^{10}B capture cross section was extracted. Additionally, a second calculation for the subcritical cell was performed, in which only the flux from the fuel assembly was provided as input and the buckling was set to zero to achieve an axially infinite configuration. The results for the ^{10}B capture cross section are presented in Table 4.26 for the various calculation modes considered.

Calculation Mode	$\boldsymbol{\sigma_c^{^{10}\mathrm{B}}}$ **[b]**
Super-cell	1.51920
Subcritical ($B^2 = 0$)	1.70482
Subcritical ($B^2 > 0$ through Eq. (4.5))	1.83432

Table 4.26: Comparison of ^{10}B capture values for different calculation modes.

For Phase 2.2, the k was calculated both in ECCO and BISTRO for all 3 calculation modes. Considering the values of k obtained in BISTRO, between the k related to the $B^2 > 0$ subcritical mode and that associated with the $B^2 = 0$ configuration, the former was the one to closely match the k of the super-cell case. In particular, the calculation in BISTRO, using the cross sections from the subcritical cell approach in ECCO, was performed by cylindrizing the internal control assembly and the external fuel ring, where the latter becomes a ring around the former. The cross sections calculated in ECCO for the subcritical cell were then assigned to the internal circle, and those from the fuel assembly are assigned to the ring. Finally, the reflection boundary condition was applied. From Table 4.26, it can be observed that for the case of the super-cell calculation (see Section 4.4.1), the smallest value of the capture cross section is recorded, while for the

$B^2 > 0$ calculation that accounts for neutron leakage, the highest value is obtained. This observation is a consequence of the condensation of cross sections weighted by the fluxes in the different groups:

$$\sigma_{x,i,G} = \frac{\sum_{g\in\mathcal{G}} \sigma_{x,i,g}\phi_g}{\sum_{g\in\mathcal{G}} \phi_g}, \tag{4.6}$$

where:

- $\sigma_{x,i,\mathcal{G}}$ is the condensed microscopic cross section for reaction x in group $\mathcal{G}$ and isotope i.
- $\sigma_{x,i,g}$ is the microscopic cross section for reaction x in energy group g and isotope i.
- ϕ_g is the neutron flux in energy group g.
- $\sum_{g\in\mathcal{G}}$ indicates that the summation is performed over all energy sub-groups g that belong to the larger group $\mathcal{G}$.

Indeed, observing Figure 4.13, which shows the comparison of the energy-normalized neutron flux (see Eq. (4.2)) for the super-cell and the control cell ($B^2 > 0$) , it is clear that for the former there is a harder neutron flux corresponding to a smaller ^{10}B capture cross section (see Figure 4.12). However, this result could also be dependent on resonances.

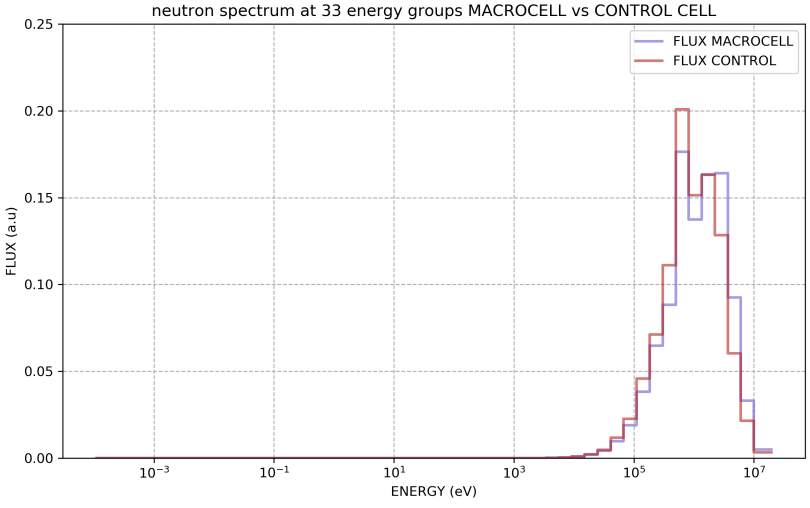

Figure 4.13: Comparison of neutron spectrum normalized by energy at 33 energy groups between super-cell (MACROCELL) and control cell ($B^2 > 0$).

Considerations on super-cell calculation

It is important to emphasize here certain aspects of this complex and heterogeneous super-cell calculation. During the simulations, it was noted that even with identical overall geometry, minor adjustments - such as eliminating small gaps or reversing the order of pin or assembly definitions - resulted in substantial variations in the outcomes. For instance, analyzing the k values for the 1-group condensation, the following results were obtained:

- For the super-cell without approximations (see Listing 4.3), $k = 0.873467$, corresponding to a microscopic capture cross section for ^{10}B of 1.51920 b.
- For the geometry with:
  - The definition of the fuel assembly, followed by the definition of the control rod assembly.
  - The elimination of the void with cladding dilution for the dummy pin of the fuel assembly.
  - The elimination of the gap with absorber dilution for the absorber pins.
  - The hexagonalization of the internal profile of the wrapper of the control rod assembly.

  the result is $k = 0.928186$, corresponding to a microscopic capture cross section for ^{10}B equal to 1.34464 b.

The result obtained with these approximations seems to be the most accurate when looking at the k found across the various ECCO steps. However, the capture cross section for ^{10}B deviates from the one calculated using the subcritical cell process. For this reason, it seems that the best result for the ^{10}B capture cross section is the one obtained through the calculation process for with the subcritical cell, however, further studies are necessary to better understand the super-cell calculation.

4.5 PHASE 2.3: Shield Super-cell Simulations

Phase 2.3 of the benchmark focuses on studying a two-dimensional heterogeneous model of a shield assembly surrounded by inner-type fuel assemblies (see Section 2.2). In modeling the super-cell, it was decided to include the fraction of inter-assembly lead corresponding to the coolant of the analyzed assemblies (see Figure 4.14). Additionally, the shield assembly was modeled as a fuel assembly with solid pellets made of yttria-stabilized zirconia (YSZ). Again, the boundary conditions were set in such a way as to recreate an infinite lattice of identical and axially infinite super-cells.

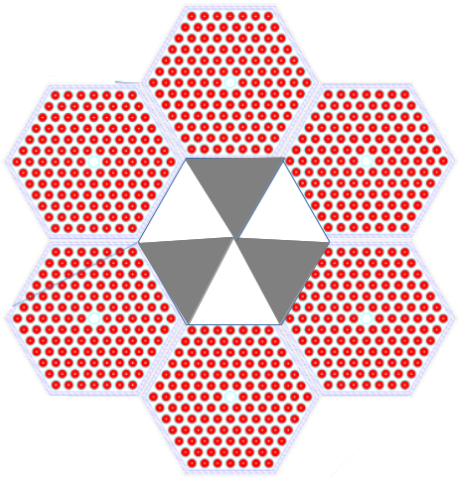

Figure 4.14: Model of the shield assembly surrounded by the a ring of six fuel assemblies.

The benchmark requires to find the following quantities:

- The infinite multiplication factor k.
- The fission and capture microscopic 1-group cross sections for ^{239}Pu, ^{241}Pu, ^{235}U, and ^{238}U, together with their average number of neutrons emitted per fission event ν.
- The 1-group inelastic scattering microscopic cross section for ^{238}U and ^{208}Pb.
- The 1-group capture microscopic cross sections for ^{56}Fe and ^{208}Pb.
- The reproduction factor $\eta = \dfrac{\nu\Sigma_f}{\Sigma_{a,fuel}}$.
- The utilization factor $f = \dfrac{\Sigma_{a,fuel}}{\Sigma_{a,tot}}$.
- The transport cross section $\Sigma_{tr} = \Sigma_t - \mu_0\Sigma_s$.
- The macroscopic fission, capture, elastic, and inelastic cross sections for the 7-group discretization.
- The five isotope and reaction combinations that give the highest k sensitivity coefficients and uncertainties.

4.5.1 Phase 2.3 Execution

As for the previous case, Phase 2.3 was solved using the ECCO cell code, and only the General method for the axially infinite configurations, was involved. Due to the high heterogeneity of the super-cell, it was necessary to make some simplifications to reduce the number of links and void regions. For this reason, it was decided to eliminate the void inside the dummy pin at the center of the assemblies by diluting its cladding. The same procedure was repeated for the gap surrounding the YSZ pellet inside the shield assembly (see Figure 4.15). These simplifications were introduced after analyzing multiple simulations, where efforts were made to preserve the geometry as defined by the benchmark, in which, it was evident that the cell calculation process led to significant fluctuations in the value of k.

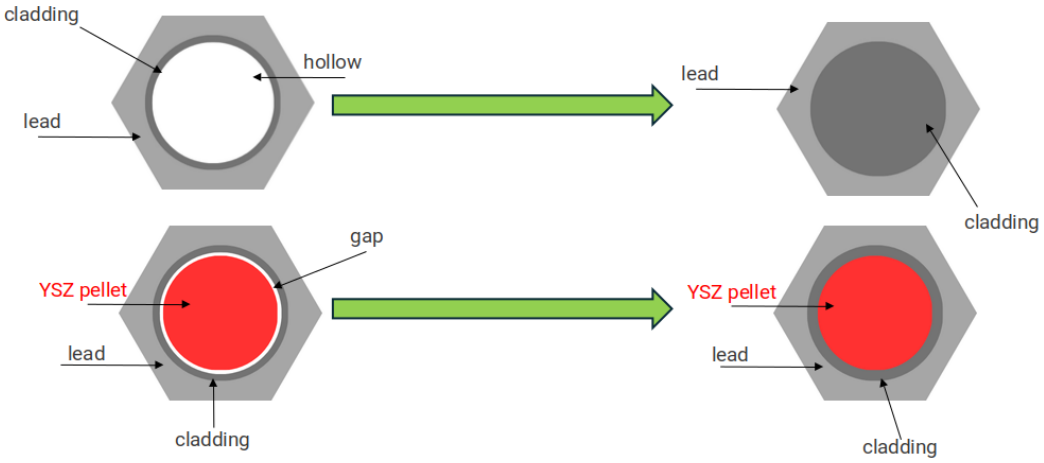

Figure 4.15: Simplified YSZ pin model.

For this case, in addition to the materials and media defined previously, the 'YSZ' medium was implemented and used to model the pin region of the shield assembly. The geometry is defined as in Listing 4.4.

```
CELL   'SHIELD super-cell'
COMPOSITION_ORDER
    'lead_med' 'AIM1_med' 'MOX_med' 'AIM1_DIL_med' 'YSZ_med' '2AIM1_DIL_med'
GEOMETRY DATA
HEXAGONAL LATTICE 2 (SA_PITCH) 2    ! START LAT super-cell
  HEXAGON 2 (W_IN) ! DEFINITION OF SHIELD ASSEMBLY
   HEXAGONAL LATTICE (N_RING) (PIN_PITCH) 2
   CYLINDRICAL 1
   (R_D_CLAD_OUT) REGION 1 'dummy_ysz' COMP 4 (TEMP_CELSIUS+273.15)
   IN
   REGION  2  'lead_dummy_ysz' COMP 1   (TEMP_CELSIUS+273.15)
   CYLINDRICAL 2
   (R_EXT_YSZ)   REGION 3  'pin_ysz' COMP 5   (TEMP_CELSIUS+273.15)
   (R_EXT_CLAD_YSZ) REGION 4 'clad_ysz' COMP 6 (TEMP_CELSIUS+273.15)
   IN
```

```
16    REGION 5 'lead_ysz' COMP 1 (TEMP_CELSIUS+273.15)
17    1 2 2 2 2 2 2
18    IN
19    REGION  6  'lead_flow_ysz' COMP 1   (TEMP_CELSIUS+273.15)
20    (W_OUT)
21    REGION  7   'wrapper_ysz' COMP 2  (TEMP_CELSIUS+273.15)
22    IN
23    REGION  8   'bypass_ysz'  COMP 1  (TEMP_CELSIUS+273.15)
24    HEXAGON 2 (W_IN) ! DEFINITION OF FUEL ASSEMBLY
25    HEXAGONAL LATTICE (N_RING) (PIN_PITCH) 2
26    CYLINDRICAL 1
27    (R_D_CLAD_OUT) REGION 9  'clad_dummy' COMP 4 (TEMP_CELSIUS+273.15)
28    IN
29    REGION  10  'lead_dummy' COMP 1   (TEMP_CELSIUS+273.15)
30    CYLINDRICAL 2
31    (R_EXT_GAP)   REGION 11  'fuel' COMP 3   (TEMP_CELSIUS+273.15)
32    (R_EXT_CLAD)  REGION 12  'clad' COMP 2   (TEMP_CELSIUS+273.15)
33    IN
34    REGION  13  'lead' COMP 1   (TEMP_CELSIUS+273.15)
35    1 2 2 2 2 2 2
36    IN
37    REGION  14  'lead_flow' COMP 1   (TEMP_CELSIUS+273.15)
38    (W_OUT)
39    REGION  15   'wrapper' COMP 2  (TEMP_CELSIUS+273.15)
40    IN
41    REGION  16   'bypass'  COMP 1  (TEMP_CELSIUS+273.15)
42  1 2 ! END LATTICE super-cell
43  REFLECT ! BOUNDARY CONDITION super-cell
44  END OF GEOMETRY DATA
45  ;
```

Listing 4.4: Geometry of shield super-cell for benchmark Phase 2.3.

The reflection boundary condition was applied to the outer face of geometry. The geometry of the super-cell was defined as a shield assembly surrounded by one ring of fuel assemblies. This macrostructure was created using the HEXAGONAL LATTICE command on line 5, setting the option for the number of cell types in the lattice to 2. The cell of type 2 is the fuel cell, which is identical to that defined for Phase 2.1 of the benchmark. The cell of type 1, on the other hand, is that of the shield, which has the same structure as that of type 1, with the exception that the fuel pins are replaced by YSZ pins. In line 42, the two rings that make up the super-cell were defined, with the innermost being the shield ring.
Notice that the choice to adopt a single fuel assembly ring derives from the fact that with more than two rings of hexagons that are themselves hexagonal lattice, the geometry became too complicated, leading to wrong results (see Subsection 4.4.1).

4.5.2 Phase 2.3 Results

1-group macroscopic cross sections and integral parameters

Table 4.27 shows the results obtained using the Axially Infinite ECCO computational routines, with input data highlighted in red.

Quantity	Axially Infinite configuration	Unit
k	1.20104	#
B^2	0.0000	cm^{-2}
Σ_a	4.65356×10^{-3}	cm^{-1}
$\Sigma_{a,fuel}$	4.29301×10^{-3}	cm^{-1}
$\nu\Sigma_f$	5.57724×10^{-3}	cm^{-1}
Σ_f	1.90952×10^{-3}	cm^{-1}
Σ_{tr}	2.79985×10^{-1}	cm^{-1}
η	1.29914	#
f	9.22521×10^{-1}	#

Table 4.27: 1-group output quantities for Phase 2.3: multiplication factor k, buckling B^2, main macroscopic cross sections, reproduction factor η, and utilization factor f.

The first thing that can be observed is the value of k, which falls between that of Phase 2.2 and that of Phase 2.1. This result was expected, as it is lower than the case of an infinite lattice composed only of fuel cells and higher than a lattice where, for every six fuel cells, there is one control rod cell. An important aspect detected during the simulations is that, while for simple cells such as those of Phases 1 and 2.1, the k calculated with a 1-group condensation matches those related to multi-group calculations, Phase 2.3 evidences that a greater cell complexity requires an increased calculation precision. Table 4.28 shows the values of k calculated by condensing to 1, 7, and 33 groups.

G	k (ECCO)	k (BISTRO)
1	1.20104	1.20023
7	1.21977	1.21898
33	1.21910	1.21837

Table 4.28: Comparison of k between ECCO and BISTRO for 1, 7, and 33 group condensations for Phase 2.3.

Referring to the values in Table 4.27, it can be observed that in the absence of an absorber, Σ_a is lower compared to Phase 2.2. Regarding other quantities, the utilization factor f for the case under consideration is higher than that of the control super-cell, as almost all of the absorption occurs in the fuel. However, it remains lower than in Phase 2.1, where the fuel concentration is higher. In relation to Σ_f, Phase 2.2 and Phase 2.3 have the same fuel concentrations, but the microscopic fission cross sections differ: they are higher for fissile isotopes in Phase 2.3, and for the fissionable ones in Phase 2.2 (see Table 4.29). This difference is due to the cell neutron spectrum, which exhibits lower energies in the cell with a shield. However, these effects counterbalance

each other, resulting in nearly identical macroscopic fission cross sections Σ_f. Despite this, the reproduction factor η is higher for the control super-cell, as the fuel absorption is lower than the shield one. Recalling that $\Sigma_a = \Sigma_c + \Sigma_f$, this indicates that in Phase 2.3 the fuel exhibits higher captures (see Table 4.29).

1-group microscopic quantities

Isotope	Quantity	Axially Infinite configuration	Unit
^{239}Pu	σ_c	5.98756×10^{-1}	b
^{239}Pu	σ_f	1.85967	b
^{239}Pu	ν	2.93145	#
^{241}Pu	σ_c	4.95534×10^{-1}	b
^{241}Pu	σ_f	2.69710	b
^{241}Pu	ν	2.96164	#
^{235}U	σ_c	6.22048×10^{-1}	b
^{235}U	σ_f	2.07526	b
^{235}U	ν	2.45017	#
^{238}U	σ_c	3.19766×10^{-1}	b
^{238}U	σ_f	3.32071×10^{-2}	b
^{238}U	ν	2.72048	#
^{56}Fe	σ_c	9.48593×10^{-3}	b
^{208}Pb	σ_c	6.39065×10^{-4}	b
^{208}Pb	σ_{in}	2.03507×10^{-2}	b

Table 4.29: 1-group microscopic cross sections σ and the average number of neutrons emitted per fission event ν for Phase 2.3. The subscripts c, f, and in represent the capture, fission, and inelastic reactions.

In Table 4.29, the observations made so far regarding the spectrum of the super-cell containing the shield assembly become evident. Specifically, the spectrum is softer compared to all other cases, as indicated by the iron capture cross section and ν.

Uncertainty and sensitivity analysis for the infinite case

The five most impactful isotope and reaction combinations in terms on k sensitivity and uncertainty (see Sections 3.4 and 3.5) were chosen among the main isotopes involved in the previous benchmark requests. Similarly to Phase 1, they were calculated in ERANOS with condensed cross sections at 33 groups.

$\boldsymbol{\alpha}$	$\boldsymbol{S(k,\alpha)}$
$\sigma_f^{^{239}\mathrm{Pu}}$	4.8410×10^{-1}
$\sigma_c^{^{238}\mathrm{U}}$	-2.2859×10^{-1}
$\sigma_f^{^{241}\mathrm{Pu}}$	7.6745×10^{-2}
$\sigma_c^{^{239}\mathrm{Pu}}$	-5.8212×10^{-2}
$\sigma_{el}^{^{238}\mathrm{U}}$	-5.6519×10^{-2}

Table 4.30: Most relevant sensitivity coefficients $S(k,\alpha)$ of the multiplication factor k to the input data α for Phase 2.3.

$\boldsymbol{\alpha}$	$\boldsymbol{\varepsilon(k,\alpha)}$
$\sigma_f^{^{239}\mathrm{Pu}}$	5.61860×10^{-3}
$\sigma_c^{^{238}\mathrm{U}}$	3.17660×10^{-3}
$\sigma_c^{^{239}\mathrm{Pu}}$	3.10750×10^{-3}
$\sigma_{in}^{^{238}\mathrm{U}}$	2.58440×10^{-3}
$\sigma_{in}^{^{239}\mathrm{Pu}}$	1.26020×10^{-3}

Table 4.31: Most relevant uncertainties $\varepsilon(k,\alpha)$ of the multiplication factor k to the input data α for Phase 2.3.

Once again, it can be seen that plutonium tops both rankings while maintaining that difference of two orders of magnitude between sensibility and uncertainty.

7-group macroscopic cross sections

Group	$\boldsymbol{\Sigma_f}$ **[cm^{-1}]**	$\boldsymbol{\Sigma_c}$ **[cm^{-1}]**	$\boldsymbol{\Sigma_{el}}$ **[cm^{-1}]**	$\boldsymbol{\Sigma_{in}}$ **[cm^{-1}]**
1	5.68055×10^{-3}	1.10298×10^{-3}	1.70507×10^{-1}	5.63820×10^{-2}
2	2.40361×10^{-3}	7.78752×10^{-4}	2.03757×10^{-1}	1.98916×10^{-2}
3	1.33382×10^{-3}	1.22223×10^{-3}	3.16759×10^{-1}	6.29525×10^{-3}
4	1.66019×10^{-3}	4.31564×10^{-3}	4.40912×10^{-1}	6.17705×10^{-4}
5	5.12613×10^{-3}	1.41287×10^{-2}	4.65635×10^{-1}	5.69743×10^{-12}
6	2.39908×10^{-2}	5.36102×10^{-2}	4.62478×10^{-1}	3.64970×10^{-18}
7	5.81829×10^{-2}	6.54146×10^{-2}	4.45448×10^{-1}	1.21933×10^{-18}

Table 4.32: 7-group macroscopic cross sections Σ for Phase 2.3. The subscripts f, c, el, and in represent the fission, capture, elastic, and inelastic reactions.

Table 4.32 shows that the cross sections follow the same trends across the 7 groups as in the previous phases; however, they show differences in terms of values for the respective groups. In particular, compared to Phase 2.2, the following differences are observed:

- Macroscopic fission cross section Σ_f: The values of Σ_f are slightly different between the two phases for all groups. In Phase 2.3, the values are generally lower compared to Phase 2.2, particularly in groups 6 and 7, where a significant reduction is observed. However, when considering the one-group condensed fission cross section, it shows a higher value for Phase 2.3. This result is likely due to the condensation weighted by the flux (see Eq. (4.6)).

- Macroscopic capture cross section Σ_c: The values of Σ_c show variations between the two phases. Phase 2.3 shows a reduction in capture values for most energy groups compared to Phase 2.2, this is due to the presence of an absorber in the super-cell case of Phase 2.2.

- Macroscopic elastic cross section Σ_{el}: The macroscopic elastic cross sections change slightly between the two phases. In Phase 2.3, the values for groups 2 to 4 are slightly higher, while for groups 5, 6, and 7, the values are lower compared to Phase 2.2.

- Macroscopic inelastic cross section Σ_{in}: The macroscopic inelastic cross sections also present differences. In Phase 2.3, the values for the first three groups are quite similar to those in Phase 2.2, but for groups 4 to 7, there is an even more significant reduction compared to Phase 2.2.

Chapter 5

Conclusions

The Lead-cooled Fast Reactors (LFR) have garnered increasing international attention after being selected by the Generation-IV International Forum (GIF) as a promising candidate for future nuclear energy systems. However, very limited operating experience exists to support the design, verification, and licensing of LFRs, especially for the core design. For this reason, the Expert Group on Physics of Reactor Systems (EGPRS) of the Organisation for Economic Co-operation and Development (OECD) Nuclear Energy Agency (NEA) endorsed a neutronic benchmark to assess the simulation capabilities for LFR systems. The benchmark aims to: familiarize with the physics of an LFR core, practice with the neutronics of an LFR core, and assess the confidence in the ability to simulate an LFR core. The reference system chosen for the benchmark is the Advanced Lead-cooled Fast Reactor European Demonstrator (ALFRED). The neutronic benchmark of ALFRED, organized in three phases, aims to assess the simulation capabilities of fast reactor codes for LFR systems through a gradual approach, starting from local models and progressing to whole-core simulations.
In this thesis, calculations concerning the first two phases of the benchmark were performed using the deterministic ERANOS system and its integrated cell code, ECCO. Specifically, ECCO was used to compute the cross sections and integral parameters for each cell in the study cases. To achieve this, the numerical methods for solving both homogeneous and heterogeneous cell calculations were thoroughly explored in depth to set up the calculation procedures capable of accurately modeling the physics of the cell. To assess the variation in the multiplication factor k due to changes in microscopic cross sections or uncertainties in the input parameters from nuclear data, sensitivity and uncertainty analyses were performed. As ECCO does not support these analyses, the BISTRO reactor code, included in the ERANOS suite, was used instead. As a result, routines were developed within ERANOS to automatically extract condensed and homogenized cross sections from ECCO and transfer them to BISTRO. Within the reactor code, the geometry was recreated and the homogenized cross sections were assigned to proceed with the aforementioned analyses.

For Phases 1 and 2.1, in addition to the benchmark requirements, two other types of analyses were conducted:

- Comparison between the infinite lattice cell (required by the benchmark) and a critical cell case (still radially infinite), in which the axial dimension is finite, determined by buckling.
- Comparison between the Roth 6 and General solution methods.

From the comparison of the two configurations (for both Phase 1 and Phase 2.1), it was found that the critical cell exhibits a slightly harder neutron spectrum compared to the infinite cell. This difference impacted the microscopic cross sections (and consequently the macroscopic ones), particularly the fission cross sections, where lower values were observed for fissile isotopes and higher values for fertile isotopes in comparison to the infinite cell. The result is a larger macroscopic fission cross section for the critical cell configuration, highlighting how, in a harder spectrum, the fertile fuel component, particularly ^{238}U, plays a key role.
Another interesting result came from the axial buckling search for the critical configuration (for both Phase 1 and Phase 2.1). The result obtained is plausible for a reactor whose core is designed to develop more horizontally than vertically (e.g. with a 3:1 aspect ratio). Additionally, when comparing the buckling for the critical configuration of the Pin Cell with that of the Fuel Assembly, a higher value was observed, which is justified by the greater fuel fraction than in the Fuel Assembly cell, as the latter contains also, wrapper material and dummy pins, thus requiring a larger axial dimension to achieve criticality. This is also confirmed in the infinite configuration, where the largest multiplication factor is for the Fuel Pin cell.
The comparison between the two numerical methods showed minimal differences for Phase 1, where the geometry is relatively simple and not very heterogeneous, while greater differences emerged for Phase 2.1. Using the manual and literature sources, it was concluded that the Roth 6 method provides better results for a single hexagonal fuel assembly than the General method, as the search for the multiplication factor yields a more stable result throughout the calculation steps.
For the 2.2 and 2.3 cases, only the General method could be used, as for Super-cells (i.e., an assembly of multiple S/As), the Roth 6 method cannot find a solution.
For the Absorber Super-cell case, particular attention was given to the capture microscopic cross sections for ^{10}B. This was calculated using both the approach employed in previous cases, where the entire cell is defined and solved as a single geometry (using the General method), and the approach proposed in ECCO for control rod cell calculations. In this approach, the fuel assembly and control rod assembly are defined separately, assuming that the former provides the flux to the latter. Comparing the ^{10}B microscopic cross sections, differences emerged, likely due to an overestimation in the split-cell approach and an underestimation in the single-cell calculation. However, the results suggest

that the split-cell calculation provides a more plausible value, as applying the General method to complex and heterogeneous cells, such as those in Phases 2.2 and 2.3, leads to results affected by numerical uncertainties. Specifically, for both cases (more evident in 2.2, being subcritical), instability in the solution of k was observed depending on how the geometry is defined in the code. This is due to the fact that, for heterogeneous geometry steps, the collision probability methods used to solve the transport equation for the flux introduce a series of approximations that become non-negligible for geometries with many nested elements, varying based on how these elements are declared (e.g., which assembly is defined first in the geometry). For this reason, further investigation of the ECCO cell code and the General method for treating heterogeneous cells with many nested elements will be necessary in the future.
The final result to highlight is related to the sensitivity coefficients and the uncertainties that nuclear data introduce in the solution of the multiplication factor k. In all simulations, k was particularly sensitive to variations in the microscopic fission cross section of ^{239}Pu, which proved to be the most significant factor, and the microscopic capture cross section of ^{238}U, which ranked second in importance (in Phase 2.2, the microscopic capture cross section of ^{10}B emerged as the second most significant factor). Despite this, the uncertainties associated with ^{239}Pu and ^{238}U remained the largest, though comparable to those of other key nuclide-reaction pairs.

Bibliography

[1] E. E. Lewis and W. F. Miller, "Computational methods of neutron transport," Jan. 1984. [Online]. Available: https://www.osti.gov/biblio/5538794.

[2] P. Peerani, "Elementi di neutronica per il codice di cella ECCO," ENEA, Technical Report, May 1989.

[3] G. Rimpault, "Physics documentation of Eranos: The ECCO Cell Code," CEA, Technical Report DER-SPRC-LEPh97-001, 1997.

[4] Entreprise extérieure, "Generalisation du calcul des probabilités de collision dans ECCO," CEA, Note Technique 00-214, Dec. 2001.

[5] G. Rimpault, D. Plisson, J. Tommasi, *et al.*, "The ERANOS code and data system for fast reactor neutronic analyses," in *PHYSOR 2002-International Conference on the New Frontiers of Nuclear Technology: Reactor Physics, Safety and High-Performance Computing*, 2002.

[6] J. Tommasi, "ERANOS USER'S MANUAL – Applications of Perturbation Theory with Finite Difference Diffusion and Sn Transport Flux solvers / ERANOS Manuel des Methodes – Applications de la Theorie des Perturbations avec des Solveurs de Flux Diffusion et Transport Sn en Differences Finies," CEA, Technical Report 07-003, 2007.

[7] P. Reuss, *Neutron Physics* (Nuclear engineering). EDP Sciences, 2008.

[8] W. M. Stacey, *Nuclear Reactor Physics*, Second Edition, Completely Revised and Enlarged. Wiley, 2010.

[9] K. Aoto, P. Dufour, Y. Hongyi, *et al.*, "A summary of sodium-cooled fast reactor development," *Progress in Nuclear Energy*, vol. 77, pp. 247–265, 2014, ISSN: 0149-1970. DOI: https://doi.org/10.1016/j.pnucene.2014.05.008. [Online]. Available: https://www.sciencedirect.com/science/article/pii/S0149197014001279.

[10] G. Grasso, C. Petrovich, D. Mattioli, *et al.*, "The core design of alfred, a demonstrator for the european lead-cooled reactors," *Nuclear Engineering and Design*, vol. 278, pp. 287–301, 2014, ISSN: 0029-5493. DOI: https://doi.org/10.1016/j.nucengdes.2014.07.032. [Online]. Available: https://www.sciencedirect.com/science/article/pii/S0029549314004361.

[11] D. Asner, K. Burns, L. Campbell, *et al.*, "Method of fission product beta spectra measurements for predicting reactor anti-neutrino emission," *Nuclear Instruments and Methods in Physics Research Section A: Accelerators, Spectrometers, Detectors and Associated Equipment*, vol. 776, pp. 75–82, 2015, ISSN: 0168-9002. DOI: https://doi.org/10.1016/j.nima.2014.09.076. [Online]. Available: https://www.sciencedirect.com/science/article/pii/S0168900214011085.

[12] M. Frignani, A. Alemberti, and M. Tarantino, "Alfred: A revised concept to improve pool related thermal-hydraulics," *Nuclear Engineering and Design*, vol. 355, p. 110 359, 2019, ISSN: 0029-5493. DOI: https://doi.org/10.1016/j.nucengdes.2019.110359. [Online]. Available: https://www.sciencedirect.com/science/article/pii/S0029549319303930.

[13] G. Grasso, M. Sarotto, F. Lodi, and D. M. Castelluccio, "An improved design for the alfred core," in *International Congress on Advances in Nuclear Power Plants (ICAPP 2019)*, SFEN, Juan-les-Pins, France, May 2019.

[14] A. Alemberti, M. Caramello, M. Frignani, *et al.*, "Alfred reactor coolant system design," *Nuclear Engineering and Design*, vol. 370, p. 110 884, 2020, ISSN: 0029-5493. DOI: https://doi.org/10.1016/j.nucengdes.2020.110884. [Online]. Available: https://www.sciencedirect.com/science/article/pii/S0029549320303782.

[15] C. Demazière, "3 - Neutron transport calculations at the cell and assembly levels," in *Modelling of Nuclear Reactor Multi-physics*, C. Demazière, Ed., Academic Press, 2020, pp. 73–192, ISBN: 978-0-12-815069-6. DOI: https://doi.org/10.1016/B978-0-12-815069-6.00003-9. [Online]. Available: https://www.sciencedirect.com/science/article/pii/B9780128150696000039.

[16] D. Mostacci, *Trasporto di Neutroni. Appunti per il corso di Trasporto di Particelle e Radiazioni*, Lecture notes, Per gli allievi del Corso di Laurea Specialistica in Ingegneria Energetica. Anno Accademico 2019/2020, 2020.

[17] G. Grasso, "The current alfred core design," ENEA, Technical Report SICNUC-P000-017, 2022.

[18] G. I. I. Forum, *Gif 2023 annual report*, 2023. [Online]. Available: https://www.gen-4.org/gif/jcms/c_224108/gif-2023-annual-report.

[19] C. F. Smith and L. Cinotti, "Chapter 6 - lead-cooled fast reactors (lfrs)," in *Handbook of Generation IV Nuclear Reactors (Second Edition)*, ser. Woodhead Publishing Series in Energy, I. L. Pioro, Ed., Second Edition, Woodhead Publishing, 2023, pp. 195–230, ISBN: 978-0-12-820588-4. DOI: https://doi.org/10.1016/B978-0-12-820588-4.00018-9. [Online]. Available: https://www.sciencedirect.com/science/article/pii/B9780128205884000189.

[20] NEA, *Lead-cooled fast reactor benchmark (lfr)*. [Online]. Available: https://www.oecd-nea.org/jcms/pl_66836/lead-cooled-fast-reactor-benchmark-lfr.

[21] OECD Nuclear Energy Agency, *JANIS (Java-based Nuclear Data Information Software)*. [Online]. Available: https://www.oecd-nea.org/jcms/pl_39910/janis.

[22] W. Ambrosini and B. Montagnini, *Lezioni sul Trasporto dei Neutroni*. Pisa, Italia, 1999-2000, Appunti ad uso del corso di Metodi Numerici per Reattori Nucleari.

[23] U. D. N. E. R. A. Committee and the Generation IV International Forum, "A technology roadmap for generation iv nuclear energy systems," December 2002. [Online]. Available: https://www.gen-4.org/gif/jcms/c_40481/technology-roadmap.